Studies on Variability of Non-Thermal Emissions in Solar Flares

A thesis presented
by

Takashi Minoshima

to
The Department of Earth and Planetary Science
in partial fulfillment of the requirements
for the degree of
Doctor of Science
in the subject of

Solar Physics

The University of Tokyo
Tokyo, JAPAN
December 2007

Thesis advisor
Takaaki Yokoyama

Author
Takashi Minoshima

Studies on Variability of Non-Thermal Emissions in Solar Flares

Abstract

Many observations of hard X-rays (HXRs) and microwaves in solar flares have told that a significant amount of non-thermal electrons are produced. However, their kinematics of acceleration and transport is still an open question. The determination of the energy and pitch-angle distribution of accelerated electrons from the observations is essential to solve this problem. From both observational and theoretical studies, we determined the distribution of injection electrons and addressed electron acceleration mechanisms in solar flares.

We performed a comparative analysis of non-thermal emissions of HXRs and microwaves in the impulsive phase of the 2003 May 29 flare, to reveal characteristics of non-thermal electrons in a wide energy range. We focus on the higher energy HXRs above 100 keV that have been less studied and thus less understood so far. We found that the spatial distribution of the higher energy HXRs coincides with that of the lower energy HXRs below 100 keV while the time profile of the spectrum of the higher energy HXRs is similar to that of the microwaves. This analysis showed characteristics of higher energy HXR-emitting electrons (in intermediate energy range) as well as lower energy HXR-emitting electrons (in lower energy range) and microwave-emitting ones (in higher energy range).

To explain the observed variability and determine the injection pitch-angle distribution, we developed a general treatment of the electron transport model called trap-plus-precipitation, by solving the Fokker-Planck equation in space, energy, and pitch angle. Comparing the calculations and observations, we showed that the trap-plus-precipitation model in the weak diffusion regime can explain the variability of the observed non-thermal emissions. By the observed characteristics of the higher energy HXRs, we concluded that the electrons are accelerated more perpendicular to than parallel to the magnetic field line. We suggest a possible mechanism of the betatron acceleration to yield such pitch-angle distribution.

We performed a detailed analysis of the spatial distribution of non-thermal emis-

sions in the early impulsive phase of the 2003 May 29 flare. We found an energy-dependent asymmetric distribution of footpoint HXR sources appeared at the southeast and northwest sites. The northwest footpoint HXR source is brighter (weaker) for lower (higher) energy than the southeast one, and its time profile leads the southeast. This variability could not be explained by previously proposed scenarios. We showed that this could be explained if the injected electrons have an asymmetric pitch-angle distribution in direction parallel to the magnetic field. A field-aligned electric field is a candidate to yield this pitch-angle distribution.

We numerically studied the electron propagation along the loop based on the observation of the 1999 August 28 flare. From the refined modeling of the electron propagation with the Fokker-Planck equation and the gyrosynchrotron radiation, we concluded that the injected electrons have to be widely distributed in pitch-angle space to yield the observed propagating feature of the microwave source. We suggest that the electrons are almost isotropically accelerated in this flare.

By the observational and theoretical studies, we addressed the pitch-angle distributions of injection electrons in three cases. These are different from each other, implying that a different acceleration mechanism efficiently works in a different physical condition. A macroscopic magnetic field configuration is one of the keys. During the impulsive phase of the 2003 May 29 flare, the flare geometry shows a simple two-dimensional configuration, which is close to the dipole magnetic field or is described by the Petschek-type magnetic reconnection model. In such geometry, the adiabatic betatron acceleration works more efficiently than the adiabatic Fermi acceleration. Consequently the electron pitch-angle distribution is concentrated perpendicular to the magnetic field line.

On the other hand, the geometries in the early impulsive phase of the 2003 May 29 flare and the 1999 August 28 flare are different from the two-dimensional picture. They show a complex three-dimensional configuration. In such geometries, the betatron acceleration might not play a dominant role. Different electron acceleration mechanisms might efficiently work and then yield different pitch-angle distributions.

Contents

List of Figures

Acknowledgments

First, I would like to express my sincere gratitude and appreciation to associate professor Takaaki Yokoyama for his kindhearted guidances, meaningful comments and discussions, and continuous encouragements to achieve my works, throughout the five years of my graduate studies. He has taught me a lot, such as, how to study, how to have a presentation, how to write a paper, and so on. I am really happy that I study in his laboratory.

I would like to deeply thank Profs. M. Hoshino and T. Terasawa for their helpful and valuable advises and comments during my graduate studies. I thank Drs. H. Isobe, M. Oka, and S. Imada for their continuous advises and encouragements. I thank all members of Space & Planetary Science Group for wonderful and enjoyable discussions with them.

I greatly appreciate Drs. K. Makishima (University of Tokyo), M. Fujimoto (Institute of Space and Astronautical Science, Japan Aerospace Exploration Agency), S. Masuda, J. Sato (Solar-Terrestrial Environment Laboratory, Nagoya University), and S. Tsuneta (National Astronomical Observatory of Japan) for fruitful comments and discussion. I also would like to thank Drs. K. Shibasaki, M. Shimojo, A. Asai, and H. Nakajima for fruitful discussions and giving me opportunities to study in the solar group at Nobeyama Radio Observatory.

I acknowledge Drs. S. Krucker, H. S. Hudson, G. J. Hurford, K. Watanabe, and R. P. Lin for giving me wonderful experiences to study at Space Sciences Laboratory, University of California, Berkeley. I also thank Dr. A. Caspi for his careful reading my manuscripts and giving me helpful comments. I deeply acknowledge the whole *RHESSI* team for providing worthwhile data and software, and providing me opportunities to study the physics of solar flares with hard X-rays.

My work is supported by COE program of the University of Tokyo, "Predictability of the Evolution and Variation of the Multi-scale Earth System: An integrated COE for Observational and Computational Earth Science".

Finally, I would like to express my largest thank to my parents and sister for their continuous supports and encouragements.

Chapter 1

General Introduction

In the first part of this chapter, we briefly review solar flares and their non-thermal aspects from the observational point of view. The radiation mechanisms for the non-thermal emissions are also reviewed that are necessary to deduce information of non-thermal electrons from the observational data. Next, we briefly review current understanding of the physics of non-thermal electrons from the theoretical point of view. Finally we raise questions to be solved in this thesis.

1.1 Solar Flares

The solar corona is full of dynamic plasma phenomena. Recent observations have revealed that the solar corona is much dynamic than we thought, even if the Sun is quiet. Above all, a solar flare (Fig. 1.1) is the largest exploding phenomenon in our solar system. Its spatial scale reaches 10^5 km, which is 10 times larger than the radius of the Earth. Its energy reaches 10^{32} erg, which is 100 million times larger than the energy released by a hydrogen bomb. Once the flare occurs, a huge amount of energy is released in a short time, and solar plasma is strongly heated and accelerated. Almost all flares are accompanied by a huge amount of mass ejection, the so-called coronal mass ejections (CMEs), into interplanetary space. It affects the Earth's magnetosphere, yielding geomagnetic storm and aurora.

Classically solar flares were merely recognized as sudden exploding and brightening phenomena on the photosphere (Carrington, 1859). But recent notable progress of

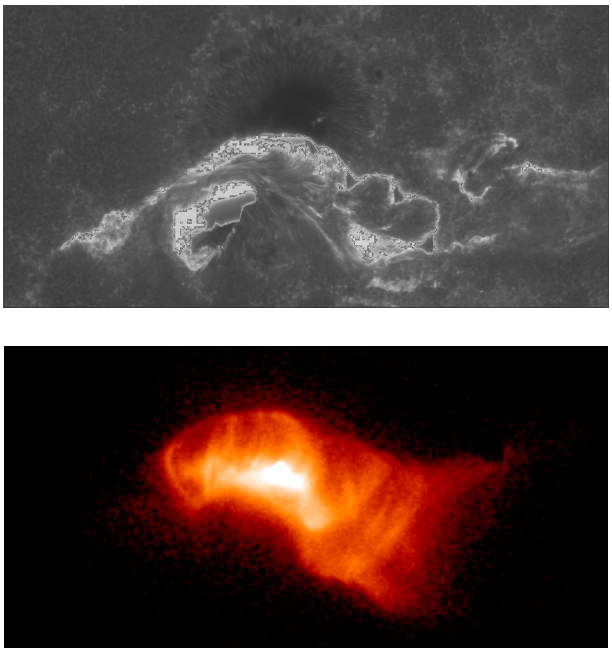

Figure 1.1: *Hinode* observation of a solar flare occurred on 2006 December 13. *Top*: Ca II H image at 02:30 UT taken with the Solar Optical Telescope (SOT; Tsuneta et al., 2007). *Bottom*: Soft X-ray image at 03:00 UT taken with the X-Ray Telescope (XRT; Golub et al., 2007). Solar north is up and west is to the right. Note that the field of views of both images are different, $200'' \times 100''$ ($1'' \sim 700$ km) for SOT image and $280'' \times 140''$ for XRT image. The center positions of images with respect to the Sun are also different from each other.

observational instruments such as *Yohkoh* (Ogawara et al., 1991), *SOHO*[1], *TRACE*[2], *RHESSI*[3], and *Hinode* (Kosugi et al., 2007) has made it possible to investigate the pictures and physics of solar flares in detail. Solar flares are understood as a consequence of release of the magnetic energy that is stored in the corona. The magnetic reconnection model is widely accepted to explain the mechanism of solar flares. Magnetic reconnection, topological change of a configuration of antiparallel magnetic field

[1] *Solar and Heliospheric Observatory* (Domingo et al., 1995).

[2] *Transition Region and Coronal Explorer* (Handy et al., 1999).

[3] *Reuven Ramaty High Energy Solar Spectroscopic Imager* (Lin et al., 2002).

lines in the presence of plasma, is a fundamental physical process of plasma and is thought to be a highly efficient engine to convert magnetic energy into thermal and kinetic energies of plasma. Observed phenomena associated with solar flares such as a cusp shaped structure (Tsuneta et al., 1992), plasmoid ejections (Ohyama & Shibata, 1998), a reconnection inflow (Yokoyama et al., 2001), and so on, morphologically confirm the standard magnetic reconnection model called the CSHKP model (Fig. 1.2; Carmichael, 1964; Sturrock, 1966; Hirayama, 1974; Kopp & Pneuman, 1976). The scenario of the CSHKP model is as follows. When magnetic reconnection occurs at the corona, the magnetic energy is released and the coronal plasma is heated and accelerated. Some of them propagate downward to the solar chromosphere/photosphere along the reconnected magnetic field lines. When they precipitate into the chromosphere, they dissipate their energy and heat the chromospheric dense plasma (blue regions in Fig. 1.2). This period is observed with such as Hα line (e.g., Asai et al., 2004), Ca II H line (top image of Fig. 1.1), and ultraviolet (UV) band. The heated chromospheric plasma, which has a higher gas pressure, starts to move upward and then fills the magnetic loop in the corona (red regions in Fig. 1.2). This phenomenon is called "chromospheric evaporation" (Antonucci et al., 1982, 1984). Consequently the flare loop is filled with high temperature dense plasma and can be observed in X-ray band (bottom image of Fig. 1.1).

1.2 Non-Thermal Emissions

Solar flares radiate electromagnetic waves over a very wide range of wavelengths extending from X-rays (occasionally γ-rays) to microwaves. Figure 1.3 shows a schematic picture of light curves in various wavelengths (Kane, 1974). One can recognize from the time profile of light curves that flares have two phases with different properties. Light curves of such as Hα line and soft X-ray (SXR) band show a smoothly varying profile with long duration of tens of minutes to hours. The period when these emissions are prominent is called the "gradual phase". The emissions in the gradual phase are produced by thermal plasma with a temperature of $\sim 1 \times 10^{6-7}$ K in the loop.

On the other hand, light curves of high energy ($\gtrsim$ 30 keV) X-ray called hard

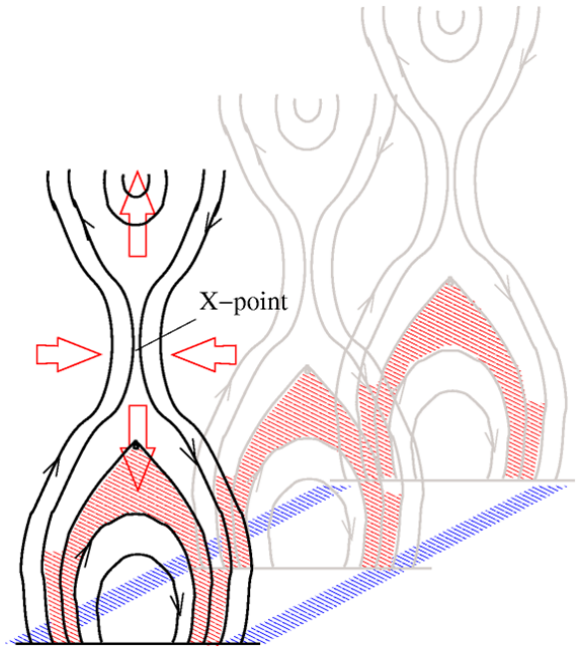

Figure 1.2: Cartoon of the CSHKP model. Solid lines show the magnetic field lines. Red arrows show the directions of plasma flow. Blue regions show the emission from chromosphere, called "flare ribbons". Red regions show the emission from the flare loop.

X-ray (HXR) and gigahertz microwave bands show a fluctuating profile with short duration of seconds to minutes, leading the light curves in the gradual phase. The period when these emissions can be seen is called the "impulsive phase". These emissions are thought to be generated by electrons which energy is quite higher than the temperature of the flare plasma. The energy spectra of the HXR photon flux are presented in Figure 1.4 (Lin et al., 1981). During the impulsive phase (left), the HXR spectra ranging from tens to hundreds keV are not expressed by a Maxwellian but by a power-law function. Therefore these are non-thermal emissions, thus indicating that high energy non-thermal particles (electrons) are produced in association with the flare.

The particle acceleration, also seen in other space plasma environments such as interplanetary shocks, Earth's magnetospheric reconnection, supernova remnant, and so on, is a universal phenomenon of the plasma. However, a mechanism for accelerating particles is still an open question. In solar flares, a considerable amount of

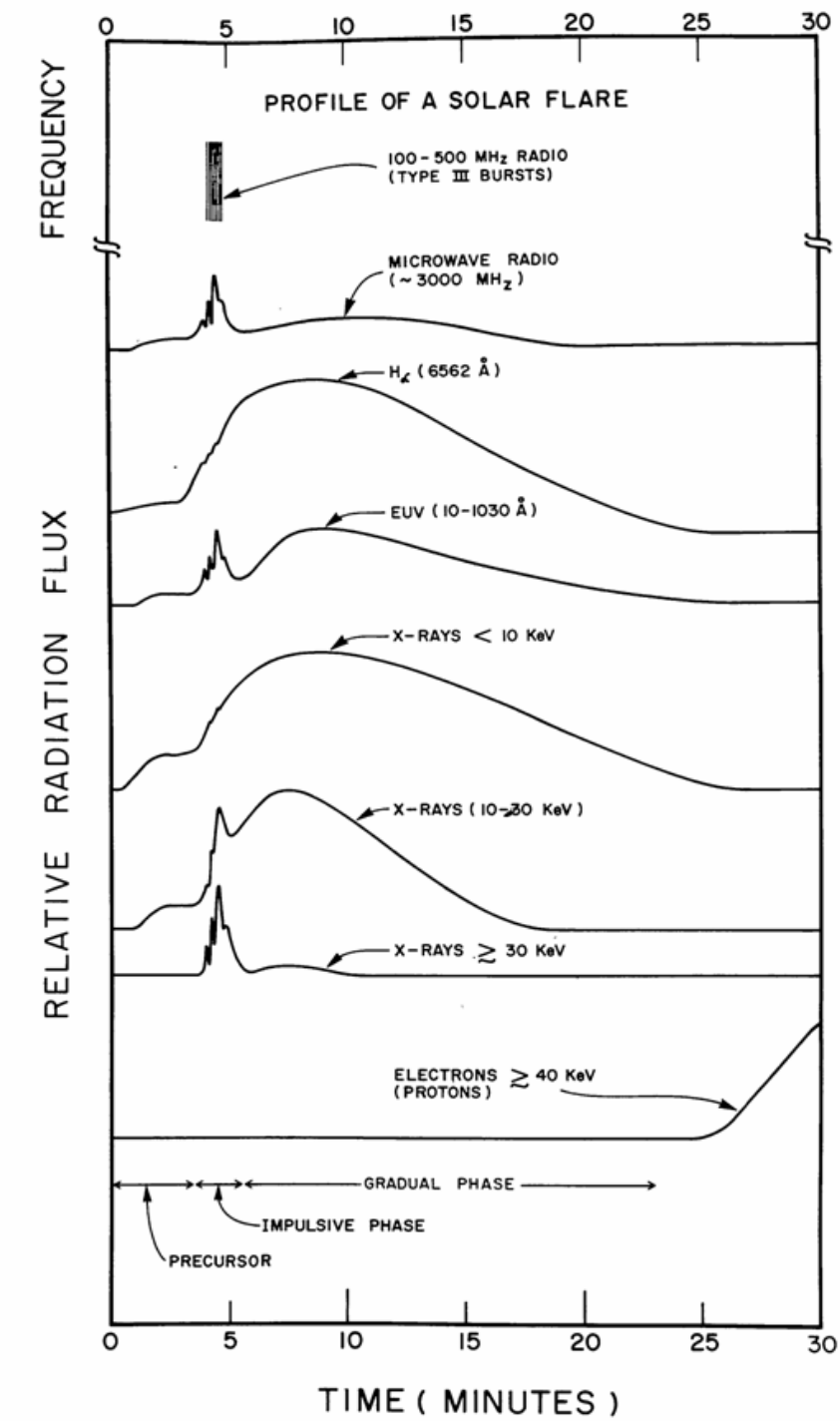

Figure 1.3: Schematic picture of light curves of a solar flare in various wavelengths (from Kane, 1974).

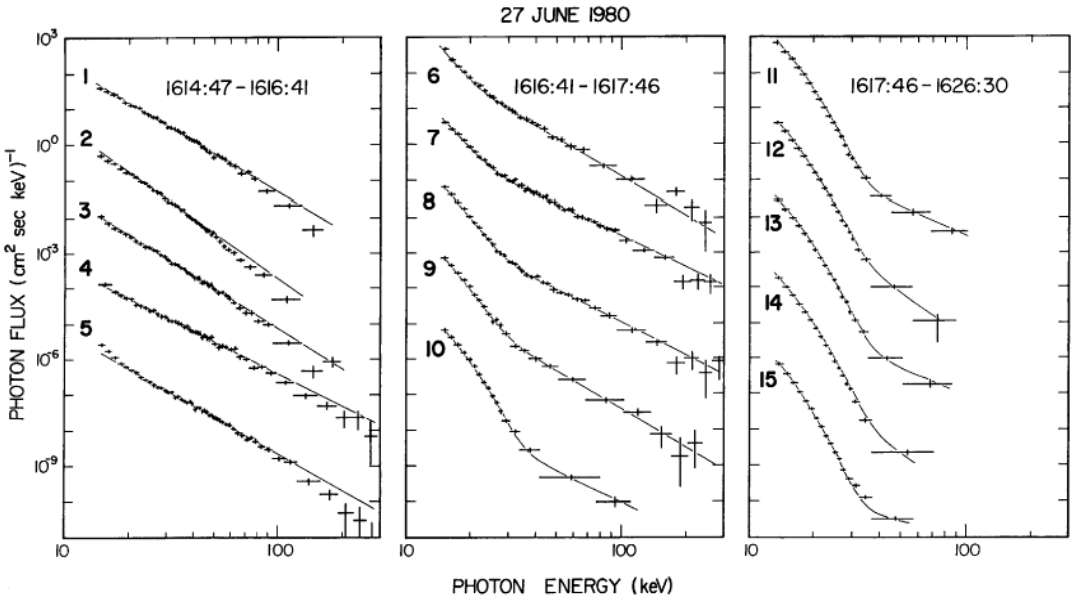

Figure 1.4: Energy spectra of the HXR photon flux observed in the 1980 June 27 flare (from Lin et al., 1981).

energy released via magnetic reconnection is expended for the particle acceleration (e.g., Duijveman et al., 1982). Thus accelerated particles play an important role in the energetics of the flare itself (Neupert, 1968). Therefore the study of non-thermal phenomena in solar flares is important to understand not only the particle acceleration mechanism but also the nature of the flare. We can utilize the observational data of HXRs and microwaves as a key diagnostic of the non-thermal electrons in solar flares.

1.2.1 Hard X-Rays (HXRs)

HXR emissions in solar flares, ranging from tens to hundreds keV, are widely believed to be generated by the interaction of high energy non-thermal electrons with an ambient plasma. This is a non-thermal bremsstrahlung radiation process. The HXR photon with energy ϵ is emitted by electrons with comparable energy. In the context of solar flares, there are two major approximated models of the non-thermal bremsstrahlung radiation, depending on the density of the target plasma. These are called "thin-target" and "thick-target" models (Brown, 1971). In the thin-target

model, it is assumed that the density of the target plasma is so low that parent electrons continue to emit HXRs by losing only a small fraction of their energy. This model can approximate the emission in the upper corona where the number density of the ambient plasma is $\lesssim 10^{10}$ cm^{-3}. In the thick-target model, on the other hand, it is assumed that parent electrons immediately lose all of their energy by Coulomb collisions with quite dense plasma. This model well describes the emission from the dense target region such as chromosphere where the number density of the ambient plasma is $\gtrsim 10^{13}$ cm^{-3}.

Recent solar-dedicated HXR imaging observatories of *Hinotori*, *SMM*, *Yohkoh*, and *RHESSI* have revealed the spatial distribution of HXRs. The HXR sources are mostly located at chromosphere, both ends of the flare loop called footpoints (Sakao, 1994, 1999, and Fig. 1.5), not in the corona. Therefore the thick-target model is suitable for describing the flare HXR emissions. If this model is adopted, one can relate the observed HXR emissions to parent electrons precipitating into the thick-target region. When the energy spectrum of the observed HXR photon flux is described by a power-law function with index γ, the energy distribution of the parent electron flux is approximated by a power-law with index $\delta = \gamma + 1$ (Hudson, 1972). The HXR observations are useful for a diagnostic of electrons with energy below several hundreds keV at the precipitation site.

There have been reported some exceptions. Lin et al. (1981) observed the HXR energy spectrum which have a Maxwellian component extending up to 30 keV (right plot of Fig. 1.4). This is emitted by the plasma with a temperature greater than 3×10^7 K, known as the "superhot thermal component". The "above-the-loop-top" HXR source found by Masuda et al. (1994) (Fig. 1.5) is one of the most striking results brought by *Yohkoh*. This is a strong evidence that the flare energy release and particle acceleration take place *above* the top of the loop seen in SXR which thus further supports the CSHKP model, though the origin of this source is still not clear because this is rarely observed. Recently Krucker et al. (2007) found 200-800 keV γ-ray emissions not only at the footpoint but in the corona by using *RHESSI*. These might be emitted by long-lived relativistic electrons in the corona.

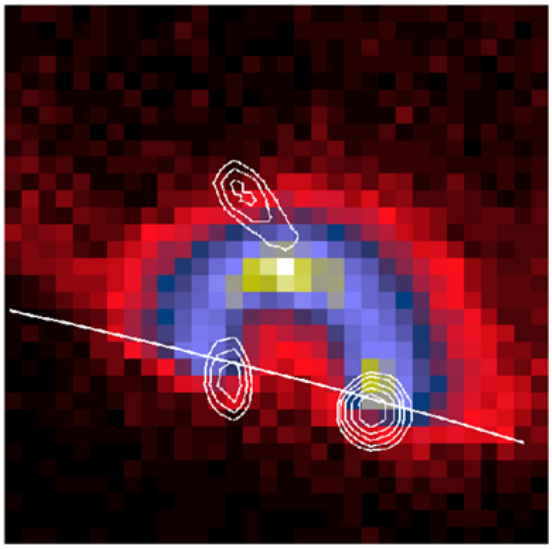

Figure 1.5: *Yohkoh* observation of the "above-the-loop-top" hard X-ray source on the 1992 January 13 flare ("Masuda" flare from Masuda et al., 1994). Background color is the soft X-ray image taken with the Soft X-ray Telescope (SXT; Tsuneta et al., 1991). White contours show the hard X-ray image taken with the hard X-ray Telescope (HXT; Kosugi et al., 1991). White thick line represents the solar limb. Solar north is to the left and west is up. Three HXR sources can be found: footpoint HXR sources at the both ends of the SXR loop, and an additional source located *above* the top of the loop.

1.2.2 Microwaves

When a flare occurs, intense microwave emissions in gigahertz range are observed with ground-based observatories such as *VLA*[4], *OVRO*[5], NoRP[6] and NoRH[7]. Since these light curves have a similar profile to those of HXRs, these microwaves are also of non-thermal. It is widely believed that gigahertz microwaves are generated by high energy non-thermal electrons gyrating in a magnetic field with a strength of

[4] *Very Large Array.*

[5] *Owens Valley Radio Observatory.*

[6] Nobeyama Radio Polarimeters (Nakajima et al., 1985).

[7] Nobeyama Radioheliograph (Nakajima et al., 1994).

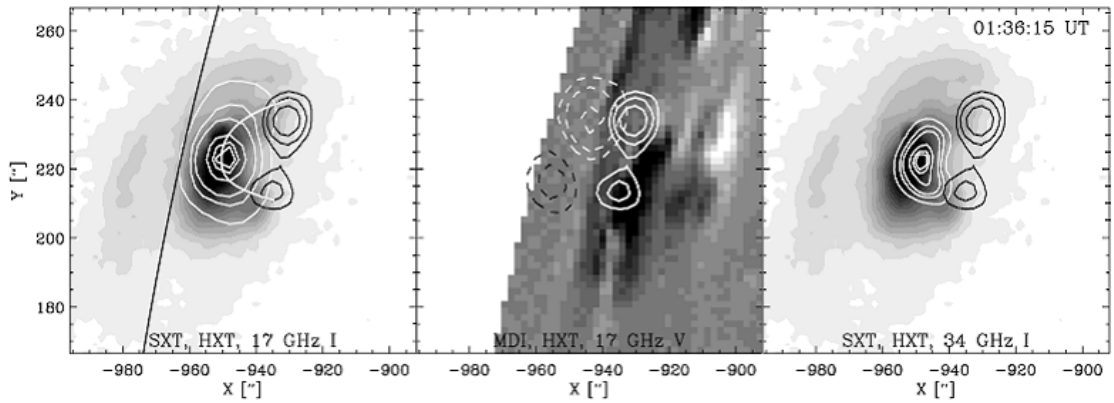

Figure 1.6: NoRH and *Yohkoh* observations of a solar flare occurred on 2000 January 12 (from Kundu et al., 2001). Solar north is up and west is to the right. *Left*: The NoRH 17 GHz brightness temperature image (white contours) and the HXT 33-53 keV image (black contours). Background image is the SXT image. *Center*: The NoRH 17 GHz polarization image (dashed white and black contours for positive and negative) and the HXT image (white contours). Background image is the *SOHO*/MDI magnetogram. *Right*: Same as the left map, but for the NoRH 34 GHz.

several tens to thousands Gauss. This is an incoherent synchrotron radiation from mildly-relativistic electrons, called the "gyrosynchrotron" radiation (Ramaty, 1969; Takakura, 1972; Petrosian, 1981; Dulk, 1985). Since the gyrosynchrotron radiation process is intricately dependent on many physical parameters, the relationship between the profile of radiation and that of parent electrons is not so simply expressed compared to the bremsstrahlung HXR. When the magnetic field strength at the emission site is $\sim$ 1000 Gauss and an observation frequency is fixed to be $\sim$ 10 GHz, an effective energy of (optically thin) gyrosynchrotron-emitting electrons is several hundreds keV (Bastian, 1999). The effective energy increases with decreasing the magnetic field strength and increasing the observation frequency. When the magnetic field strength is $\sim$ 100 Gauss, an effective energy for the $\sim$ 10 GHz gyrosynchrotron radiation is $\sim$ 1 MeV.

The solar-dedicated radio interferometer such as *OVRO* and NoRH provide two-dimensional maps, which reveal the spatial distribution of microwaves. Figure 1.6 shows the NoRH and *Yohkoh* observations of a solar flare (Kundu et al., 2001). The strong microwave emission site does not coincide with the HXR sites. The microwave

source is typically located at the top of the loop which connects the footpoint HXR sources (Melnikov et al., 2002). Since the magnetic field strength at the loop top must be weaker (order of 100 Gauss) than that at the footpoints (order of 1000 Gauss), the loop-top microwave source shows a signature of ~ 1 MeV electrons around there. The microwave observations are useful for a diagnostic of electrons with energy ~ 1 MeV in the loop.

These two non-thermal emissions with different wavelengths, HXRs and microwaves, provide us information of the electrons at different sites and in different energy ranges. These are key clues for revealing the origin of flare non-thermal electrons.

1.3 Electron Kinematics

From many observations, there is no doubt that non-thermal electrons are produced up to several MeV or more within a timescale of 1 s or less (corresponds to a duration of elementary spikes of non-thermal light curves, e.g., Kiplinger et al., 1983, 1984; Machado et al., 1993) at somewhere in solar flares, propagate in the solar corona, and finally reach their emission sites and radiate HXRs and microwaves. Since what we can know from the HXR and microwave observations is the electron distribution at their emission sites, theoretical works are of help to deduce the distribution of electrons when they are accelerated and propagating. Here we introduce previous theoretical works on the modeling of electron acceleration and transport, and then raise questions which motivate us to work with this thesis.

1.3.1 Acceleration Models

Since a solar flare is triggered by magnetic reconnection, electron acceleration is also associated with magnetic reconnection. The electron acceleration in magnetic reconnection, which is commonly seen both in solar flares and Earth's magnetosphere (Terasawa et al., 2000), is a big issue for plasma physics to be solved. In the context of solar flares, many candidates of electron accelerator such as electric fields, waves, and shocks are proposed so far. We briefly review these schemes (see also Aschwanden, 2002).

In magnetic reconnection regions (diffusion regions) where particles are no longer frozen into magnetic field lines, strong electric fields are generated. Electrons can be accelerated along the X-line (for two-dimensional picture of CSHKP model) by such electric fields. This is called Direct Current (DC) field acceleration. They are distinguished for weak and strong electric fields, depending on whether the field strength is smaller or larger than the critical Dreicer field, called sub-Dreicer and super-Dreicer fields. The critical Dreicer field is responsible for the collisional deceleration force by Coulomb collisions. When the strength of electric fields is sub-Dreicer, a part of seed electrons with their initial speed larger than the critical speed (runaway speed) can overcome the deceleration force and then are accelerated. This scenario is applied for solar flares by Holman (1985), Tsuneta (1985), and Benka & Holman (1994). If the strength of electric fields is super-Dreicer, all of seed electrons can be freely accelerated. Such situation is studied by Litvinenko (1996).

After the acceleration at diffusion regions, electrons are ejected toward the reconnection downstream region with being frozen into the magnetic field lines (Fig. 1.7). In the situation of solar flares, the reconnected field moves toward the solar surface that shortens its spatial length along the field line and increases its magnetic field strength. During this convection, electrons can be adiabatically accelerated with conserving two different adiabatic invariants: the longitudinal adiabatic invariant and the magnetic moment. When the length of the reconnected field line decreases, electrons can gain parallel energy by the conservation of the longitudinal adiabatic invariant (Somov & Kosugi, 1997). When the magnetic field strength increases, electrons can gain perpendicular energy by the conservation of the magnetic moment (Karlický & Kosugi, 2004).

Furthermore, electrons might be stochastically accelerated via wave-particle interactions. Miller et al. (1996) proposed a scenario of electron transit-time damping acceleration by the resonance of electrons and electromagnetic waves such as fast-mode magnetohydrodynamic (MHD) waves. Shimada et al. (1997) considered that electrons are stochastically accelerated by repeatedly crossing a pair of slow-mode shock fronts which are predicted by the Petschek-type magnetic reconnection model (Petschek, 1964).

When a fast reconnection outflow collides with underlying pre-formed flare loops,

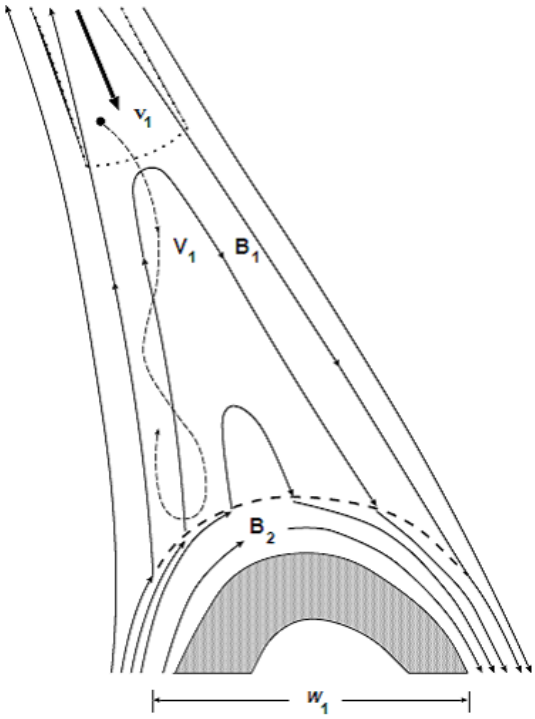

Figure 1.7: Schematic picture of magnetic trap (called "collapsing trap") in the reconnection downstream region (from Somov & Kosugi, 1997). Electrons are preaccelerated at the diffusion region and then are ejected from there (thick arrow at the upper left). They move downward with being frozen into the magnetic field. During this convection, they can be adiabatically accelerated both in parallel and perpendicular directions with respect to the magnetic field line. If the shock (dashed line) is formed above the underlying loop (grey), they might be further accelerated.

shocks might be created. Electrons have a possibility to be accelerated at the shocks. Tsuneta & Naito (1998) developed a scenario of an efficient electron acceleration by the first-order Fermi process at a fast oblique shock, motivated by the discovery of the "above-the-loop-top" HXR source (Fig. 1.5).

As seen, there are many possible candidates of the electron accelerator, but none of them is conclusive so far. To discuss which proposed model works the most efficiently, we have to determine from the observation the electron energy and pitch-angle distribution at the acceleration site. However, this is not identical to that at the emission site because electrons should take a finite time and distance to reach the emission site from the acceleration site. During this transport, electrons change their phase space

distribution because a transport process is energy-dependent (velocity-dispersive). We need an electron transport model for the determination of the electron distribution at the acceleration site.

1.3.2 Transport Models

In solar flares (more generally, magnetic reconnection), electrons ejected from diffusion regions propagate toward the downstream region with being frozen into the magnetic field lines. They can freely move along the magnetic field lines, but are limited to move perpendicular to the magnetic field lines. Therefore it is a good approximation for a treatment of electron transport to consider only the parallel motion along the magnetic field line. However, the magnetic field lines moving toward the solar surface can yield electron acceleration via such as the adiabatic processes (§ 1.3.1). In this regard, electron transport and acceleration take place simultaneously that makes a problem quite complicated. For a first step of the understanding of electron transport, one distinguishes different physical processes by assuming that they occur in sequential order.

Aschwanden (1998) provided a framework of the study of electron kinematics of acceleration, transport, and radiation. This is illustrated in Figure 1.8. He divides the electron kinematics into following different processes:

1. electron acceleration (treated as a "black box"),
2. electron injection into a static magnetic loop,
3. electron transport along the magnetic loop,
4. energy loss by radiation (HXRs and microwaves).

We call this framework the "injection model". The aim for the study of the injection model is to determine the injection condition (process 2), which can be a clue to know the property of acceleration, by modeling the electron transport (process 3) and using the observations (process 4) as a constrained condition.

Aschwanden further subdivided the electron transport into two different (but occurring in parallel) types: direct precipitation and trapping (plus precipitation or

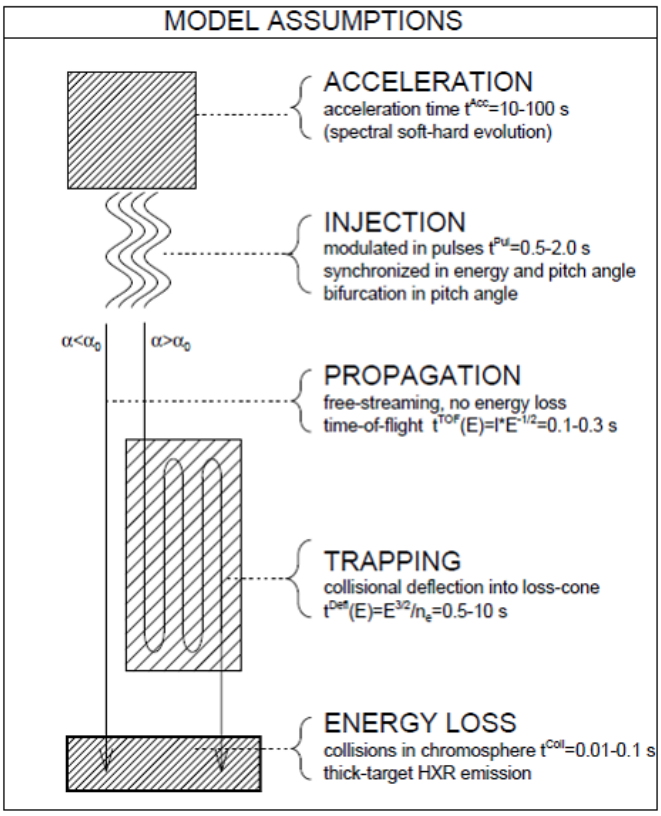

Figure 1.8: Conceptual breakdown of the electron kinematics into different physical processes (from Aschwanden, 1998).

not). Since a flare loop must be a converging magnetic loop, injected electrons can be categorized into two different types, depending on their pitch angles. Electrons with small pitch angle can freely stream along the loop without the magnetic trapping, and directly reach the footpoints of the loop. They emit HXRs at there. Electrons with large pitch angle are, on the other hand, magnetically trapped within the loop. These trapped electrons would emit microwaves. If the pitch-angle scattering works, they can reach the footpoints and then emit HXRs.

Based on this framework and a statistical analysis of the HXR data, Aschwanden et al. (1997, 1999) discussed the injection site and the physics of electron transport.

From the high-pass filtered HXR data taken with the BATSE[8] on board *CGRO*[9], they found that light curves of higher energy HXRs lead those of lower energy ones. They interpreted this as velocity-dependent electron time-of-flight differences and concluded that the injection site is located above the top of the flare loop. This is in agreement with the Masuda flare (Fig. 1.5). From the low-pass filtered HXR data, they found that light curves of higher energy HXRs lag those of lower energy ones. They interpreted this as a consequence of the electron trap-plus-precipitation (Melrose & Brown, 1976): electrons once trapped in the loop are scattered via Coulomb collisions, then subsequently precipitate into the footpoints and radiate HXRs.

In Aschwanden et al.'s studies, the electron energy and pitch-angle distribution at the injection site was not clarified. The microwave observation is suitable to discuss the pitch-angle distribution because the gyrosynchrotron radiation depends on the pitch angle of parent electrons. For example, Melnikov et al. (2002) explained the loop-top microwave sources based on the injection model (Fig. 1.9). They calculated spatial distributions of electrons and microwaves along a loop, and concluded that the loop-top microwave source can be realized if electrons are injected into a loop with a pitch-angle distribution concentrated perpendicular to the magnetic field line (bottom plots). In this study, they assumed a perfect trap (ignoring the trap-plus-precipitation effect) and a steady state of electrons.

1.4 Aim of This Thesis

The injection model is useful to study the electron acceleration in solar flares, and thus many authors have worked with this model. In the previous works, there are some simplifications. In the modeling of the electron transport, some works ignored temporal variation or spatial variation along a loop. The energy and/or pitch-angle distribution of electrons, which is the most important quantity for the determination of the electron acceleration mechanism, could not explicitly be addressed. Previous models are compared with some aspects of either the HXR or microwave observation. So far no one could implement a study to describe the temporal and spatial

[8] Burst and Transient Source Experiment

[9] *Compton Gamma-Ray Observatory*

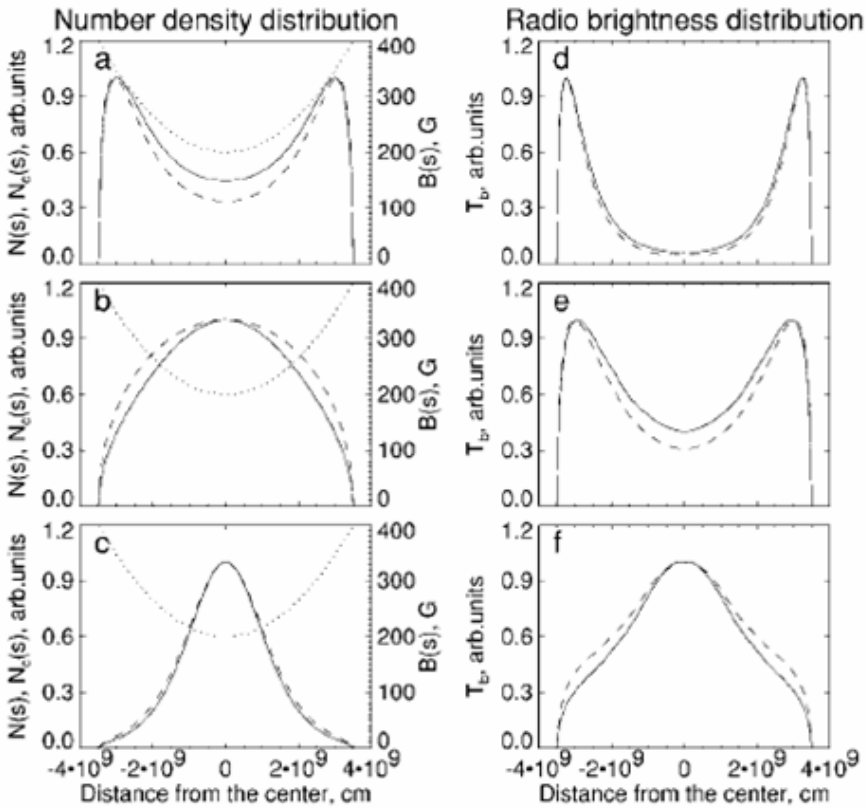

Figure 1.9: Normalized spatial distributions of electron number density (left) and 34 GHz gyrosynchrotron intensity (right) along a loop (from Melnikov et al., 2002). The pitch-angle distribution of the injected electrons is beamlike (top), isotropic (middle), and pancake (bottom), respectively.

variations of the electron distribution in energy and pitch-angle space, for comparison with temporal, spatial, and spectral variations of both the HXR and microwave observations.

The aim of this thesis is to determine the energy and pitch-angle distribution of accelerated electrons, for the understanding of the electron acceleration in solar flares. We perform both the observational and theoretical studies. In the observational study, we reveal variability of non-thermal emissions in time, space, and spectrum, by using both the HXR data (taken with *RHESSI*) and the microwave data (taken with NoRH and NoRP). In the theoretical study, we refine the injection model by treating a general form of the Fokker-Planck equation, which describes the time evolution of

the electron energy and pitch-angle distribution along the magnetic loop. This model allows us more rigorous discussions and understanding of the kinematics of flare non-thermal electrons than before, by comparing with the temporally-, spatially-, and spectrally-resolved observations.

This thesis proceeds as follows. In chapter 2 we overview a solar flare occurred on 2003 May 29, which is selected for our main study in this thesis. We present observation results taken with *TRACE*, *RHESSI*, NoRP, and NoRH. We distinguish this flare for two different phases, the early and main impulsive phases. We first analyze the observations in the main impulsive phase, focusing on characteristics of HXRs above 100 keV. We also consider the electron transport to explain the observations and determine the pitch-angle distribution of the injected electrons. These studies are presented in chapter 3. In chapter 4 we analyze the observations in the early impulsive phase, focusing on the spatial distribution of non-thermal emissions. We consider a possible electron acceleration model to explain the observations. In chapter 5 we analytically and numerically study the propagating feature of the non-thermal microwave source in the 1999 August 28 flare observed by Yokoyama et al. (2002), to determine the pitch-angle distribution of the injected electrons. Finally we present conclusions and discussion of this thesis in chapter 6.

Chapter 2

Overview of the 2003 May 29 Flare

We briefly overview observations of the 2003 May 29 flare, which we mainly study in this thesis. This flare occurred at S07°, W31° (Figure 2.1) at 00:50 UT, and lasted about 1 hour. The *GOES* soft X-ray (SXR) level was X1.2 (Figure 2.3, top). The halo coronal mass ejection (CME) associated with this flare was observed by the Large Angle and Spectrometric Coronagraph (LASCO) on board the *Solar and Heliospheric Observatory* (*SOHO*; Domingo et al., 1995). Multi-wavelength observations by space-based as well as ground-based instruments were performed: optical to extreme ultraviolet observations with the *Transition Region and Coronal Explorer* (*TRACE*; Handy et al., 1999), X-ray observations with the *Reuven Ramaty High Energy Solar Spectroscopic Imager* (*RHESSI*; Lin et al., 2002), and microwave observations with the Nobeyama Radio Polarimeters (NoRP; Nakajima et al., 1985, and references their in) and the Nobeyama Radioheliograph (NoRH; Nakajima et al., 1994). We select this flare for the study from a lot of flares observed with *RHESSI* since its operation start in February 2002 because of the following reasons: (1) good coverage of the *RHESSI* observation without interruptions by South Atlantic Anomaly transits and the satellite night. *RHESSI* detected a large amount of high energy (> 100 keV) hard X-rays (HXRs); and (2) simultaneous observations with NoRP and NoRH.

In the following sections we present an observation summary of *TRACE*, *RHESSI*, and NoRP/NoRH. Detailed studies on variability of non-thermal emissions in this flare is presented in chapters 3 and 4.

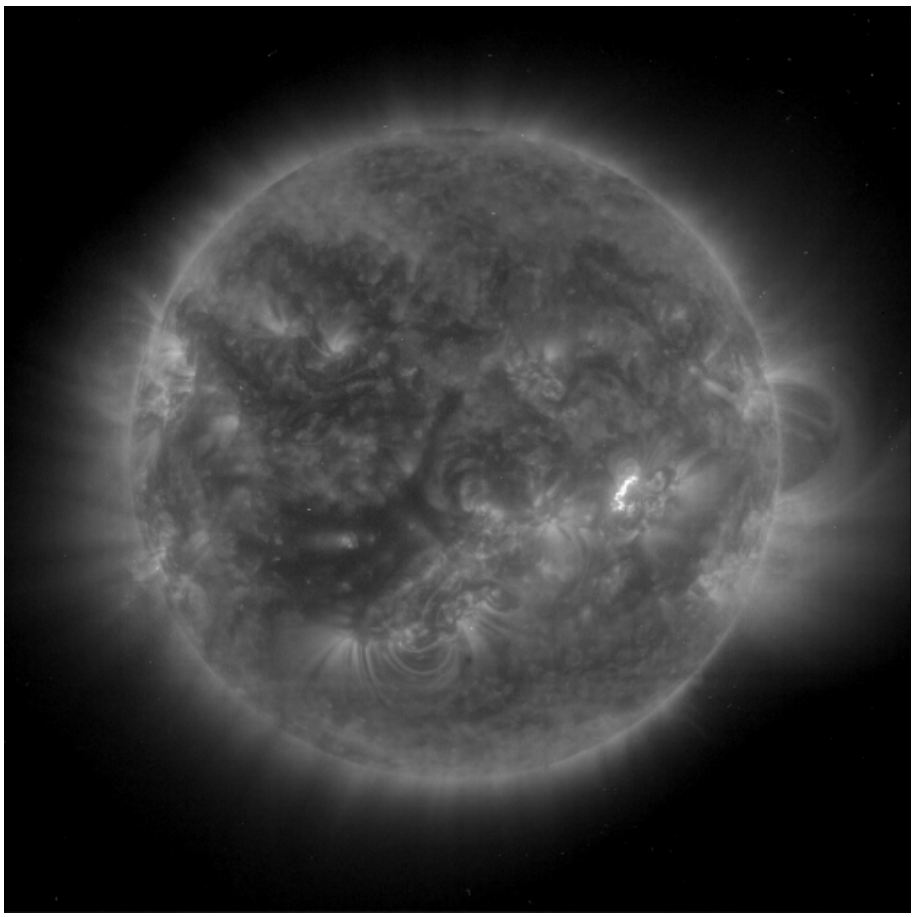

Figure 2.1: The extreme ultraviolet (171 Å) image taken with *SOHO*/EIT at 01:00:16 UT on 2003 May 29. Solar north is up and west is to the right.

2.1 TRACE Observation

TRACE observed this flare with many passbands: white light (WL), ultraviolet (UV; 1700, 1600, 1550 Å), and extreme ultraviolet (EUV; 195 Å) channels. Images taken with UV wavelengths show emissions from plasma in the chromosphere and low corona while those with EUV wavelengths show emissions primarily from coronal plasma with temperature ~ 1 MK. During this flare, WL and UV images of $1024'' \times 1024''$ with $0.5''$ pixels and EUV images of $512'' \times 512''$ with $1''$ pixels were taken. Field of view of these images was enough to cover the whole flare region. Unfortunately, time cadences of these images were not so high: approximately 18 s for EUV images and 4 minutes for WL and UV images.

It is known that the raw pointing data of *TRACE* has an error as much as $10''$ ($1'' \sim 700$ km) due to a minor flex of the metering tube on the spacecraft, though image offsets of the different wavelength channels are determined. We correct this uncertainty by performing a co-alignment analysis developed by Metcalf[1], using the white light images taken with both *TRACE* and the Michelson Doppler Imager (MDI) on board *SOHO* (e.g., Alexander & Coyner, 2006). The co-alignment analysis is performed with the data taken not only before the flare but also after the flare, to check that the offset of the pointing of *TRACE* did not drastically change during the flare. As a result, we evaluate coordinate shifts of approximately $-2.2''$ in the y-direction (north-south) and $-0.2''$ in the x-direction (east-west) from the raw pointing data.

Figure 2.2 shows the EUV (top) and UV (bottom) images taken with 195 Å and 1700 Å channels, respectively. The dashed contours are photospheric magnetic neutral lines obtained from the *SOHO*/MDI magnetogram. Since *SOHO* observes the Sun at the L1 point and this MDI magnetogram data was taken at 00:03:00 UT, we use the MDI data after correcting the parallax and the solar differential rotation. In the study of this flare (chapters 2 through 4), we use this corrected MDI data.

We first address the UV images (bottom panels of Fig. 2.2). Since these are plotted as negative images, black regions are the most brightest. The brightest regions are located at the both sides of the magnetic neutral line: the east one is located at the region with positive magnetic polarity and vice verse. They are elongated in north-south direction which is approximately parallel to the magnetic neutral line. They are called "flare ribbons", i.e., magnetically conjugate footpoints of bundles of the magnetic loops at the chromosphere. The loops, which are quasi-perpendicular to the magnetic neutral line, evolve toward north-south direction and form the arcade structure. This can be identified from the EUV image taken after the flare (top right panel) showing the post-flare loops. Both the UV ribbon structure at the chromosphere and the EUV arcade structure at the corona are frequently observed in flares (e.g., Asai et al., 2003). These are widely interpreted as a consequence of magnetic reconnection (Carmichael, 1964; Sturrock, 1966; Hirayama, 1974; Kopp &

[1] "Correcting *TRACE* Pointing with MDI WL Images or EIT EUV Images" at http://www.cora.nwra.com/~metcalf/TRACE/pointing.html

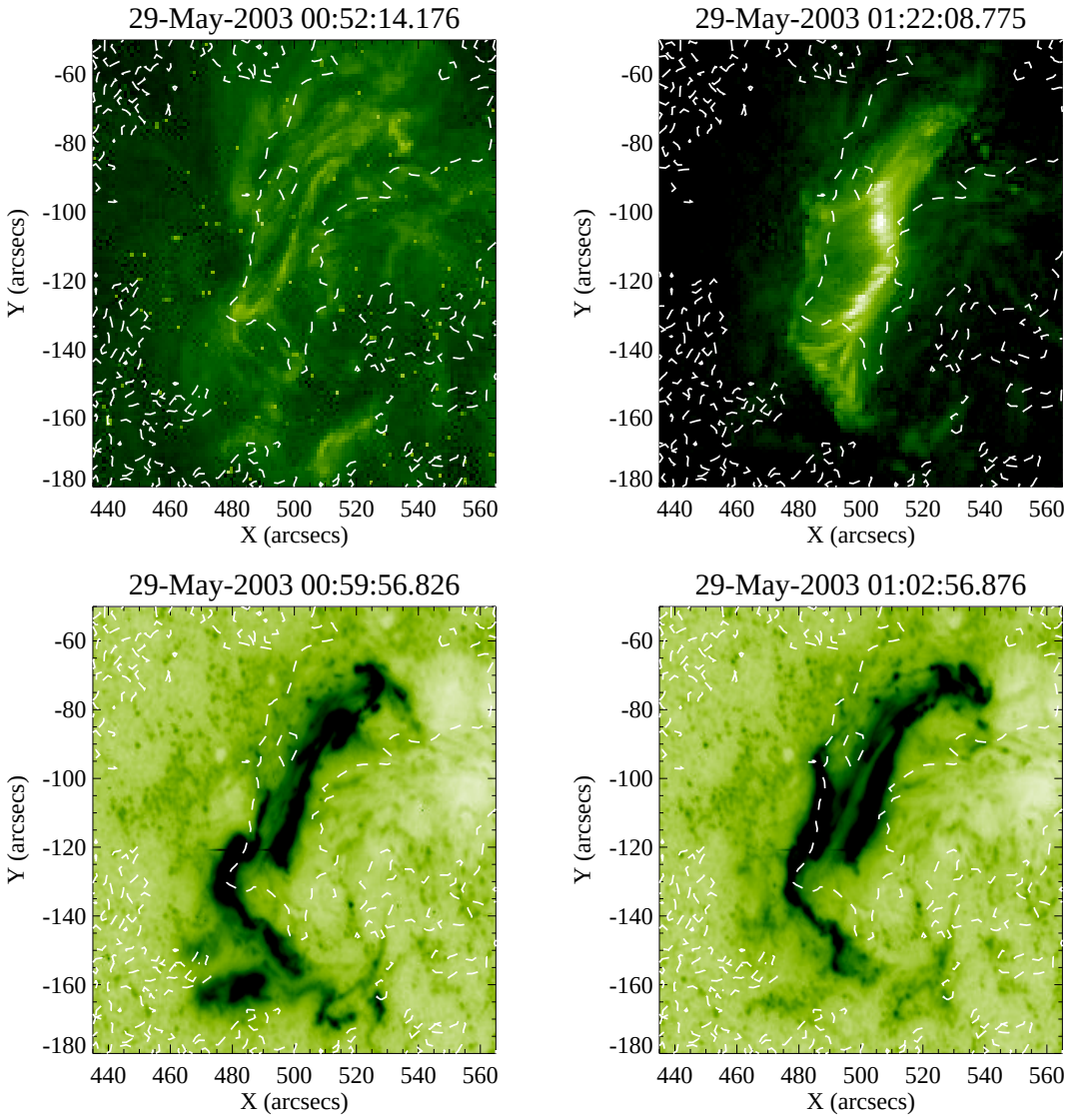

Figure 2.2: *TRACE* observation of the 2003 May 29 flare. Solar north is up and west is to the right. *Top*: 195 Å EUV images taken at 00:52:14 UT (left) and at 01:22:09 UT (right). *Bottom*: 1700 Å UV negative images taken at 00:59:57 UT (left) and at 01:02:57 UT (right). The dashed contours denote the photospheric magnetic neutral lines obtained from the *SOHO*/MDI magnetogram.

Pneuman, 1976, the CSHKP model). Though a detailed emission mechanism of UV radiation at ribbons is too complicated to be fully understood yet, they are interpreted as an evidence of the energy dissipation of non-thermal electrons as well as the thermal conduction precipitating into the chromosphere from the upper corona where they are produced via magnetic reconnection. Asai et al. (2004) presented the spatial distribution of the flare ribbons seen in Hα line and the photospheric magnetic field intensity, and explained their quantitative relationship based on the magnetic reconnection model.

We note other characteristics seen in *TRACE* images. The top left and bottom right panels of Figure 2.2 show the structure connecting the southeast site around [480, −130] with positive magnetic polarity to the northwest site around [530, −70] with negative magnetic polarity. This represents the sheared field line (quasi-parallel to the photospheric magnetic field line), which magnetically connects the two sites. The UV images (bottom panels) show the evolution of the spatial distribution of the ribbons. The east ribbon in the later time (bottom right panel) is located at the north region compared with that in the earlier time (bottom left panel). On the other hand, the spatial distribution of the west ribbon does not show significant change in north-south direction. This implies that the formation of sheared loops is followed by the formation of relaxed loops (quasi-perpendicular to the photospheric magnetic field line) with the flare progress. Subsequently, both the east and west ribbons move toward east-west direction and separate from each other. This is an evidence of successive magnetic reconnection. From a time series of the *TRACE* images, we estimate the velocity of the separation motion to be roughly 10 km s^{-1}.

2.2 RHESSI Observation

RHESSI detected a large amount of HXRs during 01:00:00 - 01:05:30 UT. We define this period as the impulsive phase. During this period, *RHESSI* was operated with an attenuator state of 3 (Smith et al., 2002): both the thick and thin shutters were in front of the detectors to keep them from being saturated at high counting rates of low energy photons, and to reduce their deadtime and the pulse pileup effect. We obtain well reliable and calibrated HXR data especially above 40 keV.

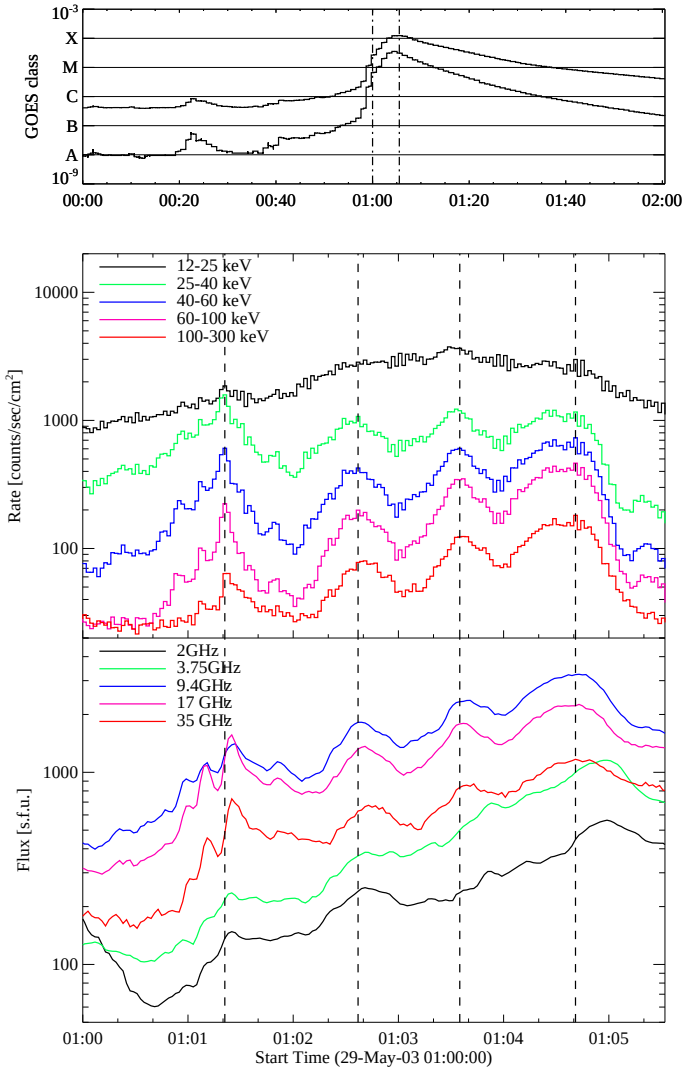

Figure 2.3: Light curves for the 2003 May 29 flare. *Top*: The *GOES* SXR light curves with two channels of 1-8 Å (top) and 0.5-4 Å (bottom) during 00:00 - 02:00 UT. The period during 01:00:00 - 01:05:30 UT (dot-dashed lines) is defined as the impulsive phase. *Bottom*: Light curves of the non-thermal emissions during the impulsive phase. The upper part shows the HXR light curves (in units of counts/sec/cm^2) taken with *RHESSI* in five energy bands: 12-25, 25-40, 40-60, 60-100, and 100-300 keV from top to bottom. The lower part shows the microwave light curves (S.F.U. = 10^{-19} erg/s/cm^2/Hz) observed in the NoRP 2, 3.75, 9.4, 17 and 35 GHz bands. The dashed lines denote the peak times of each spike in the 40-60 keV.

The upper part of the bottom plot of Figure 2.3 shows the HXR light curves taken with *RHESSI* in five energy bands: 12-25, 25-40, 40-60, 60-100, and 100-300 keV with a time resolution of 2 s. The HXR light curves, except in 12-25 keV, consist of four spikes. We confirm that these emissions are of non-thermal from spectral analysis in chapter 3. The HXR light curve in 12-25 keV shows smooth rather than spiky profile. This is attributed to a contamination of emissions from thermal plasma to those from non-thermal electrons.

Figure 2.4 shows the spatial distribution of 40-100 keV HXRs at the peak times of four spikes, overlaid on the *SOHO*/MDI magnetogram. These *RHESSI* images are reconstructed with the CLEAN algorithm (Hurford et al., 2002) using collimators 3-6 which give an angular resolution of $\sim 7''$. The accumulation time for making these images is 12.48 s, which is triple periods of the *RHESSI* rotation (4.16 s) during the impulsive phase.

The *RHESSI* maps at 40-100 keV show double sources located at regions of opposite magnetic polarity and within the ribbons seen in UV (bottom panels of Fig. 2.2). Therefore, these HXRs are emitted near the footpoints of a loop, called double-footpoint sources. However, there is a considerable difference of the spatial distribution between the HXR and UV, in spite that both of them show the energy dissipation sites at the footpoints of the loops. The HXR sources appear in compact regions, while the UV ribbons show the elongated structure. Though there are a few HXR observations showing the ribbon structure (Masuda et al., 2001; Liu et al., 2007; Jing et al., 2007), such difference of the spatial distribution between the HXR and UV is quite commonly seen in flares. One explanation proposed by Asai et al. (2002) is that a loop with footpoint HXR sources has a stronger magnetic field intensity than other loops without footpoint HXR sources, and thus the strong energy release and particle acceleration are expected.

A time series of the *RHESSI* images show the temporal evolution in the HXR sources. The location of the HXR sources during the first peak indicates that the loop connecting them is sheared with respect to the magnetic neutral line. During the second through last peaks, the loop connecting HXR sources is less sheared. The HXR sources during these periods move toward parallel to (northward) as well as perpendicular to the photospheric magnetic neutral line, similar to the UV ribbons.

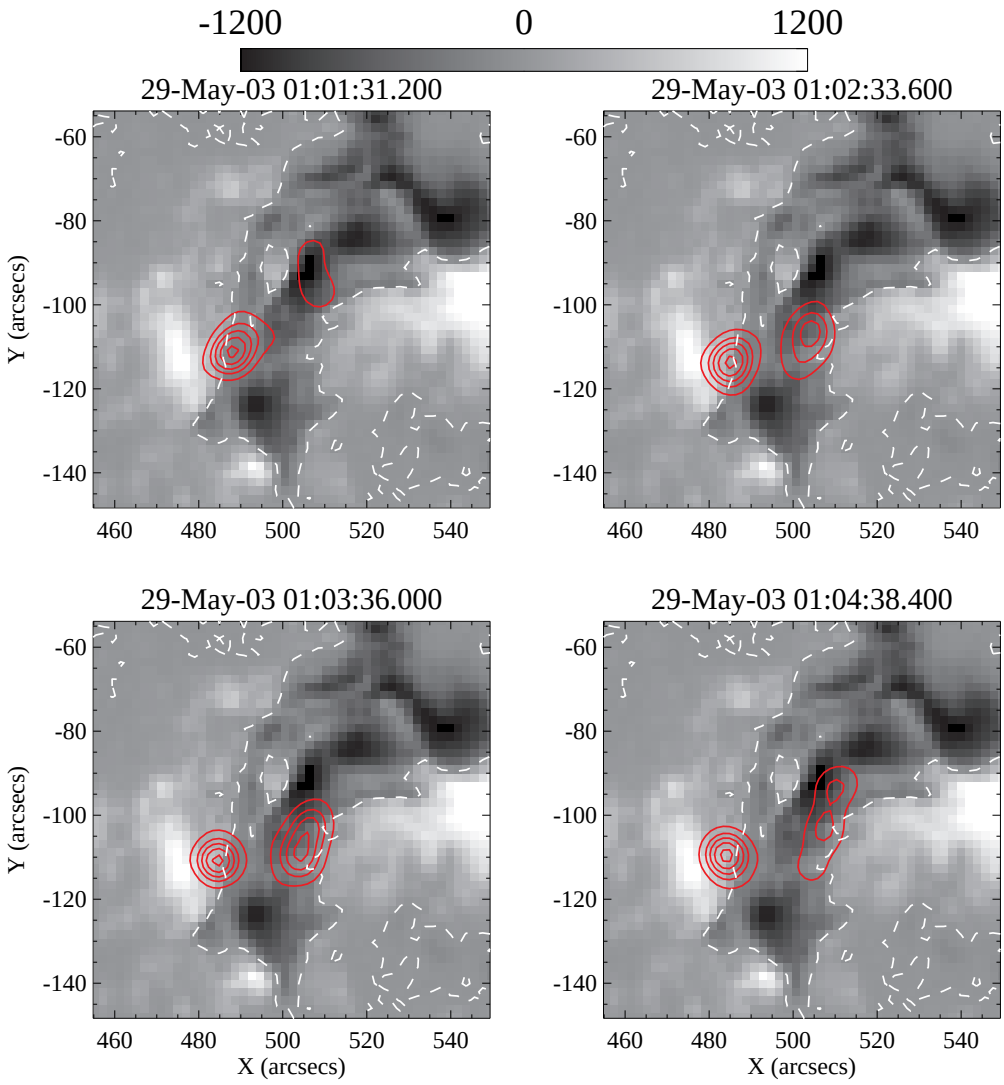

Figure 2.4: Spatial distribution of HXRs during the impulsive phase of the 2003 May 29 flare. The *RHESSI* 40-100 keV contours (red) at 01:01:31 UT (top left), 01:02:34 UT (top right), 01:03:36 UT (bottom left), and 01:04:38 UT (bottom right) are overlaid on the *SOHO*/MDI magnetogram (in units of Gauss). Contour levels are 35%, 50%, 65%, 80%, 95% of the peak intensity in each image. The dashed contours denote the photospheric magnetic neutral lines. Solar north is up and west is to the right.

The velocity of the HXR source motion is roughly estimated from the position of each source centroid, ~ 10 km s^{-1}. This is also in agreement with the UV ribbons.

2.3 Microwave Observation

2.3.1 NoRP Observation

NoRP observes the total microwave flux with multiple frequencies of 1, 2, 3.75, 9.4, 17, 35, and 80 GHz with a time resolution of 0.1 s. Within them, the microwave light curves at 2 through 35 GHz are shown in the lower part of the bottom plot of Figure 2.3. At lower frequencies (2 through 9.4 GHz) the total microwave fluxes increase with increasing frequency, indicating that they are in the optically thick regime. At higher frequencies (9.4 through 35 GHz) they decrease with increasing frequency, and their light curves show four spikes that are almost simultaneous with the HXR ones. This indicates that the 17 and 35 GHz microwaves are optically thin, non-thermal gyrosynchrotron radiation (Ramaty, 1969; Petrosian, 1981; Dulk, 1985). This assertion is further confirmed from spectral analysis in chapter 3.

2.3.2 NoRH Observation

NoRH observes the Sun in the microwave range. Full Sun intensity maps at two frequencies of 17 GHz and 34 GHz are synthesized from the obtained data with the image reconstruction technique of the CLEAN algorithm. Figure 2.5 shows the spatial distribution of the 17 (left) and 34 GHz (right) brightness temperature at 01:04:39 UT. The spatial resolution of them depends on the observation frequency, $\sim 18''$ for 17 GHz and $\sim 9''$ for 34 GHz. The 17 and 34 GHz microwaves show similar structure: an elliptical shape located between the footpoint HXR sources. This geometry is seen during the course of the impulsive phase. Comparing this with the one in EUV (top right panel of Fig. 2.2), we consider that the microwaves correspond to (unresolved) bundles of the loops. We will confirm this speculation in chapter 3.

Though the spatial resolution of NoRH is lower than that of *TRACE* and *RHESSI*, its time resolution is the highest. Then the NoRH data is the most suitable for investigating the temporal variation of the morphology. We use the NoRH data

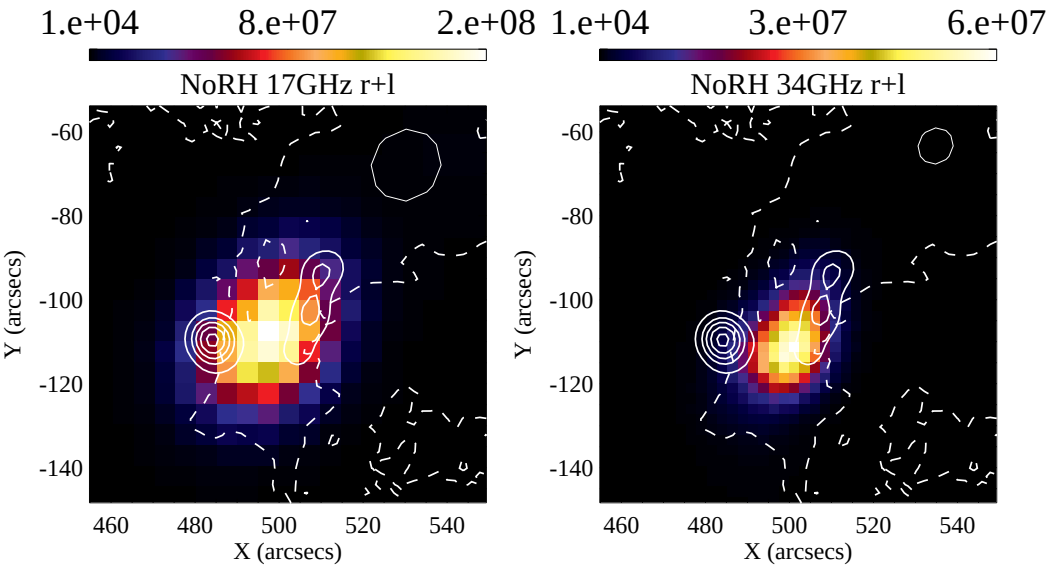

Figure 2.5: Spatial distribution of microwaves at 01:04:39 UT on 2003 May 29. The left and right maps are the NoRH 17 and 34 GHz brightness temperature (in units of kelvin) images. White circles in the upper right corner in each image denote the beam size at half-level of the peak intensity, giving the spatial resolution of $\sim 18''$ for 17 GHz and $\sim 9''$ for 34 GHz. The thick solid contours are the 40-100 keV HXRs, same as those shown in the bottom right panel of Figure 2.4. The dashed contours denote the photospheric magnetic neutral lines. Solar north is up and west is to the right.

synthesized with a integration time of 2 s, and describe the time evolution of the spatial distribution of the microwave sources by fitting them with a two-dimensional elliptical gaussian function (see, Appendix B for a method in detail). By this method, we obtain six number of gaussian parameters in each image: the peak brightness temperature $T_{\rm b}$, the position of the gaussian center x_0 and y_0, the gaussian full-width at half-maximum (FWHM) w_{MM} and w_{mm} in directions of major (M) and minor (m) axes of the ellipse, and the angle θ between m- and x-axes. The M-axes is oriented to the northwest direction, as can be found in Figure 2.5.

The shape of the observed microwave source is a convolved image of an actual microwave source by the beam pattern, which is different with different observation frequencies. The above fitting parameters are instrument-dependent, and then their quantitative comparison between different frequencies (17 GHz and 34 GHz) does not mean. However, since the observed shape of the source is enough larger than

the beam size and is well described by the gaussian distribution, we expect that an actual shape of the source is also roughly described by the gaussian distribution with parameters ($T_{\rm b}^{\rm a}$, $x_0^{\rm a}$, $y_0^{\rm a}$, $w_{MM}^{\rm a}$, $w_{mm}^{\rm a}$, $\theta^{\rm a}$), which are determined from the following manner (see, Appendix C):

$$\begin{cases} T_{\rm b}^{\rm a} = T_{\rm b}\left(\frac{w_{MM}}{w_{MM}^{\rm a}}\right)\left(\frac{w_{mm}}{w_{mm}^{\rm a}}\right), \\ x_0^{\rm a} = x_0, \\ y_0^{\rm a} = y_0, \\ \left(w_{MM}^{\rm a}\right)^2 = \left(w_{MM}\right)^2 - \left(w_{MM}^{\rm b}\right)^2, \\ \left(w_{mm}^{\rm a}\right)^2 = \left(w_{mm}\right)^2 - \left(w_{mm}^{\rm b}\right)^2, \\ \theta^{\rm a} \simeq \theta, \end{cases} \tag{2.3.1}$$

where $w_{MM}^{\rm b}$ and $w_{mm}^{\rm b}$ are the beam FWHM in M- and m-directions, respectively. The last approximation holds when the sharp of the beam is close to circle. Since these parameters are no longer instrument-dependent, we can quantitatively compare the parameters of 17 GHz with those of 34 GHz. Through these methods, we parameterize the 17 GHz and 34 GHz microwave sources at each time.

Figures 2.6 and 2.7 show the time profiles of the fitting parameters in equation (2.3.1) for 17 GHz and 34 GHz, respectively. The time profiles of them are similar to each other, and their evolution is in agreement with that seen in other wavelengths (*TRACE* and *RHESSI*). The third panel of Figure 2.6 shows that the y-position of the 17 GHz microwave source is around $-125''$ before 01:00:00 UT, and then it moves toward north direction and reaches around $-110''$ at 01:01:20 UT. This motion corresponds to the evolution of the east ribbon in *TRACE* (bottom panels of Fig. 2.2). The fifth panel of Figure 2.6 shows that the source size in m-direction, which is approximately perpendicular to the photospheric magnetic neutral line, gradually increases after 01:01:20 UT (peak time of the first spike). The velocity of this evolution is ~ 10 km s^{-1}. Therefore this corresponds to the separating motion of the footpoints of the loops, also seen in *TRACE* and *RHESSI*.

We consider from Figures 2.6 and 2.7 that there are two different stages in the impulsive phase of this flare. The evolution during the second through last peaks looks simple. The light curve shows slow variation (first panel) with e-folding times of ~ 30 s. The center position of the source does not change during this period (second and third panels). The source size gradually increases in m-direction (fifth panel), but

does not vary in M-direction (forth panel). These imply that the geometry during this period slowly evolves only in the direction perpendicular to the magnetic neutral line. This is explained by the two-dimensional CSHKP model (Fig. 1.2). On the other hand, the evolution during the rise phase of the first spike (01:00:00 - 01:01:20 UT) looks complicated. The light curve shows fast variation (first panel) with an e-folding time of $\sim$ 10 s. The center position of the source moves toward northwest direction (second and third panels). The source size drastically changes in M-direction (fourth panel). These imply that the geometry during this period impulsively evolves in the direction parallel to the magnetic neutral line, which might be beyond the scope of the CSHKP model.

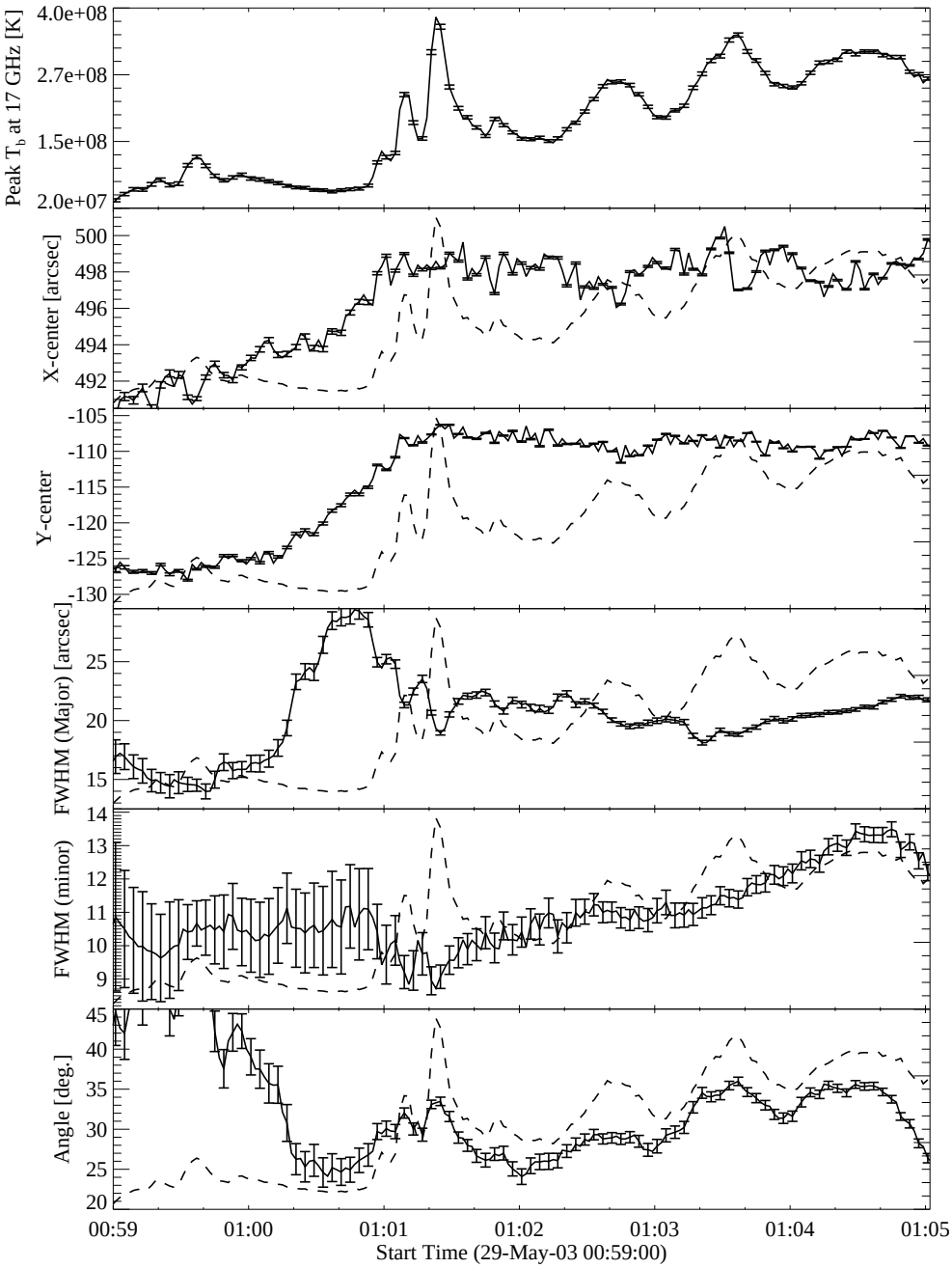

Figure 2.6: *From top to bottom*: Time profiles of the fitting parameters of the peak brightness temperature ($T_{\rm b}^{\rm a}$), the x and y position of the gaussian center ($x_0^{\rm a}, y_0^{\rm a}$), the FWHM in directions of major and minor axes ($w_{MM}^{\rm a}, w_{mm}^{\rm a}$), and the angle between m- and x-axes ($\theta^{\rm a}$) for 17 GHz. The dashed lines are $T_{\rm b}^{\rm a}$ (same as that shown in the top panel).

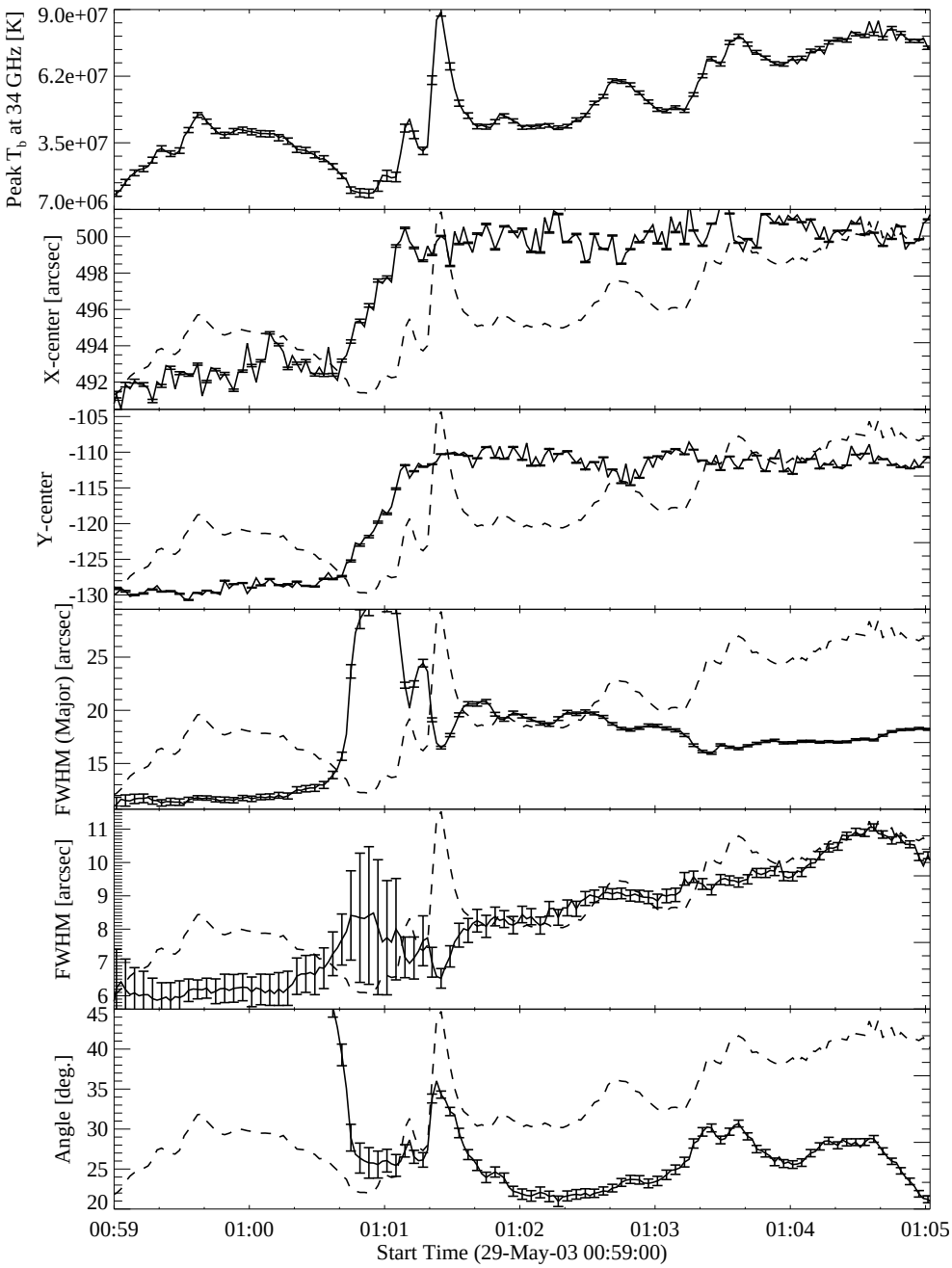

Figure 2.7: Same as Figure 2.6, but for 34 GHz.

2.4 Observation Summary

In this chapter we summarized the *TRACE*, *RHESSI* and NoRP/NoRH observations of the 2003 May 29 flare. This flare shows the ribbon and arcade structure, as observed with *TRACE*. This is the typical geometry of solar flares. In addition, we found the sheared structure which connects the southeast and northwest sites.

Non-thermal emissions of HXRs (up to 300 keV) and microwaves are observed. These light curves consist of four impulsive spikes during 01:00:00 - 01:05:30 UT (impulsive phase). We obtained the instrument-independent parameters of the shape of the microwave source, by performing the two-dimensional elliptical gaussian fit. From the time profiles of the parameters, we showed that this flare has two different stages in the impulsive phase. During 01:02:00 - 01:05:30 UT, the geometry slowly varied in the direction perpendicular to the magnetic neutral line, as also observed with *TRACE* and *RHESSI*. This can be understood by the two-dimensional CSHKP model. During 01:00:00 - 01:02:00 UT, on the other hand, the geometry looks complicated (three-dimensional) and varied impulsively.

By these results, we divide the impulsive phase into two different phases: periods during the first peak (01:00:00 - 01:02:00 UT, "early impulsive phase") and the subsequent peaks (01:02:00-01:05:30 UT, "main impulsive phase"). In chapter 3 we focus on the main impulsive phase to study the transport of non-thermal electrons both observational and theoretical points of view. In chapter 4 we focus on the early impulsive phase to study the energy dependence of the spatial distribution of non-thermal emissions.

Chapter 3

Comparative Analysis of Non-Thermal Emissions and Electron Transport in the Main Impulsive Phase*

In this chapter we analyze the non-thermal emissions during the main impulsive phase (01:02:00 - 01:05:30 UT) of the 2003 May 29 flare. In particular, we focus on characteristics of HXRs above 100 keV. We found that this emission shows intermediate characteristics between HXRs below 100 keV and microwaves: the spatial distribution coincides with the HXRs below 100 keV while the time profile of the spectrum is similar to the microwave. Further we consider the electron transport to explain the observation and determine the injection pitch-angle distribution. We found that the observed characteristics can be explained by the trap-plus-precipitation model (Melrose & Brown, 1976) in the weak diffusion regime. The observed characteristics of the HXRs above 100 keV suggest that the non-thermal electrons are accelerated more perpendicular to than parallel to the magnetic field lines until they are injected.

---

*This chapter was published in Astrophys. J., 2008, 673, 598, entitled "Comparative Analysis of Non-Thermal Emissions and Electron Transport in a Solar Flare" by T. Minoshima, T. Yokoyama, and N. Mitani.

3.1 Introduction

HXR and microwave observations of solar flares provide the most direct information on non-thermal electrons. Since HXRs below $\sim$ 100 keV are emitted primarily by electrons with energy below several hundred keV via bremsstrahlung radiation (Brown, 1971) whereas microwaves above $\sim$ 10 GHz are emitted by electrons above several hundred keV via gyrosynchrotron radiation (Ramaty, 1969; Dulk, 1985; Bastian et al., 1998), these two sources of emissions provide information about electrons in two different energy ranges. Therefore, a comparative study by using both HXR and microwave observations is useful for discussing the physics of flare non-thermal electrons over a wide range of energies.

Impulsive behavior is commonly seen in both HXR and microwave light curves (Kane, 1974), but the two emissions do not necessarily behave identically. Temporally, higher energy HXR and microwave emissions tend to be delayed from lower energy HXRs (e.g., Crannell et al., 1978; Nakajima et al., 1983; Cornell et al., 1984; Bai & Dennis, 1985; Aschwanden et al., 1997). Aschwanden et al. (1997) statistically analyzed the low-pass filtered HXR light curves for 78 flares observed with *CGRO* and found a systematic increase of time delay toward higher energy. They interpreted these time delays in terms of electron precipitation under Coulomb collisions.

Spatially, microwave sources do not always coincide with HXR sources. HXRs are typically emitted at the footpoint regions of the flare loop (Sakao, 1994) while microwaves are emitted mainly at the top of the loop (Kundu et al., 1994; Melnikov et al., 2002). This indicates that HXRs are emitted by electrons precipitating into the footpoints while microwaves are by electrons trapped within the loop. Melnikov et al. (2002) suggested that only electrons with a pancake pitch-angle distribution concentrated perpendicular to the magnetic field lines can explain the observed loop-top microwave source.

Spectrally, Silva et al. (2000) statistically studied the correlation of the HXR and microwave spectral indices for 57 peaks of the non-thermal emission in 27 flares. They found that the electron energy distribution inferred from the microwave spectrum is systematically harder than that inferred from the HXR spectrum, and suggested that the electron energy distribution becomes harder toward higher energy. There

are three probable explanations for such spectra: (1) two (or more) different electron populations with distinct physical characteristics, (2) "second-step acceleration" (e.g., Bai & Ramaty, 1976), and (3) "trap-plus-precipitation " (TPP; e.g., Melrose & Brown, 1976).

Melrose & Brown (1976) developed a model for electron transport, TPP, which describes the evolution of electrons at the trap region (trapped electrons) and those escaping from there (precipitating electrons). They presented analytic solutions of the electron energy continuity equation under two conditions: strong and weak diffusion limits (Kennel & Petscheck, 1966). In the strong diffusion limit, electrons injected into the trap region (magnetic loop) undergo significant scattering and then are quickly isotropized during the loop transit. They escape from the loop with a precipitation rate proportional to their velocity, $\nu_{\rm p} \propto v$. In the weak diffusion limit, on the other hand, electrons are less scattered during the transit. When the loss cone distribution is formed, the pitch-angle diffusion time $\tau_{\rm d}$, which is longer than the transit time, controls the electron precipitation, yielding $\nu_{\rm p} \propto 1/\tau_{\rm d}$. The precipitation rate and the evolution of electrons vary, depending on which condition applies.

Silva et al. (2000) pointed out in their study that the discrepancy of the energy distribution between the HXR- and microwave-emitting electrons could be explained by the TPP model. To confirm their suggestion the imaging observation is necessary, while it was not available in their study. If the HXR and microwave sources do not coincide spatially, the discrepancy of the energy distribution between the HXR- and microwave-emitting electrons can be explained in the TPP model as a consequence of the different spatial distributions of the HXR- and microwave-emitting electrons. Imaging as well as spectral data at both HXR and microwave wavelengths are essential to confirm the influence of TPP on the parent electrons.

We analyze the non-thermal emissions during the main impulsive phase (01:02:00 - 01:05:30 UT) of the 2003 May 29 flare by using *RHESSI*, NoRP and NoRH. *RHESSI* has superior spectroscopic ability from $\sim$ 3 keV to $\sim$ 17 MeV, providing the HXR spectrum from $\sim$ 3 to $\sim$ 300 keV with a spectral resolution of $\sim$ 1 keV and arbitrary energy bands. In previous studies, the temporal evolution of the (HXR) spectrum has been considered in less detail, probably due to instrumental limitations. However, temporally resolved analysis of the spectrum is important because non-thermal

emissions and thus non-thermal electrons are the most "time-varying" objects in solar flares. *RHESSI* enables us to analyze an accurate, temporally resolved HXR spectrum above $\sim$ 100 keV. Because the HXRs above $\sim$ 100 keV are mainly emitted by electrons above $\sim$ 200 keV (Aschwanden & Schwartz, 1996), *RHESSI*'s well-resolved spectral data below $\sim$ 300 keV provide us more accurate information on electrons from tens to hundreds of keV than before. Combining the *RHESSI* HXR and NoRH/NoRP microwave spectral data allows us to fully cover the electrons from tens to thousands of keV without gap, which has not been implemented so far due to a lack of detailed imaging and spectroscopic observations of HXRs above $\sim$ 100 keV.

For a physical interpretation of the observations, we adopt the injection model (§ 1.3.2). For the determination of injection properties based on the observations, we study the electron transport by developing a numerical model of TPP that treats the pitch-angle diffusion more generally than the analytic solutions developed for the weak and strong diffusion limits. Lee & Gary (2000) performed a similar analysis of the electron transport to explain their microwave observation of a flare on 1993 June 3. We also predict the microwave and HXR emissions from the calculated electron distribution. Comparing these model results with the observations, we discuss electron injection and transport, and address how the pitch-angle distribution of the injected electrons affects the evolution of the trapped and precipitating electrons, and their resulting emissions.

This chapter proceeds as follows. In § 3.2 we present a comparative study of the non-thermal emissions during the main impulsive phase, by using the *RHESSI* HXR and Nobeyama microwave observations. Temporally resolved spectra of the HXRs and microwaves are analyzed in detail. We discuss energy-dependent delays of the time profiles of the spectral indices, which have not been discussed in previous studies. In § 3.3 we present our treatment of the TPP model. We numerically solve the gyro-averaged Fokker-Planck equation (Hamilton et al., 1990) with the Coulomb interaction (Leach & Petrosian, 1981) and a time-dependent injection. In § 3.4 we describe the time evolution of the trapped and precipitating electron distribution and the predicted microwave and HXR emissions. The behavior of the HXR and microwave emissions predicted by the model are compared with the observations that allows us to give constraints on the properties of the injected electrons. In § 3.5 we

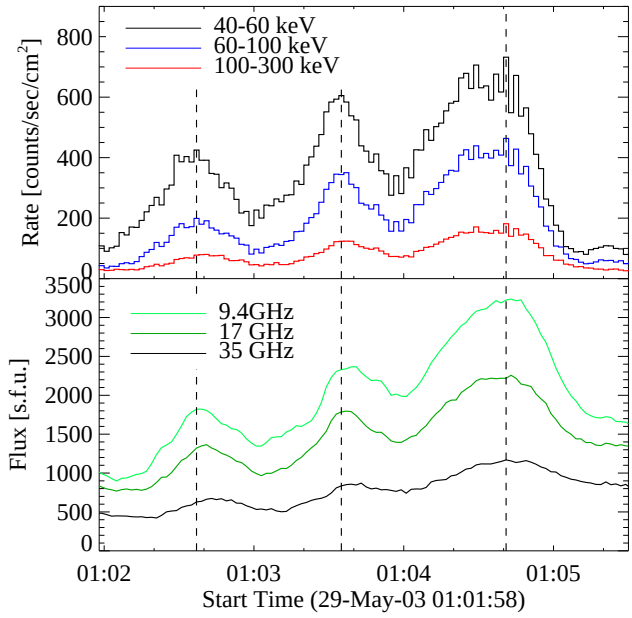

Figure 3.1: Light curves during the main impulsive phase of the 2003 May 29 flare. *Upper*: The *RHESSI* HXR light curves (in units of counts/sec/cm^2) in 40-60, 60-100, and 100-300 keV from top to bottom. *Lower*: The microwave light curves (S.F.U.) observed in the NoRP 9.4, 17 and 35 GHz bands from top to bottom. The dashed lines denote the peak times of each spike in the 40-60 keV band.

present the summary and discussion of this chapter.

3.2 Observations

The overall observation summary of the 2003 May 29 flare is presented in chapter 2. In this chapter we focus on detailed characteristics of light curves, images, and spectra of the non-thermal emissions in 01:02:00 - 01:05:30 UT.

3.2.1 Light Curves

The non-thermal light curves of HXRs (>40 keV) and microwaves (>9.4 GHz) are shown in Figure 3.1. In this plot, we denote the peak times of each spike in 40-60 keV band by the dashed lines. Though both the HXRs and microwaves show the similar

profile, the microwave peaks are delayed from the HXR peaks by about 4 s.

3.2.2 Images

Figure 3.2 shows the spatial distribution of the HXR emissions in the main impulsive phase. The top left map is the *RHESSI* 12-25 keV image overlaid on the *TRACE* 195 Å image. The top right, bottom left, and bottom right maps show the *RHESSI* images in three energy bands, 50-70 keV (black solid contours), 70-100 keV (blue), and 100-200 keV (red), during 01:02:00 - 01:03:00 UT, 01:03:00 - 01:04:00 UT, and 01:04:00 - 01:05:00 UT, respectively. The *RHESSI* images are reconstructed with the CLEAN algorithm (Hurford et al., 2002) using collimators 3-6 for 12-25 keV image and 3-5 for other images. An angular resolution of them is $\sim 7''$.

The *RHESSI* map at 12-25 keV (top left) is co-spatial with the brightest region in 195 Å image. Since 195 Å EUV is primarily emitted from coronal plasma, this indicates that the 12-25 keV HXRs are thermal bremsstrahlung radiation from the coronal plasma in the flare loop. This interpretation is supported by the smooth profile of the corresponding light curve (Fig. 2.3, black line).

The *RHESSI* maps above 50 keV (top right, bottom left, and bottom right) show double sources located at regions of opposite magnetic polarity with one of the sources lying at the edge of the bright region in 195 Å. Therefore, the HXRs in these energy ranges must be emitted near the footpoints of the loop. This has been already found in chapter 2. We emphasize that the 100-200 keV HXRs are emitted from the footpoints, co-spatial with the 50-100 keV HXRs (these contours are occulted by the red contours of 100-200 keV). There is no energy-dependent spatial distribution of the HXRs in 50-200 keV.

Note that the eastern HXR source is brighter than the western one. The magnetic field strength (see, Fig. 2.4) at the eastern source ($\sim +410$ Gauss) is weaker than that at the western one (~ -510 Gauss). Since a stronger HXR source indicates a more efficient electron precipitation, the spatial relationship between the HXR sources and the magnetic field strength can be interpreted as the result of magnetic mirroring of the HXR-emitting electrons (Sakao, 1994).

Figure 3.3 shows the 34 GHz brightness temperature and the degree of polarization at 17 GHz images taken with NoRH at 01:04:39 UT. The left map shows that the

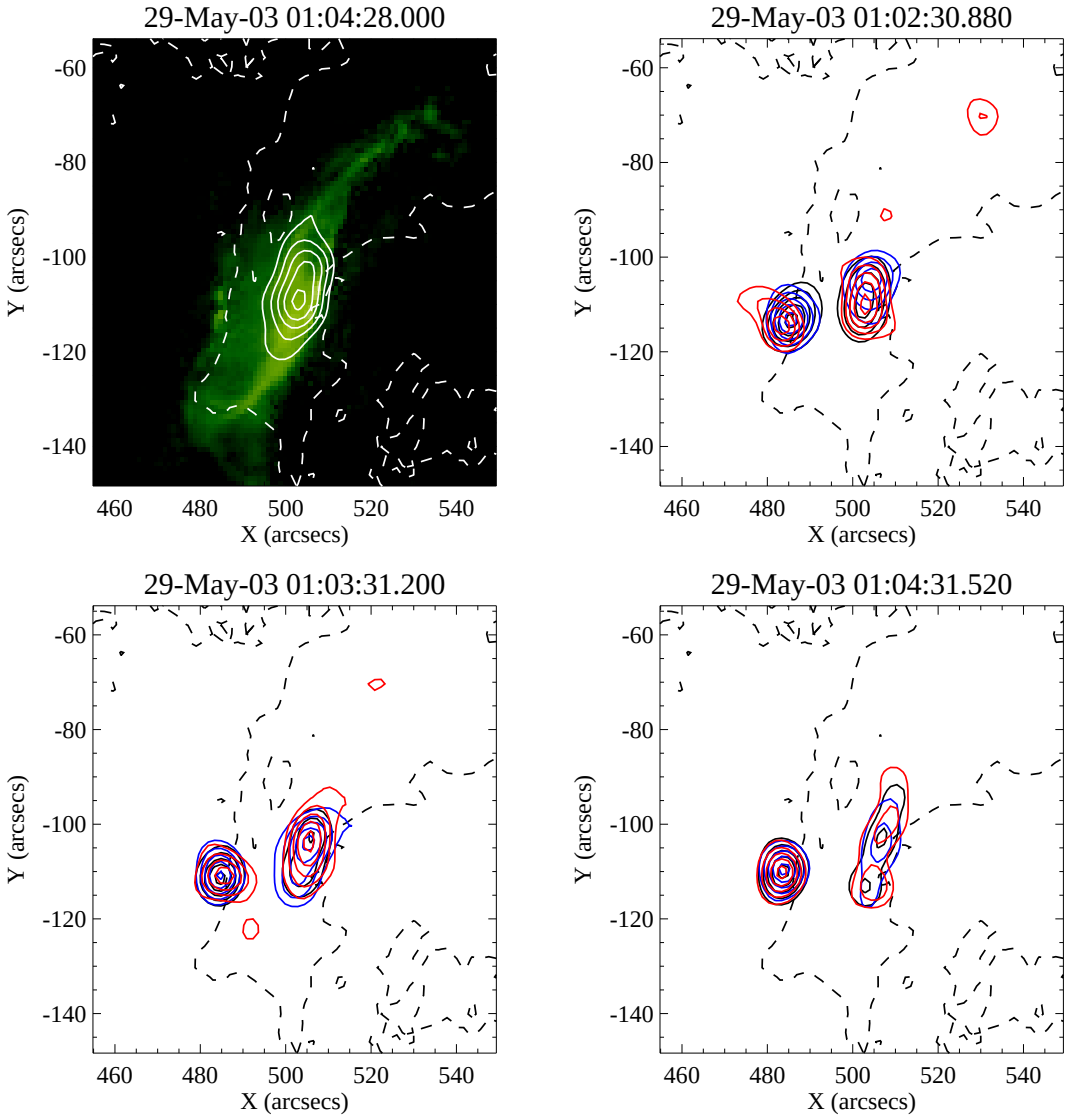

Figure 3.2: Spatial distribution of HXRs during the main impulsive phase. The top left map is the *RHESSI* 12-25 keV image (white solid contours) during 01:04:20 - 01:04:36 UT overlaid on the *TRACE* 195 Å image taken at 01:04:28 UT. The top right map is the *RHESSI* images in three energy bands, 50-70 (black solid contours), 70-100 (blue), and 100-200 keV (red) during 01:02:00 - 01:03:00 UT. The bottom left and right maps are same as the top right map, but during 01:03:00 - 01:04:00 UT and 01:04:00 - 01:05:00 UT, respectively. The *RHESSI* images are reconstructed with the CLEAN algorithm. Contour levels are 35%, 50%, 65%, 80%, and 95% of the peak intensity in each image. The dashed contours denote the photospheric magnetic neutral lines. Solar north is up and west is to the right.

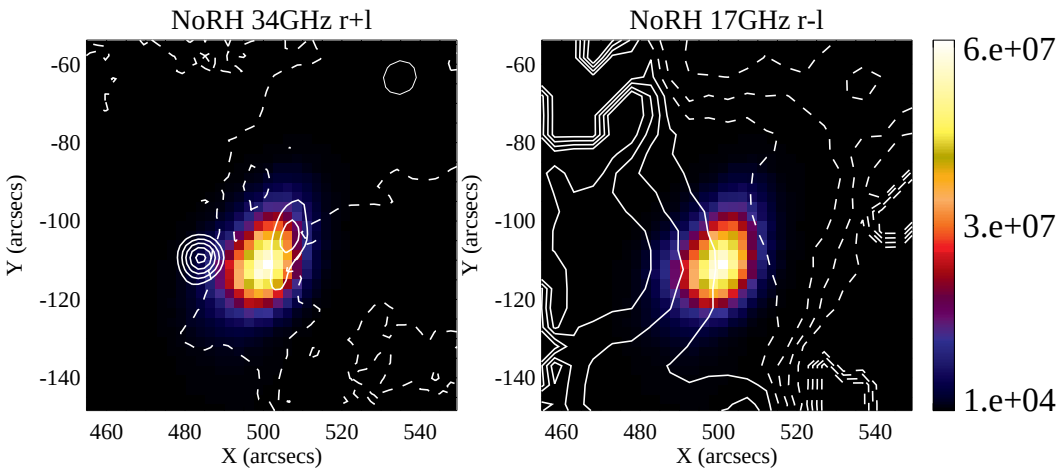

Figure 3.3: Spatial distribution of microwaves and the degree of polarization at 01:04:39 UT. The color images are the NoRH 34 GHz brightness temperature (in units of kelvin) map. Solar north is up and west is to the right. *Left*: The solid contours are the *RHESSI* 70-100 keV image, same as the blue contours in the bottom right map of Fig. 3.2. The dashed contours denote the photospheric magnetic neutral lines. A white circle in the upper right corner denotes the beam size at half-level of the peak intensity. *Right*: The thick and dashed contours are degree of right- and left-circular polarization at 17 GHz, respectively. Contour levels are 10%, 30%, 50%, and 70%.

microwave source is located between the footpoint HXR sources. It is close to the coronal HXR (12-25 keV) source, implying that this microwave source is located at the loop top. The right map shows that the microwave at the eastern region with positive magnetic polarity is right circularly polarized and vise verse. This is consistent with x-mode emission, supporting that this microwave emission is the gyrosynchrotron radiation. We further confirm from the spectral analysis (§ 3.2.3) that the microwave emissions above 17 GHz are optically thin non-thermal gyrosynchrotron radiation. The microwave is the brightest at the region with weaker degree of polarization. Both the polarization information and the configuration of the longitudinal magnetic field indicate that the magnetic field at the microwave source is quasi-perpendicular to the line of sight (Fleishman & Melnikov, 2003). Therefore we consider that this microwave source corresponds to the loop top. Such a spatial distribution of the HXR and microwave emissions can be explained by the TPP model, if the microwaves are

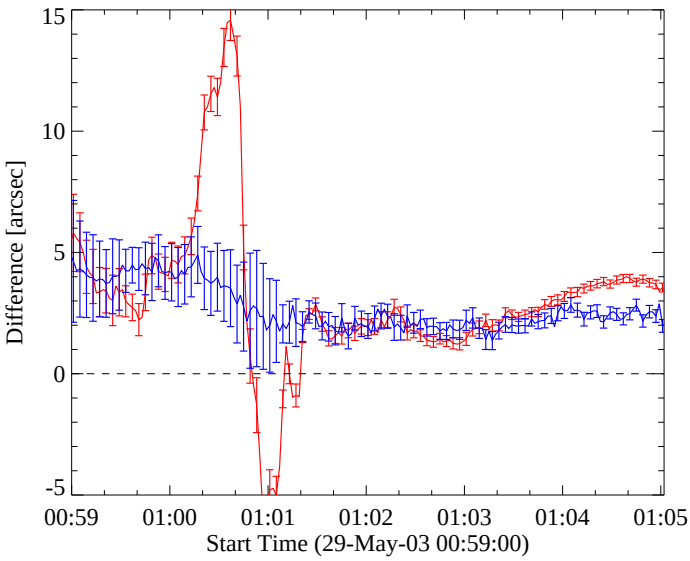

Figure 3.4: Time profiles of the difference of the microwave source size between 17 GHz and 34 GHz. The red line denotes the difference of the microwave source width in M-direction, $(w^{\rm a}_{MM})_{17\ {\rm GHz}} - (w^{\rm a}_{MM})_{34\ {\rm GHz}}$, and the blue line is that in m-direction, respectively.

emitted by ~ 1 MeV electrons trapped in the loop top and the HXRs are emitted by ~ 100 keV electrons precipitating into the footpoints.

Figure 3.4 shows the difference of the microwave source size between 17 GHz and 34 GHz, which is estimated in § 2.3.2. The red and blue lines show the time profiles of the difference of the source width, $w^{\rm a}_{17\ {\rm GHz}} - w^{\rm a}_{34\ {\rm GHz}}$, in M- and m-directions, respectively. The 17 GHz microwave source size is always larger than the 34 GHz in both M- and m-directions, except the period during 01:00:40 - 01:01:20 UT. This indicates that higher energy electrons are more efficiently trapped at a narrower region of the loop top, because higher frequency gyrosynchrotron radiation is emitted by more energetic electrons.

3.2.3 Spectra

We analyze the temporally resolved (but spatially unresolved) spectra during the main impulsive phase. We fit the *RHESSI* 40-250 keV spectrum at each time interval

with a double power-law function of the form,

$$f(\epsilon, t) = \begin{cases} I_{\rm L}(t)\epsilon^{-\gamma_{\rm L}(t)}, & \text{if } \epsilon \leq \epsilon_{\rm b}(t), \\ I_{\rm H}(t)\epsilon^{-\gamma_{\rm H}(t)}, & \text{if } \epsilon > \epsilon_{\rm b}(t), \end{cases} \tag{3.2.1}$$

where ϵ is the photon energy, $\gamma_{\rm L}(t)$ and $\gamma_{\rm H}(t)$ are the spectral indices of the lower and higher energy parts, $\epsilon_{\rm b}(t)$ is the break energy, and $I_{\rm H}(t) = I_{\rm L}(t)\epsilon_{\rm b}(t)^{\gamma_{\rm H}(t)-\gamma_{\rm L}(t)}$, respectively. The upper panel of Figure 3.5 shows an example *RHESSI* energy spectrum and its fitting result. We chose energy bins of 2 keV from 40 to 60 keV, 2.5 keV from 60 to 100 keV, 5 keV from 100 to 150 keV, and 12.5 keV beyond 150 keV, and a time resolution of 4 s (approximately equal to the *RHESSI* rotation period). We used the front segments of detectors 3, 4, and 8, which have the best energy resolution below $\sim$ 100 keV (Smith et al., 2002). For convenience of analysis, the range of $\epsilon_{\rm b}(t)$ was limited to 70 to 130 keV.

We also obtained the temporally resolved microwave spectral index from the NoRP data. After integrating it by 2 s to improve the statistics, we fit the NoRP spectrum taken with five frequencies of 2, 3.75, 9.4, 17, and 35 GHz at each time interval with a generic function (Silva et al., 2000),

$$\begin{aligned} g(\nu, t) &= a_1(t)\nu^{a_2(t)}\left[1 - \exp(-a_3(t)\nu^{-a_4(t)})\right] \\ &\simeq \begin{cases} a_1(t)\nu^{a_2(t)}, & \text{if } \nu \ll \nu_{\rm turnover}(t), \\ a_1(t)a_3(t)\nu^{-[a_4(t)-a_2(t)]}, & \text{if } \nu \gg \nu_{\rm turnover}(t), \end{cases} \end{aligned} \tag{3.2.2}$$

where ν is the frequency. We obtained the best-fit spectral index of the microwave flux density in the optically thin (higher frequency) regime, $\alpha(t) = a_4(t) - a_2(t)$ (positive value), as well as the turnover frequency $\nu_{\rm turnover}(t)$. The lower panel of Figure 3.5 shows an example NoRP microwave spectrum and its fitting result. We confirm that $\nu_{\rm turnover}(t)$ is less than 17 GHz during the main impulsive phase. Therefore the microwave emissions above 17 GHz are certainly optically thin, non-thermal gyrosynchrotron radiation.

Figure 3.6 (top) shows the time profiles of the spectral indices of the non-thermal emissions. The blue and red asterisks are the spectral indices of the lower energy ($\lesssim$ 100 keV) and higher energy ($\gtrsim$ 100 keV) HXRs (hereafter $\gamma_{\rm L}^{\rm obs}(t)$ and $\gamma_{\rm H}^{\rm obs}(t)$), and the green diamonds are the spectral indices of the microwaves in the optically thin regime (hereafter $\alpha^{\rm obs}(t)$), respectively.

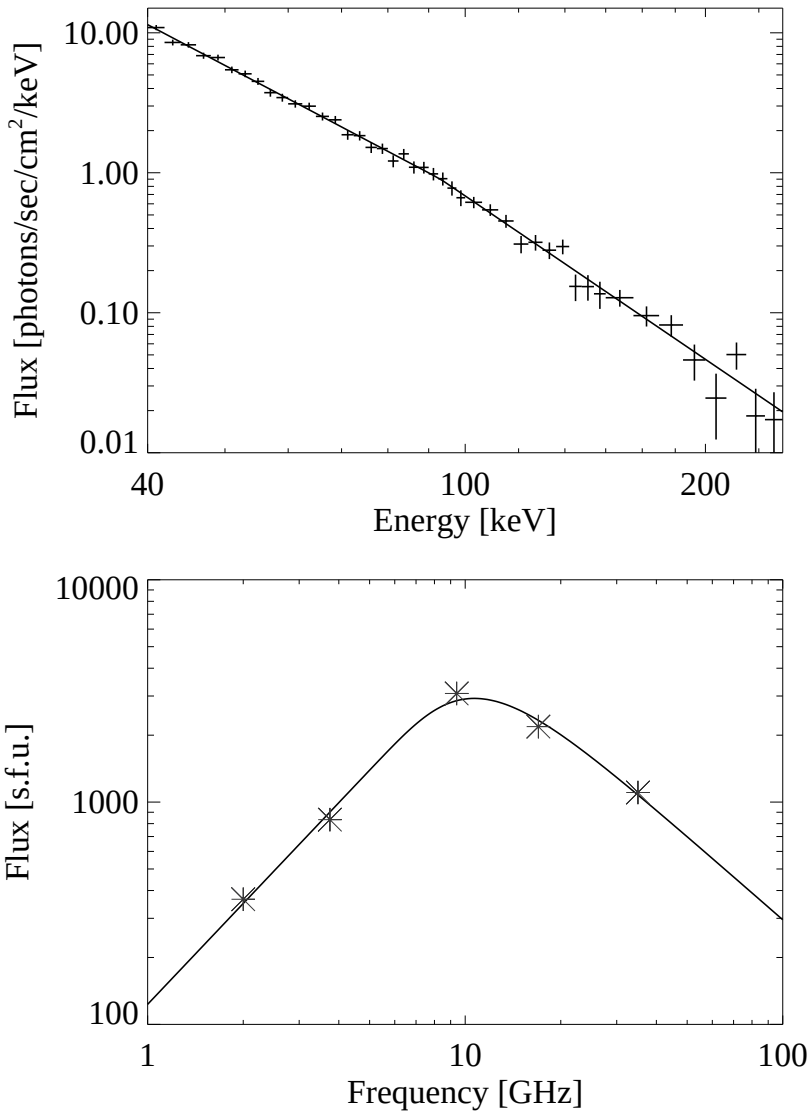

Figure 3.5: HXR and microwave spectra taken with *RHESSI* and NoRP. The upper plot shows the HXR photon spectrum (points with error bars) and the fitted double power-law function (solid line) at 01:04:28 - 01:04:32 UT. Values of $\gamma_{\rm L}$, $\gamma_{\rm H}$, and $\epsilon_{\rm b}$ (keV) are determined to be $\{3.01 \pm 0.001, 3.88 \pm 0.003, 93.0 \pm 0.1\}$. The lower plot shows the microwave spectrum at five frequencies of 2, 3.75, 9.4, 17, and 35 GHz (asterisks) and the fitted model described by equation (3.2.2) (solid line) at 01:04:29 UT. Values of α and $\nu_{\rm turnover}$ (GHz) are determined to be $\{1.25, 11.1\}$.

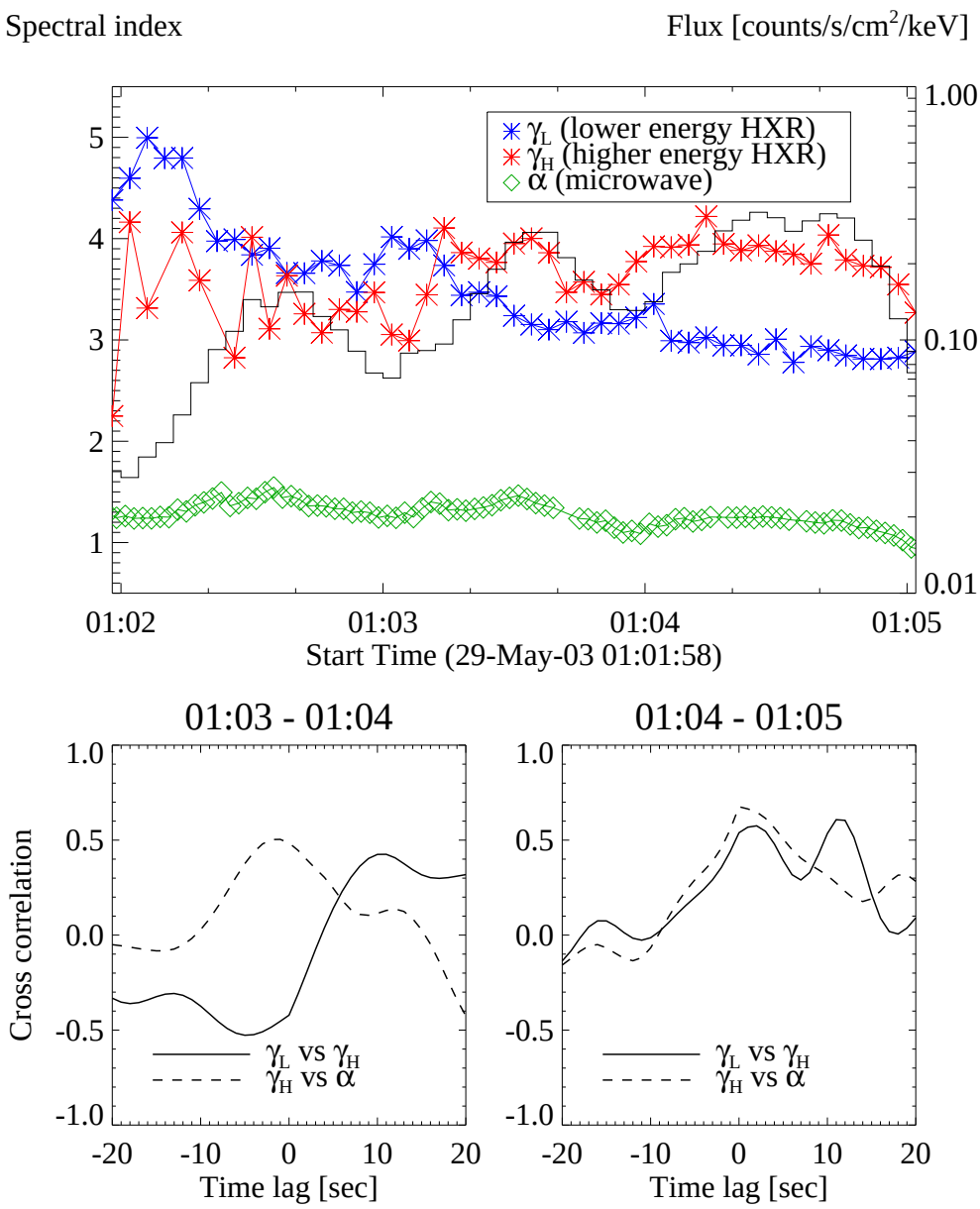

Figure 3.6: *Top*: Time profiles of the spectral indices of the non-thermal emissions during the main impulsive phase. The blue, red, and green symbols are $\gamma_{\rm L}^{\rm obs}(t)$, $\gamma_{\rm H}^{\rm obs}(t)$, and $\alpha^{\rm obs}(t)$, respectively. The break energy is $\sim$ 100 keV. The solid line denotes the *RHESSI* count flux at 50-100 keV. Note that some data which have large uncertainty are omitted in the plot. *Bottom*: Cross-correlation functions of two time profiles of the spectral indices as a function of time lag, during 01:03 - 01:04 UT (*left*) and 01:04 - 01:05 UT (*right*). The solid lines are cross-correlation of $\gamma_{\rm L}^{\rm obs}(t)$ and $\gamma_{\rm H}^{\rm obs}(t)$, and the dashed lines are that of $\gamma_{\rm H}^{\rm obs}(t)$ and $\alpha^{\rm obs}(t)$, respectively.

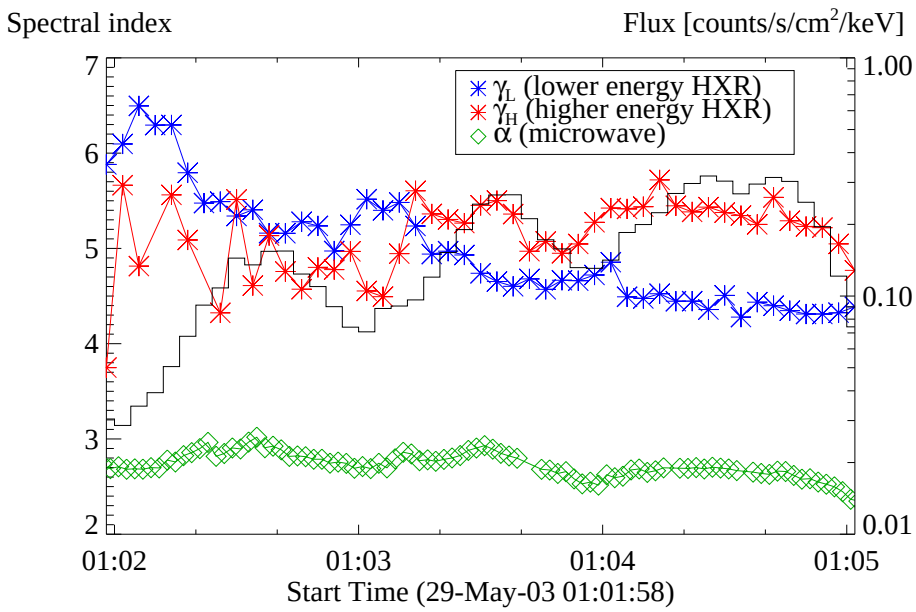

Figure 3.7: Time profiles of the spectral indices of the non-thermal electrons inferred from the spectra of emissions (Fig. 3.6). The blue, red, and green symbols correspond to the parent electron spectral indices of the lower energy HXRs, higher energy HXRs, and microwaves, respectively.

The time profile of $\gamma_{\rm L}^{\rm obs}(t)$ shows the so-called soft-hard-soft (SHS) behavior for each spike except the last. For example, $\gamma_{\rm L}^{\rm obs}(t)$ is $\sim$ 4.8 at 01:02:10 UT, becomes hard ($\sim$ 3.7) at 01:02:40 UT, and softens again ($\sim$ 4.0) at 01:03:10 UT. This is interpreted that the efficiency of electron acceleration is higher when the HXR flux is larger (Grigis & Benz, 2006). However, the time profile of $\gamma_{\rm H}^{\rm obs}(t)$ behaves differently from that of $\gamma_{\rm L}^{\rm obs}(t)$. It does not show the SHS behavior. The values of the microwave spectral index are quite smaller than those of the HXR spectral indices. Figure 3.7 shows the time profiles of the spectral indices of the parent electrons inferred from the spectral indices of emissions, by assuming the emission mechanism of the HXR (thick-target bremsstrahlung, e.g., Tandberg-Hanssen & Emslie, 1988) and microwave (gyrosynchrotron, Dulk, 1985). This implies that the inferred energy distribution of the microwave-emitting electrons is harder than that of the HXR-emitting ones. We will discuss in § 3.4 whether the energy distribution of the microwave-emitting electrons is actually harder than that of the HXR-emitting ones, based on the modeling study of the electron transport.

In addition to this, we find from Figure 3.6 that the time profile of $\gamma_{\rm H}^{\rm obs}(t)$ is similar to that of $\alpha^{\rm obs}(t)$, though the absolute values of their spectral indices differ. We also find that the time profile of $\gamma_{\rm H}^{\rm obs}(t)$ (and $\alpha^{\rm obs}(t)$) is delayed from that of $\gamma_{\rm L}^{\rm obs}(t)$. This tendency is especially seen during 01:03 - 01:05 UT. The cross-correlation functions of the spline-interpolated time profiles of the spectral indices are shown in the bottom panels of Figure 3.6. We find: (1) the time profile of $\alpha^{\rm obs}(t)$ and that of $\gamma_{\rm H}^{\rm obs}(t)$ show a peak correlation without a time delay (within a time resolution of 4 s); and (2) the time profile of $\gamma_{\rm H}^{\rm obs}(t)$ is delayed by about 10 s from that of $\gamma_{\rm L}^{\rm obs}(t)$. The similarity of the time profiles between $\gamma_{\rm H}^{\rm obs}(t)$ and $\alpha^{\rm obs}(t)$ indicates that the higher energy HXR-emitting electrons and the microwave-emitting electrons are from the same population and in a close energy range. The delay of the time profile of $\gamma_{\rm H}^{\rm obs}(t)$ from that of $\gamma_{\rm L}^{\rm obs}(t)$ may be interpreted as an electron energy-dependent time delay (e.g., Aschwanden et al., 1997).

From the comparative analysis of the HXR and microwave emissions, we found a new insight of electrons which emit the higher energy ($\gtrsim$ 100 keV) HXRs. They are thought to have an intermediate energy (several hundreds keV) between the lower energy HXR-emitting electrons ($\lesssim$ 200 keV) and the microwave-emitting ones ($\sim$ 1 MeV). They emit HXRs at the footpoints of the loop, in the same manner as the lower energy HXRs. On the other hand, the time profile of their spectrum is similar to the microwave-emitting electrons rather than the lower energy HXR-emitting ones. We consider that this energy-dependent difference of the electron distribution is yielded as a consequence of an energy-dependent transport effect of the electrons.

3.3 A Model for Electron Transport

To explain the observational characteristics, we study the electron transport by using the Fokker-Planck modeling of TPP. The TPP model has been implemented in various ways, analytic (Melrose & Brown, 1976; MacKinnon et al., 1983; MacKinnon, 1986, 1988, 1991; Leach & Petrosian, 1981; Lu & Petrosian, 1988) and numerical approaches (McClements, 1990a,b; Hamilton et al., 1990; MacKinnon & Craig, 1991; Fletcher & Martens, 1998; Lee & Gary, 2000) to treat electron transport in the flare loop. We study the gyro-averaged Fokker-Planck equation that allows us to explicitly

treat electron pitch-angle diffusion in a magnetic loop and describe the electron phase space distribution along the loop.

3.3.1 Basic Equations

We treat the gyro-averaged Fokker-Planck equation (Hamilton et al., 1990; Lu & Petrosian, 1990; Fletcher & Martens, 1998),

$$\frac{\partial N}{\partial t} + \mu c\beta \frac{\partial N}{\partial r} + \frac{\partial}{\partial \mu}(\dot{\mu} N) + \frac{\partial}{\partial E}\left(\dot{E} N\right) = \frac{\partial}{\partial \mu}\left(D_{\mu\mu}\frac{\partial N}{\partial \mu}\right) + Q(r, \mu, E, t). \tag{3.3.1}$$

Here $N(r, \mu, E, t)$ is the electron distribution in phase space along the loop (number of electrons per unit length per unit pitch-angle cosine per unit energy), $Q(r, \mu, E, t)$ is the electron flux (number of electrons per unit length per unit energy per unit pitch-angle cosine per unit time) injected into the loop, $\dot{E}$ and $D_{\mu\mu}$ are the Coulomb energy loss rate and pitch-angle diffusion coefficient, $\dot{\mu}$ is the magnetic mirroring force, r is the spatial coordinates along the magnetic field line (Fig. 3.8; $r = 0$ at the loop top and $r = r_{\rm f}$ at the footpoint), μ is the pitch-angle cosine, $E = \Gamma - 1$ is the kinetic energy in units of the electron rest mass energy $m_{\rm e}c^2$, Γ is the Lorentz factor, $\beta = \sqrt{1 - \Gamma^{-2}}$, $m_{\rm e}$ is the electron mass, and c is the speed of light, respectively.

We adopt the Coulomb energy loss rate and pitch-angle diffusion coefficient for a fully ionized plasma given by Leach & Petrosian (1981),

$$\dot{E} = -Kn/\beta \equiv -\nu_{\rm E} E, \quad (K = 4\pi c r_0^2 \ln\Lambda), \tag{3.3.2}$$

$$D_{\mu\mu} = \frac{Kn}{\beta^3\Gamma^2}(1 - \mu^2) = \frac{\nu_{\rm E}}{(E + 2)}(1 - \mu^2), \tag{3.3.3}$$

where $r_0 = 2.82 \times 10^{-13}$ cm is the classical electron radius, n is the ambient plasma number density, $\ln\Lambda \simeq 25$ is the Coulomb logarithm for the typical solar coronal condition, and $\nu_{\rm E} \equiv Kn/(\beta E)$ is the Coulomb collision frequency, respectively. The ambient plasma number density and the Coulomb logarithm are treated as constant. We neglect other Coulomb diffusion coefficients such as D_{EE} and $D_{\mu E}$ which are smaller than $D_{\mu\mu}$ by a factor of order $\ln\Lambda$ (Hamilton et al., 1990). Here any other physics of electron kinematics such as wave-particle interactions are ignored for simplicity. We later discuss the validity of this simplification.

The magnetic mirroring force,

$$\dot{\mu} = -\frac{1}{2}c\beta(1-\mu^2)\frac{d\ln B(r)}{dr}, \tag{3.3.4}$$

depends on the gradient of the magnetic field strength $B(r)$ along the field line. However, the actual magnetic field configuration in solar flares is unknown. In this model, we employ the potential magnetic field configuration for simplicity. We give the two-dimensional, static, and symmetric potential magnetic field in Cartesians coordinate as follows (Priest, 1987):

$$\begin{cases} B_x = B_{\rm f}\cos(kx)e^{-kz}, \\ B_z = -B_{\rm f}\sin(kx)e^{-kz}, \end{cases} \tag{3.3.5}$$

where x and z directions correspond to the tangential and normal directions relative to the solar surface, and $B_{\rm f}$ is the magnetic field strength at the footpoint, respectively. The parameter of k specifies the magnetic field line, determined below. This magnetic field configuration is shown in Figure 3.8. The strength of this potential magnetic field measured along the field line is written as

$$B(r) = \frac{B_0}{\cos\left[\sin^{-1}\left\{\tanh(kr)\right\}\right]}, \tag{3.3.6}$$

where B_0 is the magnetic field strength at the loop top,

$$k = \frac{1}{2r_{\rm f}}\ln\left[\frac{1+\sin\left\{\cos^{-1}\left(M^{-1}\right)\right\}}{1-\sin\left\{\cos^{-1}\left(M^{-1}\right)\right\}}\right], \tag{3.3.7}$$

and $M = B_{\rm f}/B_0$ is the magnetic mirror ratio, respectively.

We take the parameters as follows: $r_{\rm f} = 1.5\times10^9$ cm, $n = 3\times10^{10}$ cm^{-3}, and $M = 2$. We calculate the footpoint distance (a half loop length) $r_{\rm f}$ from the distance of the HXR sources (Fig. 3.2), assuming a semi-circular shape for the loop. The number density n in our model is slightly smaller than the observed value of $(6-8)\times10^{10}$ cm^{-3} derived from the *GOES* observation during 01:03 - 01:05 UT (assuming a volume of $(2r_{\rm f})^3$ and a filling factor of unity). We assume that electrons are trapped in an outer loop with a lower density than the brightest SXR loop. In the outer loop, energy dissipation (electron bombardment) at the footpoints and the resultant filling with evaporated chromospheric plasma have not yet occurred, while they have already occurred in the inner SXR loop. We adopt the magnetic mirror

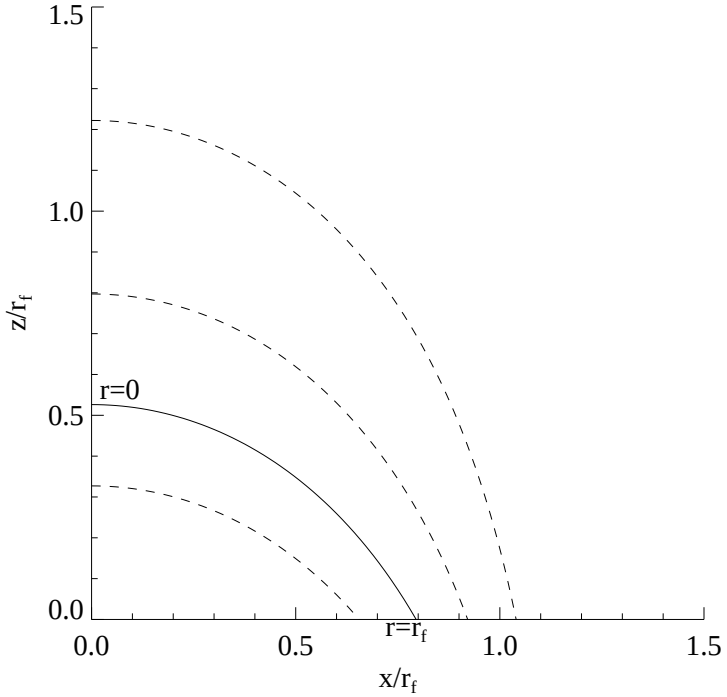

Figure 3.8: The potential magnetic field configuration described by equation (3.3.5). The x- and z-axes correspond to the tangential and normal directions relative to the solar surface, respectively. We solve the Fokker-Planck equation (eq. (3.3.1)) along the thick line which has the half loop length $r_{\rm f} = 1.5 \times 10^4$ km and the magnetic mirror ratio $M = 2$.

ratio based on the statistical analysis of flare data taken with *CGRO* and *Yohkoh* by Aschwanden et al. (1998, 1999). They estimated the fraction of directly precipitating electrons to trap-precipitating ones and derived a magnetic mirror ratio of $1.2 - 3$.

3.3.2 Numerical Code

We numerically solve equation (3.3.1) by using a finite difference method with operator splitting. The differential operators in equation (3.3.1) are split into four terms: the advection terms in r, μ and E space, and the diffusion term. We solve the diffusion term by using the Crank-Nicholson method with central difference. We employ the symmetric boundary condition in μ space to ensure total number con-

servation. For the advection term in E space we use an analytic solution derived by the method of characteristics (Craig et al., 1985; MacKinnon, 1986), and adopt a single power-law function for the necessary interpolation at the intermediate location between the grid points (if either grid point has a non-positive value, we instead apply a linear interpolation). For the advection terms in r and μ space, we adopt the CIP-CSL2 scheme developed by Yabe et al. (2001). This scheme simultaneously solves the integrated value of N as well as N itself to keep the "subgrid" information and to satisfy the mass conservation. The boundary condition at $r = 0$,

$$\left[\frac{\partial}{\partial r}\left\{N(r,\mu,E,t) - N(r,-\mu,E,t)\right\}\right]_{r=0} = 0, \tag{3.3.8}$$

is required for the symmetric solution of equation (3.3.1). Another boundary condition at $r = r_{\rm f}$ is as follows: (1) electrons with positive pitch angle, $N(r_{\rm f}, \mu \geq 0, E, t)$, are lost from the calculation box; and (2) there is no flow from outside the box, $N(r_{\rm f}, \mu < 0, E, t) = 0$. Physically, the former corresponds to the electron precipitation into the footpoint, and the latter means that the possibility of electrons originating below the footpoint (chromosphere) is excluded. We set 50×100 cells in (r, μ) space, and 100 logarithmically-spaced grids from 50 to 5000 keV in E space, respectively.

Treatment for Trap-plus-Precipitation

The concept of the TPP model developed by Melrose & Brown (1976) is to simultaneously describe the evolution of electrons at the trap region such as a magnetic loop (trapped electrons) and those escaping from there (precipitating electrons), by relating them with the implicit precipitation rate. We advance their treatment by using the general form of the spatially-inhomogeneous Fokker-Planck equation. This equation describes the time evolution of electrons $N(r, \mu, E, t)$ along the loop. We treat them as the trapped electrons in the loop. A part of them, which are inside the loss cone, can reach the footpoint and then escape from the loop. This is taken into consideration by the boundary condition at $r = r_{\rm f}$. By this condition, we can explicitly calculate the precipitating electron flux into the footpoint of the loop. This is defined as

$$F(\mu, E, t) = \mu c \beta N(r_{\rm f}, \mu, E, t), \quad \text{for } \mu > 0. \tag{3.3.9}$$

3.3.3 Time-Dependent Injection Flux

We give the time-dependent, single power-law electron injection flux $Q(r, \mu, E, t)$,

$$Q(r, \mu, E, t) = A(t)R(r)\phi(\mu)\left(\frac{E}{E_{\rm p}}\right)^{-\delta_{\rm in}(t)}, \tag{3.3.10}$$

where we adopt $E_{\rm p} = 0.098$ (= 50 keV), and

$$R(r) = \exp\left[-\left(\frac{r}{0.2r_{\rm f}}\right)^2\right], \tag{3.3.11}$$

$$A(t) = \exp\left[-\left(\frac{t-30}{20}\right)^2\right], \tag{3.3.12}$$

$$\delta_{\rm in}(t) = 4.5 + \cos^2\left(\frac{\pi t}{60}\right), \tag{3.3.13}$$

for $0 \leq t \leq 60$ s. Equation (3.3.11) gives the electron injection at the loop top. The FWHM of this injection site, $0.33r_{\rm f} \simeq 5000$ km, is roughly equal to the size of the above-the-loop-top HXR source (e.g., Masuda et al., 1994, 1995). Equations (3.3.12) and (3.3.13) describe a single peak electron injection with a SHS spectrum: the spectrum hardens when the flux increases ($0 < t < 30$ s), becomes hardest at the peak ($t = 30$ s), and then softens when the flux decreases ($30 < t < 60$ s). We adopt this form for the electron injection because the HXR spectrum in the lower energy regime observed in the 2003 May 29 flare shows the SHS behavior (Fig. 3.6).

The remaining term of $\phi(\mu)$ gives the (time- and energy-independent) pitch-angle distribution of the injection flux. We perform calculations for three cases of the pitch-angle distribution,

$$\phi(\mu) = \begin{cases} 0.5, & \text{(isotropic)}, \\ 1.134 \times \exp[-(\mu/0.5)^2], & \text{(pancake)}, \\ 1.881 \times \exp[-\{(|\mu|-1)/0.3\}^2], & \text{(beamlike)}. \end{cases} \tag{3.3.14}$$

The injection flux is given to be symmetric in (r, μ) space. The initial condition is $N(r, \mu, E, t = 0) = 0$. Then the solution of equation (3.3.1) is symmetric: $N(r, \mu, E, t) = N(-r, -\mu, E, t)$. We discuss how the difference of the injection pitch-angle distribution affects the evolution of the precipitating electrons $F(\mu, E, t)$ as well as the trapped electrons $N(r, \mu, E, t)$. Then we discuss which case well explains the observations, for the determination of the injection pitch-angle distribution.

3.4 Calculation Results and Interpretation

In this section, we present our calculation results of the Fokker-Planck equation. Figures 3.10, 3.11, and 3.12 show the electron distribution in phase space (r, μ), calculated for the isotropic, pancake, and beamlike cases, respectively. In the isotropic and pancake cases (Figs. 3.10 and 3.11), most electrons are trapped (inside the white solid line), forming the loss cone distribution. A part of them enter the loss cone (outside the white solid line) and then reach the footpoint ($r = r_{\rm f}$ with $\mu > 0$). This is more clearly seen for the lower energy (left panels) and in the isotropic case (Fig. 3.10). The electron distribution in the beamlike case (Fig. 3.12) is completely different from that in the isotropic and pancake cases. For lower energy (left panels), most electrons are in the loss cone. They correspond to directly precipitating electrons (Aschwanden, 1998; Aschwanden et al., 1998, 1999), which are injected with small pitch angle and directly precipitate into the footpoint. For higher energy, directly precipitating electrons are not clearly seen and the trapped electrons become dominant with time.

In § 3.4.1, we discuss the time evolution of the trapped electron distribution and the precipitating electron flux. Our calculations confirm the electron trap and precipitation regardless of the weak and strong diffusion limits. In § 3.4.2, we discuss the time evolution of the non-thermal emissions predicted by the electron model for comparison with the observations.

3.4.1 Evolution of Electrons

To illustrate the time evolution of the trapped and precipitating electrons, we introduce the pitch-angle integrated variables:

$$N_\mu(r, E, t) = \int_{-1}^{1} N(r, \mu, E, t) d\mu, \tag{3.4.1}$$

$$F_\mu(E, t) = \int_{-1}^{1} F(\mu, E, t) d\mu = c\beta \int_{0}^{1} \mu N(r_{\rm f}, \mu, E, t) d\mu. \tag{3.4.2}$$

Figures 3.13, 3.14, and 3.15 show the temporal variations of the trapped electrons $N_\mu(r, E, t)$ and the precipitating electron flux $F_\mu(E, t)$, calculated for the isotropic, pancake, and beamlike cases, respectively.

The color images of these Figures show the temporal variation of the trapped

electrons along the loop. The vertical axis corresponds to the spatial coordinates from the loop top to the footpoint. The spatial distributions in the isotropic (Fig. 3.13) and pancake (Fig. 3.14) cases look similar. The electrons are confined to the loop-top region. These electrons are expected to emit the microwave primarily at the loop top, as observed in the 2003 May 29 flare. The higher energy electrons (bottom) are confined to the narrower region than the lower energy ones (top). They are expected to emit the microwave which size is smaller when the frequency is higher, as also observed (Fig. 3.4). In § 3.4.2, we confirm that these electron distributions certainly emit the microwave that explains the observation of the 2003 May 29 flare. The spatial distribution in the beamlike case (Fig. 3.15) is different from that in the isotropic and pancake cases. The electrons are broadly distributed along the loop. This is because the electrons in the beamlike case have a smaller pitch-angle than those in other cases, and thus can move broadly in the loop. The higher energy electrons (bottom) are situated not at the loop top but at the intermediate position ($r \simeq 0.5$) at the peak time. In all three cases, the higher energy electrons peak later compared to the lower energy ones (top) by about ~ 5 s and remain for a longer time after the peak.

The right plots of these Figures show the time profiles of the precipitating electron flux (top for 100 keV and bottom for 1 MeV). The 100 keV electrons peak at 30 s, showing similar profile in three cases. The profile of the 1 MeV electrons is different in three cases. In the beamlike case (Fig. 3.15), they peak at 30 s. In the isotropic and pancake cases (Figs. 3.13 and 3.14), they peak later. Considerable amount of precipitation after the peak is seen, particularly in the pancake case. As such, the distributions of the electrons are quite different with their energy and the injection pitch-angle distribution.

Energy Distribution

We discuss the evolution of the energy distribution of the electrons. To illustrate the energy distribution of the trapped electrons, we integrate them over space,

$$N_{r,\mu}(E,t) = \int_0^{r_{\rm f}} N_\mu(r,E,t)dr. \tag{3.4.3}$$

Next we illustrate the time evolution of the energy distribution of the electrons by calculating the slope s in energy from the following equation,

$$s_i = -\frac{\log\left[X(E_{i+1},t)/X(E_i,t)\right]}{\log\left(E_{i+1}/E_i\right)}, \tag{3.4.4}$$

where $X = N_{r,\mu}$ or F_μ, and subscript i denotes the grid position in energy space. The calculation results in three cases are presented in Figure 3.16.

Figure 3.16 shows that the precipitating electrons (right) have a softer energy distribution than the trapped ones (left), except those below 100 keV in the beamlike case (bottom). To understand this in terms of a diffusion regime, we introduce the precipitation rate,

$$\begin{aligned} \nu_{\rm p} &= \frac{F_\mu}{N_{r,\mu}} \quad [{\rm sec}^{-1}] \\ &\propto E^{\delta}. \end{aligned} \tag{3.4.5}$$

In the strong and weak diffusion limits (Kennel & Petscheck, 1966), the precipitation rates are respectively evaluated as (using non-relativistic expressions),

$$\nu_{\rm p} \propto \begin{cases} 1/\tau_{\rm e} \propto v \propto E^{0.5}, & \text{(strong)}, \\ 1/\tau_{\rm d} \sim D_{\mu\mu} \propto E^{-1.5}, & \text{(weak)}, \end{cases} \tag{3.4.6}$$

where $\tau_{\rm e}$ is the electron loop-transit time, approximated by $2r_{\rm f}/(\mu c\beta)$. This yields $-1.5 \leq \delta \leq 0.5$. Whether diffusion for an electron is weak or strong depends on its energy E. This means that δ itself is a function of E. When $\tau_{\rm d} > \tau_{\rm e}$, the diffusion is weak and δ takes a negative value and vice versa. Since $\tau_{\rm d}$ becomes much longer than $\tau_{\rm e}$ for higher energy electrons, δ approaches its lower limit (weak diffusion limit) of -1.5 with increasing E.

Figure 3.9 shows the precipitation rates in three cases. In the lower energy regime ($<$ 100 keV) in the beamlike case (squares), the precipitation rate does not considerably vary with energy, meaning $\delta \sim 0$. In the higher energy regime (100 - 1000 keV), on the other hand, the precipitation rates decrease with increasing energy, meaning $\delta < 0$. This is consistent with the previous statement, and thus confirms our general treatment of the TPP model in the weak diffusion regime. We fit the precipitation rates in the energy range 100 - 1000 keV with a single power-law function, to estimate δ in the higher energy regime, and then obtain to be -0.84 (isotropic), -1.19 (pancake), and -0.52 (beamlike), respectively.

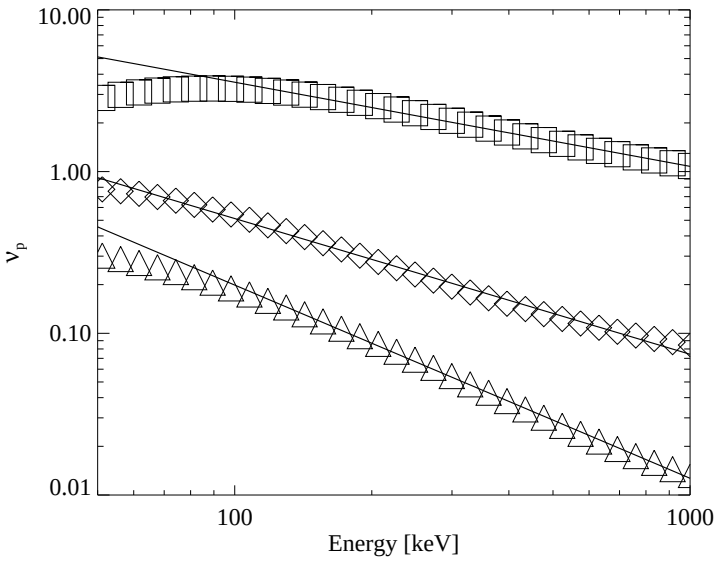

Figure 3.9: Precipitation rates (eq. (3.4.5)) at $t = 30$ s, calculated for the isotropic (diamonds), pancake (triangles), and beamlike (squares) cases, respectively. The solid lines are the fitting results in 100 - 1000 keV with a single power-law function. The slopes in the higher energy regime are ~ -0.84 (isotropic), -1.19 (pancake), and -0.52 (beamlike), respectively.

In the left panels of Figure 3.16, the slope of the trapped electrons below ~ 200 keV shows the SHS behavior, achieving its hardest values around $t = 30$ s. However, the slope above ~ 200 keV does not show the SHS behavior but hardens with time. The energy-dependent trap efficiency yields this difference of the temporal variation of the energy distribution between the lower and higher energies. The trapped electrons are lost via Coulomb energy loss and precipitation. The Coulomb energy loss rate $\nu_{\rm E}$ is smaller for the higher energy electrons. As seen in Figure 3.9, the weak diffusion yields a precipitation rate that is also smaller for the higher energy electrons. This means that the escape timescale from the phase space becomes longer for the higher energy electrons. For the lower energy electrons, the escape timescale is on the order of 1 s. This is much shorter than the injection timescale (eq. (3.3.12)). Therefore, the temporal variation of the energy distribution in the lower energy regime reflects that of the injection flux $\delta_{\rm in}(t)$ described by eq. (3.3.13). The escape timescale becomes comparable to or longer than the injection timescale for the higher energy electrons.

The higher energy electrons stay in the loop and their energy remains high for a longer time. As a result, the energy distribution in the higher energy regime hardens with time.

The right panels of Figure 3.16 show the slope of the precipitating electrons in energy. In the beamlike case (bottom), all of the electrons within 50 - 1000 keV show the SHS behavior. However, those in the isotropic and pancake cases (top and middle) do not necessarily behave SHS. The energy distributions of the electrons above ~ 200 keV harden with time, especially in the pancake case. We interpret these features in terms of the difference of the injection pitch-angle distribution.

The precipitating electrons consist of two different types: directly precipitating and trap-precipitating electrons (Aschwanden, 1998; Aschwanden et al., 1998, 1999). Electrons injected with small pitch angle directly precipitate into the footpoint without being trapped in the loop, while those injected with large pitch angle are trapped once and subsequently precipitate via pitch-angle scattering. When the injected electrons have a beamlike pitch-angle distribution, the majority of the precipitating electrons are the directly precipitating ones. When the injected electrons have a pancake pitch-angle distribution, on the other hand, almost all of the precipitating electrons are the trap-precipitating ones. The precipitating electrons in the isotropic case are in the intermediate state between them.

The directly precipitating electrons precipitate on a timescale of $\tau_{\rm e}$. The precipitation timescale of the trap-precipitating electrons, $\sim \tau_{\rm d}$, is longer than $\tau_{\rm e}$. The ratio of these two components, which is determined by the injection pitch-angle distribution, determines the precipitation timescale of the total precipitating electrons. The precipitation timescale is the shortest in the beamlike case, and the longest in the pancake case. This can be seen in Figure 3.9 that the precipitation rate is the largest in the beamlike case and the smallest in the pancake case. For the lower energy ($\lesssim 200$ keV) electrons, however, the precipitation timescale is shorter than the injection timescale in all three cases. Therefore, the temporal variation of the energy distribution in the lower energy regime reflects the instantaneous injection profile, the SHS behavior, regardless of the injection pitch-angle distribution. For the higher energy ($\gtrsim 200$ keV) electrons, the precipitation timescale becomes longer due to the weak diffusion, especially in the pancake case. When the precipitation

timescale is comparable to or longer than the injection timescale, the precipitating electrons include the trap-precipitating electrons injected previously as well as the currently injected electrons. This yields hardening of the energy distribution with time.

The difference of the slope δ in the precipitation rate (eq. (3.4.5)) in three cases can be explained by the above statement. The directly precipitating electrons take the precipitation rate of $E^{0.5}$ while the trap-precipitating ones take $E^{-1.5}$. When the number of the directly precipitating ones is larger than that of the trap-precipitating ones (corresponds to the beamlike case), δ would be close to zero or be positive. When the number of the trap-precipitating ones is larger than that of the directly precipitating ones (corresponds to the pancake case), δ approaches -1.5.

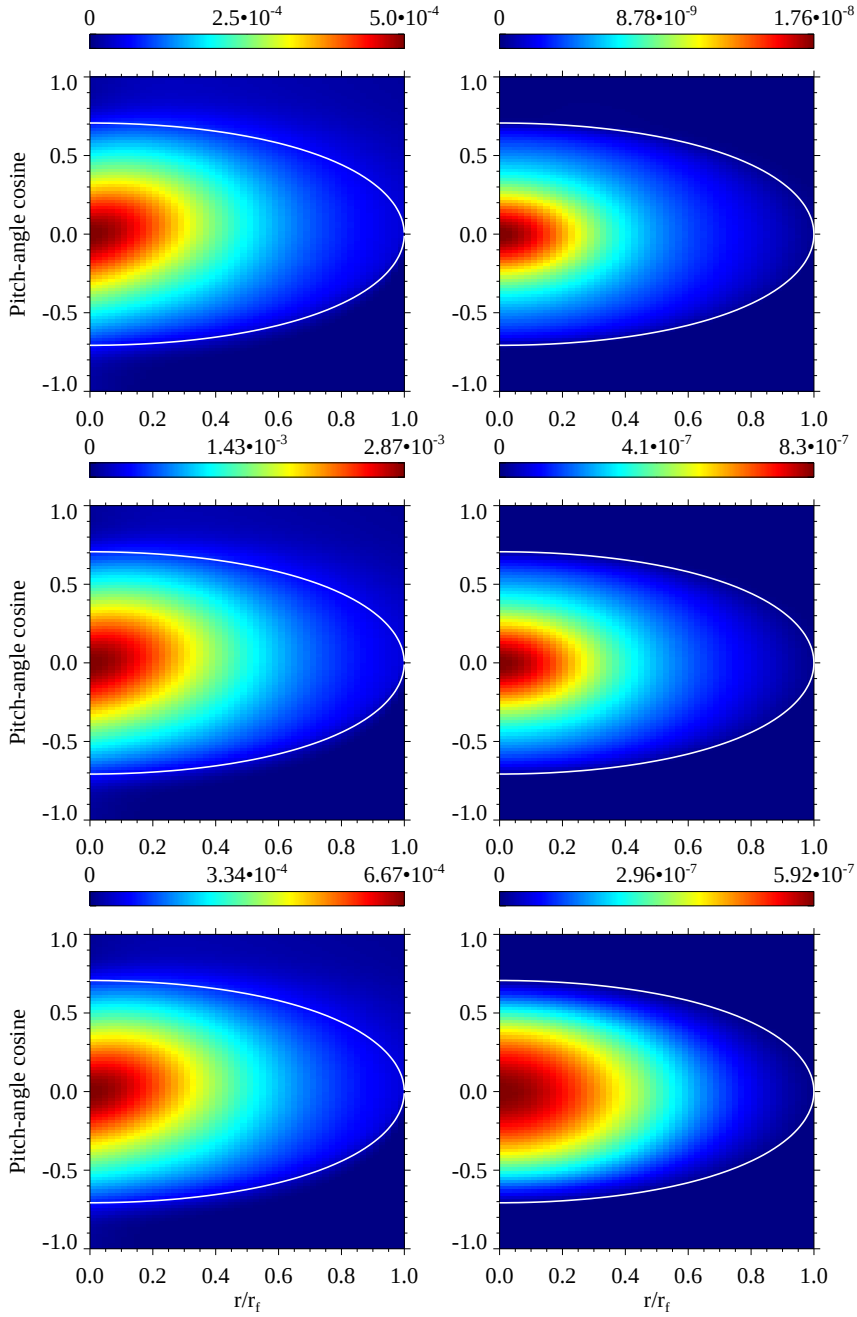

Figure 3.10: *From top to bottom*: Trapped electron distribution in phase space (r, μ) at $t = 10, 30$, and 50 s, calculated for an isotropic pitch-angle distribution of the injection flux. The left and right maps correspond to 100 keV and 1 MeV electrons, respectively. The horizontal axis corresponds to the spatial coordinates along the loop from the loop top to the footpoint, and the vertical axis corresponds to the pitch-angle cosine. The white solid lines denote the trajectory of the electron whose pitch angle is equal to the loss cone angle.

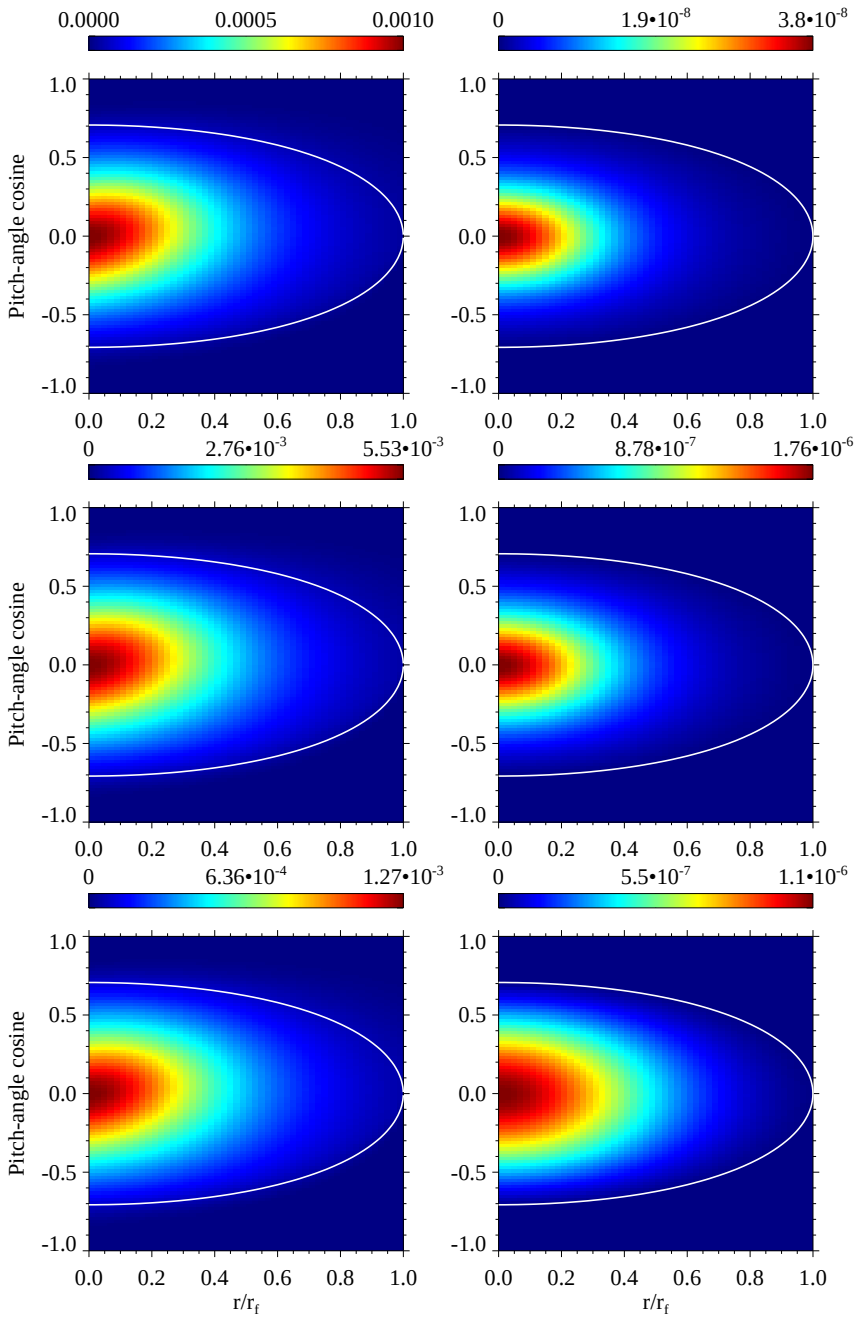

Figure 3.11: Same as Figure 3.10, but calculated for a pancake pitch-angle distribution of the injection flux.

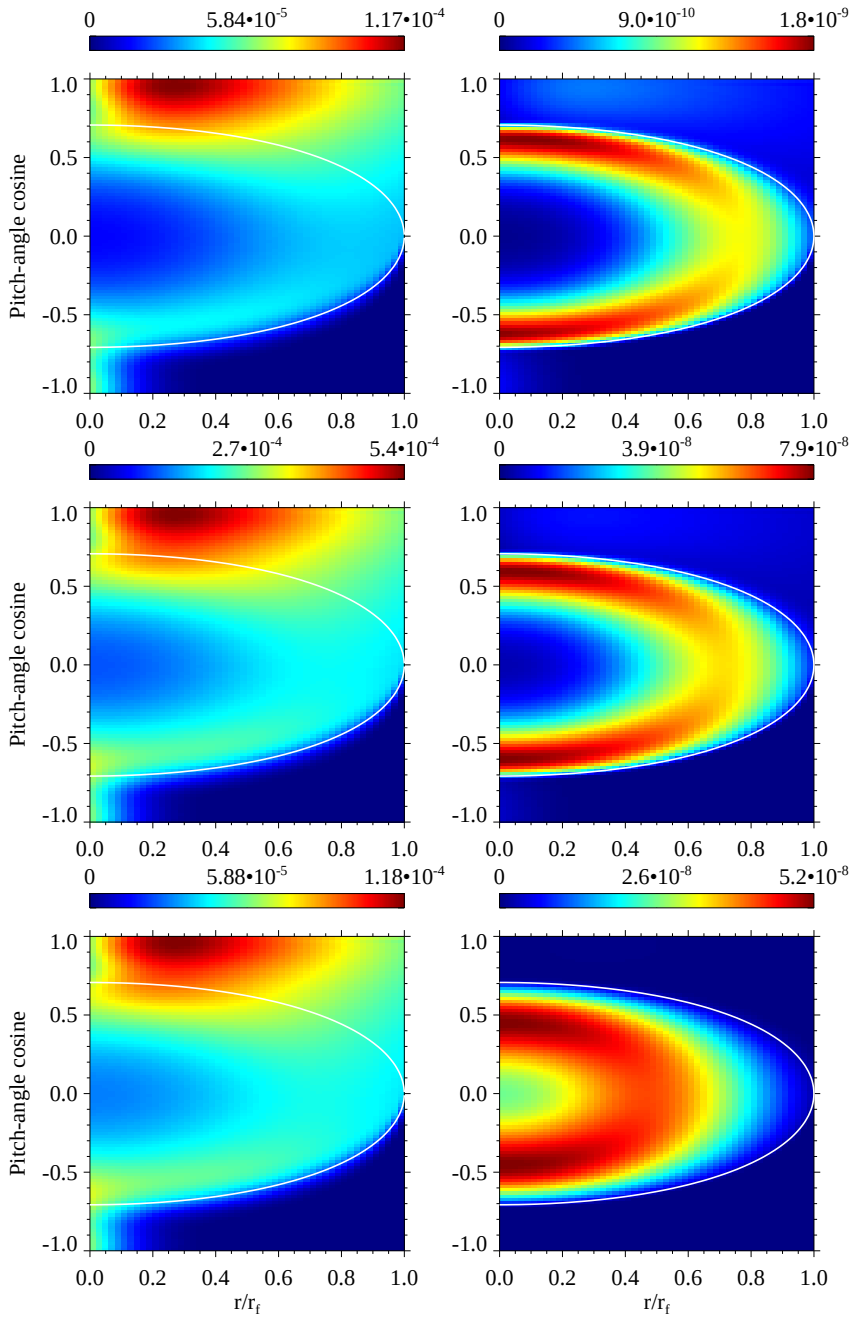

Figure 3.12: Same as Figure 3.10, but calculated for a beamlike pitch-angle distribution of the injection flux.

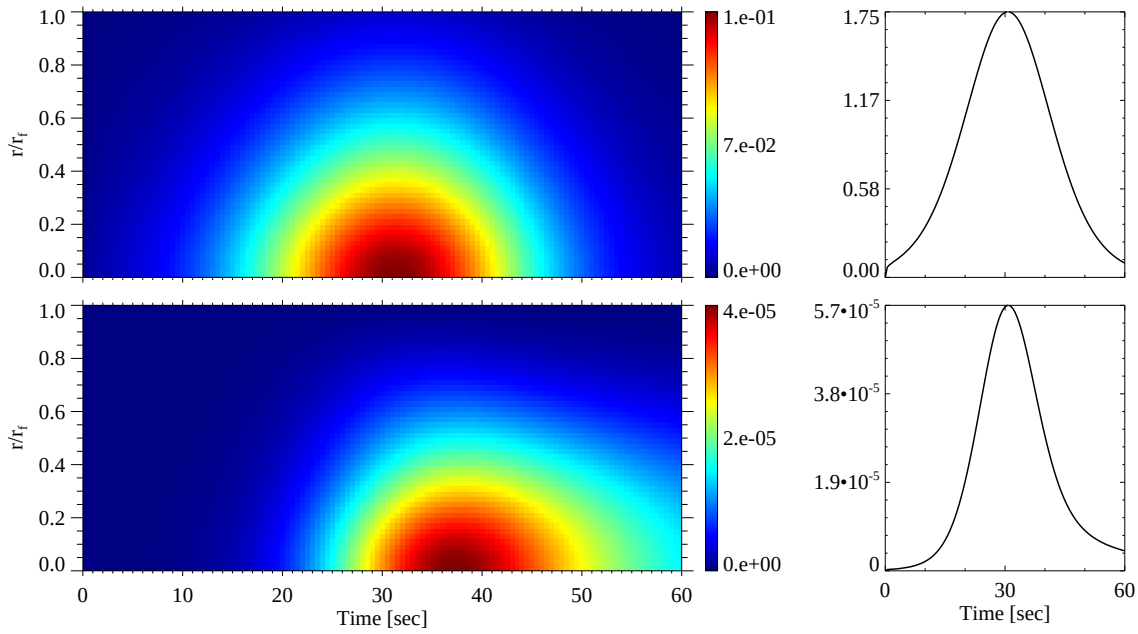

Figure 3.13: Time variations of the trapped and precipitating electrons calculated for the isotropic case. The top and bottom panels correspond to 100 keV and 1 MeV electrons, respectively. *Left*: Trapped electron number distribution $N_\mu(r, E, t)$. The vertical axis corresponds to the spatial coordinates along the loop from the loop top to the footpoint. *Right*: Precipitating electron flux $F_\mu(E, t)$.

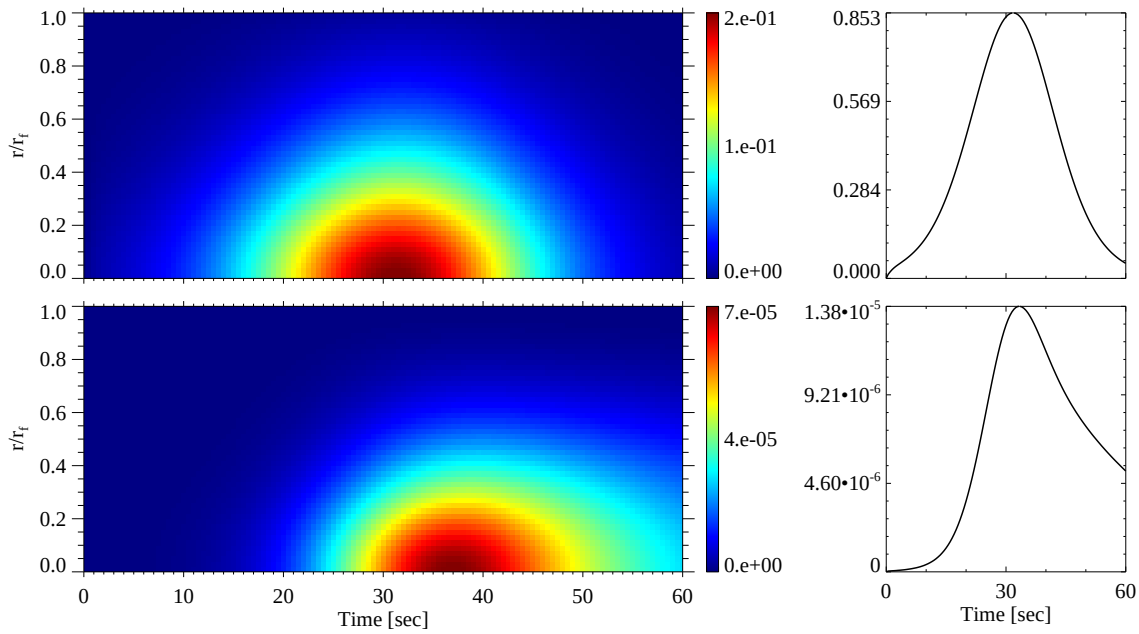

Figure 3.14: Same as Fig. 3.13, but calculated for the pancake case.

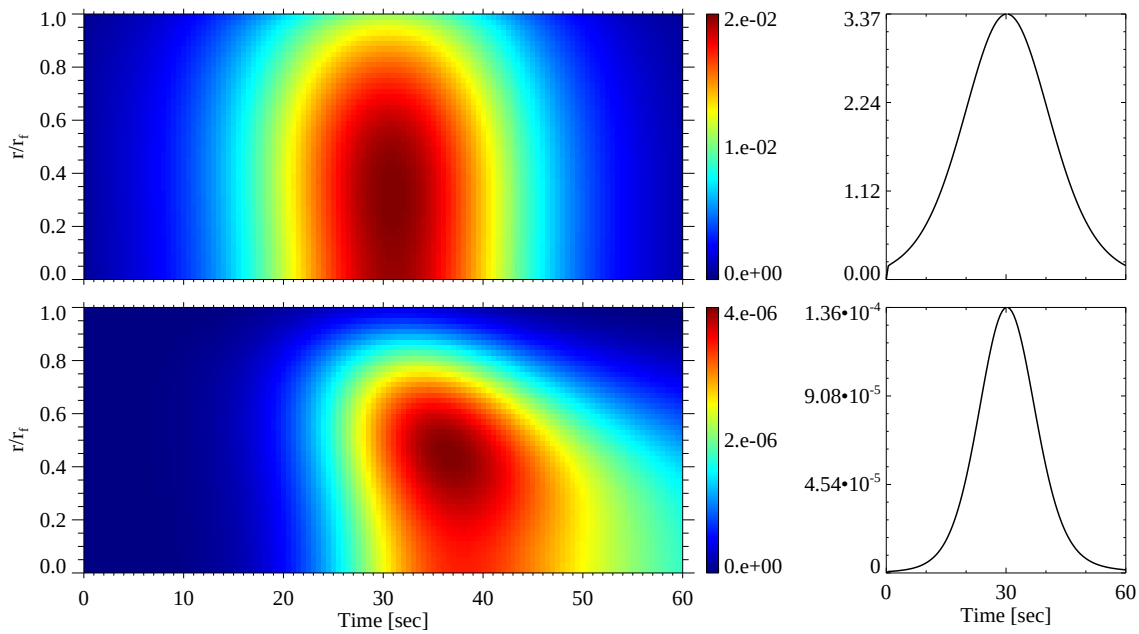

Figure 3.15: Same as Fig. 3.13, but calculated for the beamlike case.

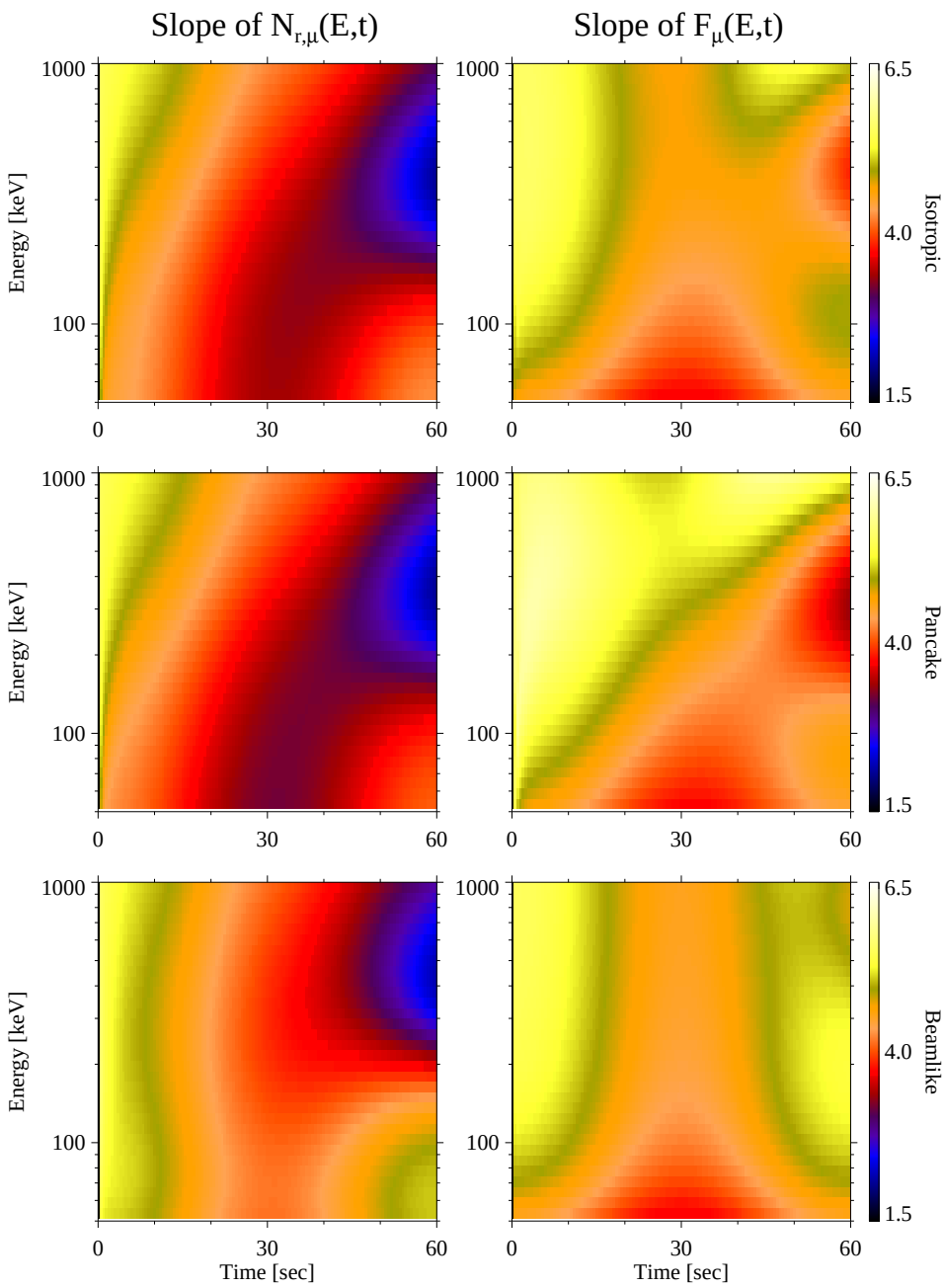

Figure 3.16: Time variations of the slope of $N_{r,\mu}(E,t)$ (left) and $F_\mu(E,t)$ (right) in energy, determined from the ratio at two adjacent energy grids (eq. (3.4.4)), calculated for the isotropic (top), pancake (middle), and beamlike (bottom) cases, respectively. Smaller value means a harder energy distribution.

3.4.2 Evolution of Radiation

In this section, we show the time evolution of the non-thermal emissions predicted by the calculated electron distributions, and compare them with the observations. The observed spatial distribution of the non-thermal emissions shows a loop-top microwave source and double-footpoint HXR sources (left panel of Fig. 3.3). This supports the interpretation that the trapped electrons $N(r, \mu, E, t)$ emit microwaves via gyrosynchrotron radiation (Ramaty, 1969; Dulk, 1985) and that the precipitating electrons $F(\mu, E, t)$ emit HXRs via thick-target bremsstrahlung (Brown, 1971). We numerically calculate the thick-target HXR intensity at a photon energy ϵ by

$$I_{\rm HXR}(\epsilon, t) = \frac{1}{4\pi R^2} \int_{\epsilon}^{\infty} dE F_{\mu}(E, t) \int_{\epsilon}^{E} dE' \frac{n v(E') \sigma_{\rm B}(\epsilon, E')}{E' \nu_{\rm E}(E')}, \qquad (3.4.7)$$

where $\sigma_{\rm B}(\epsilon, E)$ is the direction-integrated bremsstrahlung cross section given by Haug (1997), $\nu_{\rm E}$ is given in equation (3.3.2), and $R = 1$ AU. We use the pitch-angle integrated electron flux $F_{\mu}(E, t)$ because electrons precipitating into the thick-target region are quickly isotropized.

For the microwave emission, we numerically calculate the gyrosynchrotron emissivity from the trapped electrons $N(r, \mu, E, t)$ by using an approximate analytic expression given by Petrosian (1981) (see, Appendix D). Though a general description of gyrosynchrotron radiation includes absorption, this approximation is sufficient for our purpose because we discuss the microwave spectral behavior only in the optically thin regime (the electron plasma frequency, $\nu_{\rm pe} = 1.6\sqrt{n/(3 \times 10^{10}\ {\rm cm}^{-3})}$ GHz, is lower than the observation frequencies). We calculate the gyrosynchrotron emissivity in a harmonic range of $10 - 100$.

Since the gyrosynchrotron emissivity $j_{\nu}(r, \theta, t)$ depends on a magnetic field strength and a viewing angle θ with respect to the magnetic field line at the emission site as well as the parent electron distribution, we have to assume the magnetic field strength of the model potential magnetic field (eq. (3.3.6)) and its location, orientation, and tilt with respect to the solar surface (Fig. 3.8). We set magnetic field strengths at the loop top and footpoint of $B_0 = 300$ and $B_{\rm f} = 600$ Gauss, respectively. When the magnetic field strength at the emission site is on the order of 100 Gauss, the frequency range in our calculation corresponds to the observation range of NoRP and NoRH. For the determination of θ, we employ an ideal case that the loop is located

at the disk center without the tilt with respect to the solar surface. In this case, θ is written as a function of r from the model magnetic field configuration (eq. (3.3.5)),

$$\theta(r) = \cos^{-1}\left[-\tanh(kr)\right]. \tag{3.4.8}$$

Finally, we calculate the gyrosynchrotron intensity $I_\nu(r, \theta, t)$, which is the observed variable, for comparison with the observation. This can be calculated by considering the projection effect of the loop by an observer,

$$I_\nu(r, \theta, t) = j_\nu(r, \theta, t)\frac{\sqrt{A(r)}}{\sin\theta(r)}, \tag{3.4.9}$$

where $A(r)$ is the cross-sectional area of the loop determined from the conservation of the magnetic flux, $B(r)A(r) = \text{constant}$.

Light Curves

Figure 3.17 shows the light curves of the non-thermal emissions in three cases. The upper panels show the HXR fluxes at 50, 100, and 200 keV. The lower panels show the total microwave fluxes at 17 and 34 GHz, which are obtained by integrating $I_\nu(r, \theta, t)$ over space. The dashed lines denote the peak times in the HXR 50 keV flux. Emissions from higher energy electrons (higher energy HXRs and microwaves) are delayed from the HXR 50 keV flux by 1-8 s. Such delays have been often reported (e.g., Cornell et al., 1984; Kosugi et al., 1988) and also observed in the 2003 May 29 flare (§ 3.2.1).

Here we only show the thick-target HXR emissions from the precipitating electrons. The trapped electrons can emit HXRs. Since the ambient plasma number density at the trap region is low ($n = 3 \times 10^{10}$ cm^{-3}), they would emit via thin-target bremsstrahlung. We estimate the intensity of the thin-target HXRs produced by them. In the isotropic and beamlike cases, this is less than about 10 % of the intensity of the thick-target HXRs from the footpoint. In the pancake case, this is about 20 % of the intensity of the thick-target HXRs from the footpoint, but still low. We consider that this is consistent with the observation within the uncertainty of the modeling. Therefore we neglect the HXR emissions by the trapped electrons.

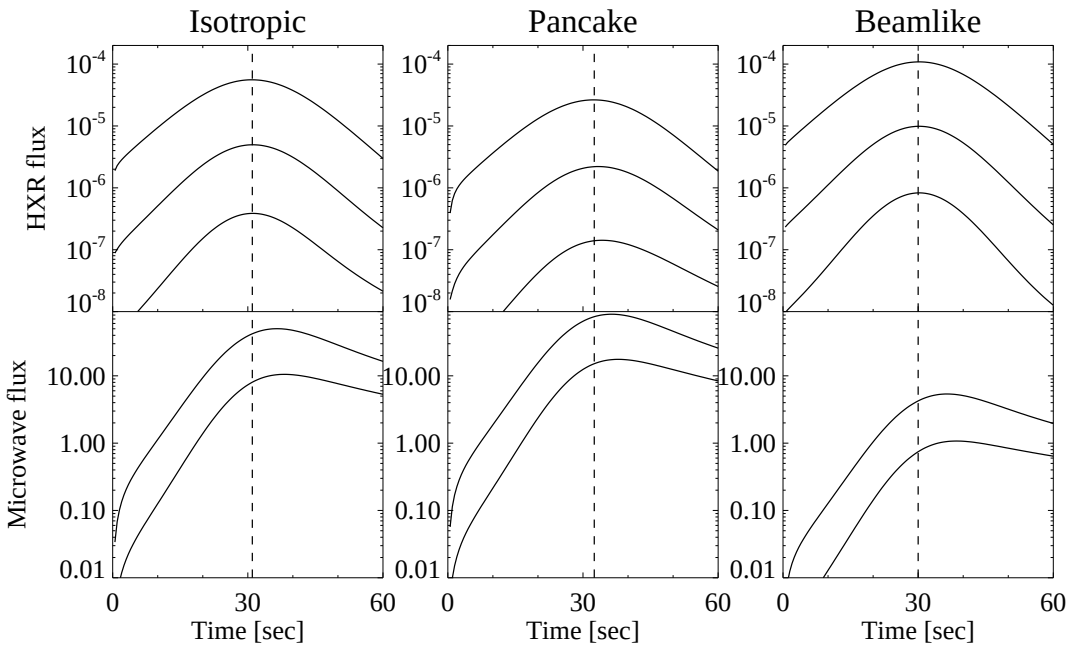

Figure 3.17: Light curves of the non-thermal emissions, calculated for the isotropic (left), pancake (center), and beamlike (right) cases, respectively. The upper panels show the HXR fluxes at 50, 100, and 200 keV from top to bottom. The lower panels show the total microwave fluxes at 17 and 34 GHz from top to bottom. The dashed lines denote the peak times in the HXR 50 keV flux.

Images

Figure 3.18 shows the temporal variation of the 17 GHz gyrosynchrotron intensity distributions along the loop. The vertical axis corresponds to the spatial coordinates from the loop top to the footpoints. The maximum of the vertical axis is smaller than unity because of the projection effect of the loop. As expected in § 3.4.1, the microwaves are emitted primarily at the loop top in the isotropic (top) and pancake (middle) cases. This is in agreement with the observation (§ 3.2.2). The microwave distribution in the beamlike case (bottom) is different from that in the isotropic and pancake cases. Emissions primarily come from the intermediate position ($x \sim 0.4r_{\rm f}$) between the loop top and footpoint, which corresponds to the site where the 1 MeV electrons are situated (bottom left panel of Fig. 3.15). The loop-top region is not bright for the microwave that is not consistent with the observation. Therefore the beamlike pitch-angle distribution is not adequate for the microwave-emitting electrons

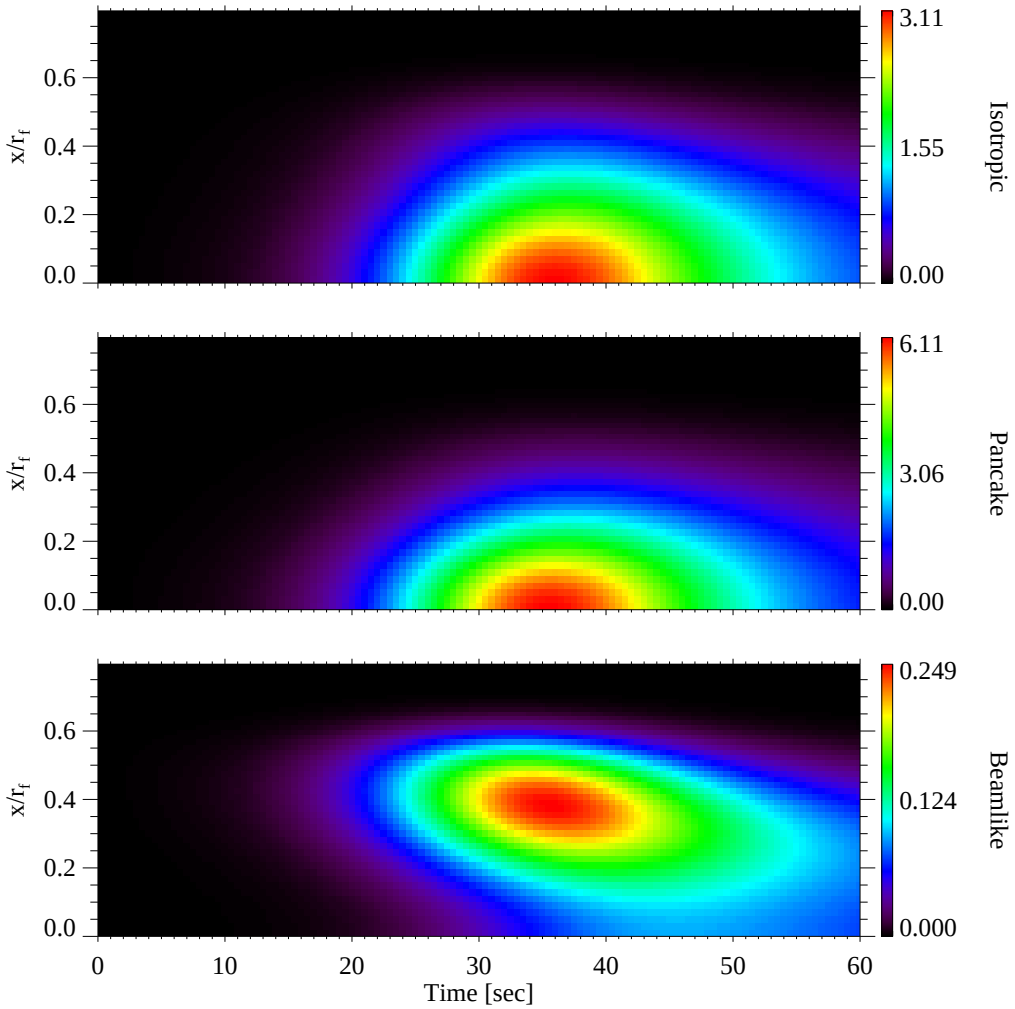

Figure 3.18: Time variation of the 17 GHz gyrosynchrotron intensity distributions along the loop, calculated for the isotropic (top), pancake (middle), and beamlike (bottom) cases, respectively. The vertical axis corresponds to the spatial coordinates from the loop top to the footpoint. Note that the maximum of the vertical axis is smaller than unity because of the projection effect of the loop.

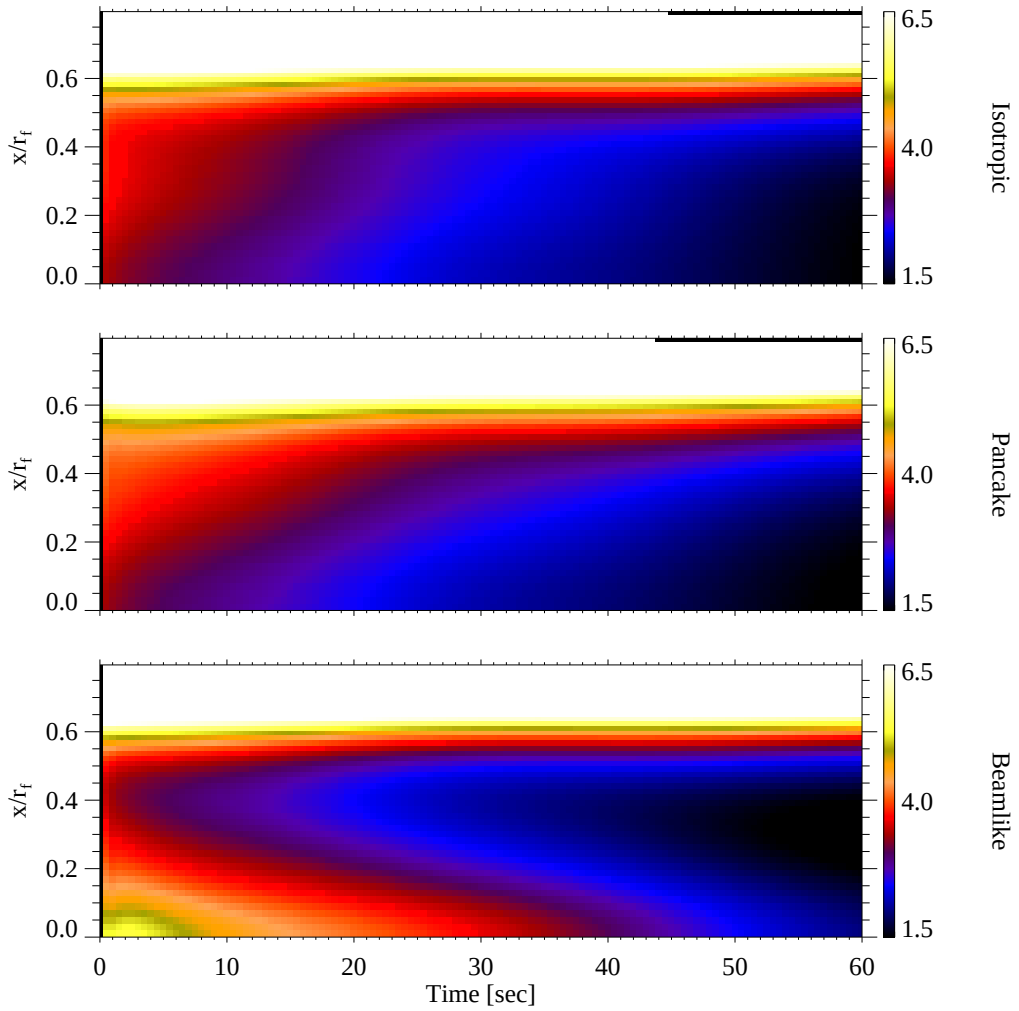

Figure 3.19: Time variation of the microwave spectral index distributions along the loop, calculated for the isotropic (top), pancake (middle), and beamlike (bottom) cases, respectively. Smaller value means a harder spectrum. The vertical axis corresponds to the spatial coordinates from the loop top to the footpoint. Note that the maximum of the vertical axis is smaller than unity because of the projection effect of the loop.

($\sim$ 1 MeV).

The gyrosynchrotron emission is primarily emitted by the electrons with the pitch-angle cosine of $\mu \sim \beta \cos\theta$ (Petrosian, 1981; Lu & Petrosian, 1990). A number of electrons with $\mu \sim 0$ are necessary at the loop top for the strong microwave emission, because $\theta = 90°$ at the loop top (eq. (3.4.8) with $r = 0$). The right panels of Figure 3.12 show a large number of 1 MeV electrons at the loop top ($r = 0$), but their pitch-angle cosine is not zero. Therefore the loop-top region is not bright for the microwave in the beamlike case.

From the microwave distribution $I_\nu(r, \theta, t)$, we calculate the microwave spectral index from 17 to 34 GHz at each time and position by fitting it with a single power-law function. Figure 3.19 shows the temporal variation of the microwave spectral index distributions along the loop. In all cases, the hardest microwave emissions come from the site where the 17 GHz intensity is the brightest (see, Fig. 3.18). For example, the spectral index is ~ 2.2 at $x = 0$, ~ 3 at $x \sim 0.5r_{\rm f}$, and quite soft for $x > 0.6r_{\rm f}$, at $t = 30$ s in the isotropic case. This means that the higher frequency microwave source size is smaller than the lower frequency one. This is in agreement with the observation (Fig. 3.4).

Above result is expected from the parent electron distribution in Figures 3.13 through 3.15. Since higher frequency gyrosynchrotron radiation is emitted by more energetic electrons, the higher frequency microwave source size is smaller than the lower frequency one when the higher energy electrons are confined to a narrower region. Confinement of the higher energy electrons to a narrower region is realized when the precipitation rate (eq. (3.4.5)) is negatively associated with energy, i.e., $\delta < 0$ (weak diffusion). Therefore the observed difference of the microwave source size between 17 GHz and 34 GHz can be interpreted by the TPP model in the weak diffusion regime, which thus supports our modeling.

In all cases, the microwave spectrum hardens with time. Our calculations of the TPP model can successfully reproduce the often observed soft-hard-harder behavior of the microwave spectrum (Silva et al., 2000). This is because the energy distribution of the gyrosynchrotron-emitting electrons ($\sim$ 1 MeV) hardens with time (left panels of Fig. 3.16). We next compare the temporal variation of the microwave spectrum with that of the HXR spectrum.

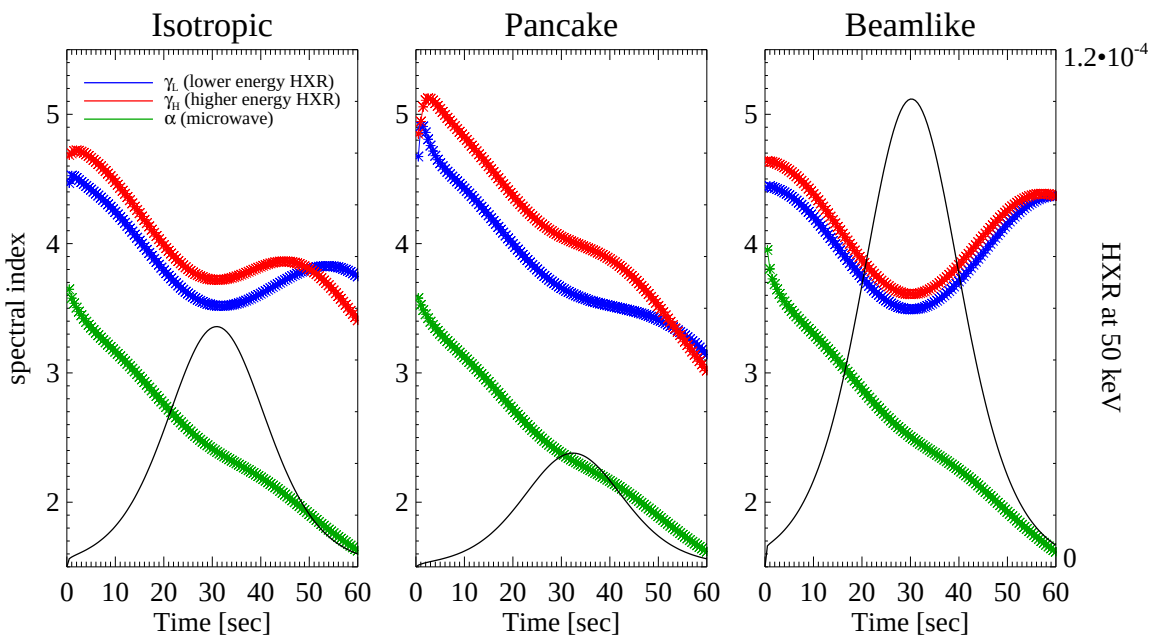

Figure 3.20: Time profiles of the spectral indices of the non-thermal emissions, calculated for the isotropic (left), pancake (center), and beamlike (right) cases, respectively. The blue, red, and green symbols denote $\gamma_{\rm L}^{\rm FP}(t)$, $\gamma_{\rm H}^{\rm FP}(t)$, and $\alpha^{\rm FP}(t)$. The solid lines denote the predicted HXR flux at 50 keV (in linear scale).

Spectra

To illustrate the spectral variation of the calculated emissions, we fit the HXR spectrum (eq. (3.4.7)) within 50-200 keV at each time with the double power-law function of equation (3.2.1). We also fit the spectrum of the total microwave intensity from 17 to 34 GHz at each time with a single power-law function.

Figure 3.20 shows the time profiles of the spectral indices of the non-thermal emissions in three cases. Colors (blue, red, and green) denote the lower energy HXRs, the higher energy HXRs, and the microwaves, respectively. We will refer to the spectral indices of the lower energy HXRs, the higher energy HXRs, and the microwaves in the calculated spectrum as $\gamma_{\rm L}^{\rm FP}(t)$, $\gamma_{\rm H}^{\rm FP}(t)$, and $\alpha^{\rm FP}(t)$, respectively.

The results show some agreements with the observations. The values of the microwave spectral indices are smaller by 1-2 than those of the HXR spectral indices in all cases. This result is quantitatively consistent with not only our observations but also previous reports (e.g., Silva et al., 1997, 2000). This is understood by using

simple analytic formulae that relate the spectral indices of the emissions to those of the parent electrons. We assume that the trapped electrons have a power-law energy distribution, $N_{r,\mu}(E) \propto E^{-\Delta}$. Dulk (1985) gives an empirical relationship of the spectral indices between the gyrosynchrotron intensity in the optically thin regime and the parent electron energy distribution at the site,

$$\alpha = 0.9\Delta - 1.22. \tag{3.4.10}$$

Though this relationship is derived with the assumption that parent electrons have an isotropic pitch-angle distribution, we use it for a rough estimate of the microwave spectral index from electrons with an arbitrary pitch-angle distribution. For HXRs, we can use equation (3.4.5), which shows the energy distribution of the precipitating electron flux, $F_\mu(E) \propto E^{-(\Delta-\delta)}$. An analytic expression for non-relativistic thick-target bremsstrahlung gives the relationship of the spectral indices between the HXR photon flux and the parent electron flux precipitating into the thick-target region (e.g., Hudson, 1972; Tandberg-Hanssen & Emslie, 1988),

$$\gamma = (\Delta - \delta) - 1. \tag{3.4.11}$$

Subtracting equation (3.4.10) from equation (3.4.11), we find the difference of the spectral indices between the HXR and microwave,

$$\gamma - \alpha = 0.1\Delta - \delta + 0.22. \tag{3.4.12}$$

In the weak diffusion regime, δ takes negative value, around -1.0 in our calculations of the isotropic and pancake cases (Fig. 3.9). This eventually yields $\gamma - \alpha \sim 1.5$ (for $\Delta = 3$), which is in agreement with the observations. Thus we conclude that the difference of the spectral indices between the HXR and microwave emissions can be interpreted as a consequence of parent electron transport in the TPP model in the weak diffusion regime.

There is no much difference in the time profiles of $\alpha^{\rm FP}(t)$ in three cases, in that all show hardening with time. This is because the time evolution of the energy distribution of the parent electrons ($\sim$ 1 MeV trapped electrons) is not influenced by the injection pitch-angle distribution (left panels of Fig. 3.16). On the other hand, the time profiles of the HXR spectra ($\gamma_{\rm L}^{\rm FP}(t)$ and $\gamma_{\rm H}^{\rm FP}(t)$) behave differently in

three cases. In the beamlike case (right plot of Fig. 3.20), $\gamma_{\rm H}^{\rm FP}(t)$ as well as $\gamma_{\rm L}^{\rm FP}(t)$ show the SHS behavior, reflecting the instantaneous injection profile. In the isotropic and pancake cases (left and center plots), however, their profiles are different from those in the beamlike case. In the isotropic case, $\gamma_{\rm H}^{\rm FP}(t)$ and $\gamma_{\rm L}^{\rm FP}(t)$ keep the SHS behavior, but slightly harden after $t = 50$ s. This is due to a contribution of the trap-precipitating electrons whose precipitation timescale is comparable to the injection timescale. The influence of the trap-precipitating electrons on the emission spectra can be more prominently seen in the pancake case. In this case, $\gamma_{\rm H}^{\rm FP}(t)$ as well as $\gamma_{\rm L}^{\rm FP}(t)$ do not show the SHS behavior but harden with time, similar to $\alpha^{\rm FP}(t)$. This is because the evolution of the parent electrons significantly deviate from the injection profile of the SHS (middle right panel of Fig. 3.16).

We observed that the time profile of $\gamma_{\rm H}^{\rm obs}(t)$ is more similar to that of $\alpha^{\rm obs}(t)$ than to that of $\gamma_{\rm L}^{\rm obs}(t)$, which only show the SHS. During the decay phase of the spike in the observation (Fig. 3.6, 01:03:30 - 01:04:00 UT), for example, both $\gamma_{\rm H}^{\rm obs}(t)$ and $\alpha^{\rm obs}(t)$ show hardening whereas $\gamma_{\rm L}^{\rm obs}(t)$ shows softening. In our modeling, the similarity between $\gamma_{\rm H}^{\rm FP}(t)$ and $\alpha^{\rm FP}(t)$ is the most clearly seen in the pancake case, while the SHS behavior of $\gamma_{\rm L}^{\rm FP}(t)$ is well seen in the isotropic and beamlike cases. By comparing the observation and the calculation, we conclude that it is reasonable to consider that the higher energy HXR-emitting electrons have a pancake pitch-angle distribution while the lower energy HXR-emitting electrons have an isotropic or a beamlike pitch-angle distribution, that is, the non-thermal electrons are accelerated more perpendicular to than parallel to the magnetic field lines until they are injected into the flare site.

3.5 Summary and Discussion

We presented a comparative study of the non-thermal emissions during the main impulsive phase of the 2003 May 29 flare, by using the *RHESSI* HXR and Nobeyama microwave observations. We also considered the electron transport of TPP, to explain the observations and determine the injection pitch-angle distribution.

We implemented the detailed analysis of the higher energy HXRs above 100 keV that has been less studied so far. The higher energy HXRs are emitted at the foot-

points of the loop in the same manner as the lower energy HXRs, indicating that they are emitted by the precipitating electrons. We presented the time profiles of the spectral indices of the higher energy HXRs $\gamma_{\rm H}^{\rm obs}(t)$ as well as the lower energy HXRs $\gamma_{\rm L}^{\rm obs}(t)$ and microwaves $\alpha^{\rm obs}(t)$. We found that the time profile of $\gamma_{\rm H}^{\rm obs}(t)$ is more similar to that of $\alpha^{\rm obs}(t)$ than to that of $\gamma_{\rm L}^{\rm obs}(t)$, and is delayed from that of $\gamma_{\rm L}^{\rm obs}(t)$.

We interpreted these observations in terms of the electron transport of TPP. The TPP model in the weak diffusion regime yields the energy-dependent difference of the electron distributions that can explain (1) the difference of the microwave source size, and (2) the difference of the values of the spectral indices. From both the observational and numerical studies, we can utilize the spectrum of the higher energy HXR for the diagnostic on the pitch-angle distribution of the injected electrons, and concluded that the observed temporal variation of $\gamma_{\rm H}^{\rm obs}(t)$ can qualitatively be explained if the parent electrons have a pancake rather than beamlike pitch-angle distribution when they are injected.

Based on these results, we address a possible mechanism yielding such pitch-angle distribution of the injected electrons. In chapter 2, we concluded that in the main impulsive phase the geometry of this flare is explained by the two-dimensional CSHKP magnetic reconnection model. Here we consider the electron acceleration mechanism in this framework. When the magnetic reconnection is triggered, electrons are initially accelerated around the X-point (Imada et al., 2005). The reconnection energy release point (X-point) is thought to be above the flare loop, which is seen in microwave and EUV. The electrons are transported toward the reconnection downstream region with being frozen into the reconnected field line. During this convection, they can be adiabatically accelerated with conserving two different adiabatic invariants. The first invariant relates the particle perpendicular energy ($E_\perp$) and the magnetic field strength, called the magnetic moment, $E_\perp/B =$ constant. If the magnetic field strength increases, its perpendicular energy increases (Karlický & Kosugi, 2004). This is the betatron acceleration process. The second invariant, named longitudinal invariant, relates the particle parallel velocity ($v_\parallel$) and its characteristic travel length ($r_{\rm c}$) along the field line, $v_\parallel r_{\rm c} =$ constant. If the characteristic travel length decreases, the parallel velocity increases (Somov & Kosugi, 1997). This is the Fermi acceleration process. In the CSHKP model, the reconnected field line moves toward the solar

surface from the upper corona. Then the magnetic field strength of the line would be increased and the length of the line would be decreased by the convection. Therefore electrons have a possibility to be adiabatically accelerated both in perpendicular (via betatron) and parallel (via Fermi) directions. Electrons can be accelerated more perpendicular to than parallel to magnetic field lines when the betatron process works more efficiently than the Fermi process.

In the modeling, we gave the injected electrons with the energy distribution extending to 5 MeV (high energy cutoff). This energy is larger than the effective energy ~ 1 MeV of the 17 and 34 GHz microwave-emitting electrons (with B of order of 100 Gauss). The results and discussion do not change when the high energy cutoff is larger than this value, because electrons with such an extremely high energy can not contribute to the emissions of our interest. However, the results would drastically change when the high energy cutoff is small. If the high energy cutoff is around ~ 1 MeV or less, the resulting microwave emissions are considerably reduced due to a lack of energetic electrons, particularly on 34 GHz. This yields significant softening of the spectrum of the microwave intensity that is inconsistent with the observations. By this reason, we considered that the injected electrons have the energy distribution extending to the energy which is larger than the effective energy of the microwave-emitting electrons.

We assumed that the injected electrons have a single power-law energy distribution ranging 50 to 5000 keV with the SHS behavior. This means that these electrons are from the same population, having the same history of the acceleration. If different kind of accelerations work on electrons with different energies, it is not necessarily that low energy electrons and high energy ones behave similarly in time. We consider that this is not in our case. The observation showed that the time profiles of $\gamma_{\rm H}^{\rm obs}(t)$ ($\alpha^{\rm obs}(t)$) and $\gamma_{\rm L}^{\rm obs}(t)$ have a correlation with a time delay (bottom panels of Fig. 3.6), indicating that the parent electrons are temporally correlated with each other. Though such correlation has not be obtained from our calculation yet, we consider that it is reasonable to assume that the electrons emitting lower energy HXRs, higher energy HXRs, and microwaves have a same time profile when they are injected into the loop.

We can consider a more general form of the energy distribution of the injected

electrons such as a double power-law. If the time profile of the spectral index of this injected electrons in the higher energy part is delayed from that in the lower energy part, it is naturally expected without considering the TPP effect that the time profile of the spectral index of the resulting higher energy HXRs is delayed from that of the lower energy HXRs. However, we can not explain the similarity of the time profiles between $\gamma_{\rm H}^{\rm obs}(t)$ and $\alpha^{\rm obs}(t)$ without the TPP effect, because the microwave shows the profile of the trapped electrons that is different from the injection profile. The similarity of the time profiles between $\gamma_{\rm H}^{\rm obs}(t)$ and $\alpha^{\rm obs}(t)$ is an evidence that the time profile of $\gamma_{\rm H}^{\rm obs}(t)$ is controlled by TPP, not is the instantaneous injection profile.

In our current study, we have modeled with nominal parameters: the ambient plasma number density n and the mirror ratio M. Since these parameters affect the evolution of electrons, we have to systematically investigate the set of parameters with which we can reproduce the observations. We believe that n of an order of 10^{10} cm^{-3} from the *GOES* observation and the mirror ratio of $1.2 - 3$ derived by Aschwanden et al. (1998) are reasonable ranges. A much higher mirror ratio drastically reduces the number of precipitating electrons and the resultant thick-target HXR emissions at the footpoints, which may be in disagreement with the observations. A much higher density ($n \gtrsim 10^{11}$ cm^{-3}) at the trap region would produce strong HXR emissions at the corona via thin-target bremsstrahlung radiation, which is rarely observed. As such, we consider that a relatively lower density at the trap region (less than that of the SXR bright loop) and a relatively smaller mirror ratio should be reasonable, and thus we believe the values adopted in our calculation, $n = 3 \times 10^{10}$ cm^{-3} and $M = 2$, are in reasonable ranges. To achieve a better agreement between the calculation and the observation, we need to further refine the model distribution of the injection flux.

Lee et al. (2000) and Lee & Gary (2000) reported the microwave observation of a *GOES* C2.8 flare on 1993 June 3. They further performed the calculations of the TPP model by using the spatially-homogeneous Fokker-Planck equation. They carried out a systematic investigation by varying the number density and the injection timescale as well as the injection pitch-angle distribution, to search for the best parameter set that agreed with their observation. They concluded that the electrons are confined to a narrow range ($|\mu| \lesssim 0.26$) of pitch angle and are injected into a low density ($n \sim 4 \times 10^9$ cm^{-3}) trap region. This number density is much lower than that we

assumed in this study. This may be because we observed a large X-class flare while they observed a small C-class flare.

The electron distributions in our model maintain the pitch-angle anisotropy (Figs. 3.10 through 3.12). Electrons with such pitch-angle distributions are unstable in nature, exciting the plasma waves such as whistler and Langmuir waves to be isotropized. This is not included in our model. If the pitch-angle scattering by these waves is much faster than that by Coulomb collisions, it would violate the condition of the weak diffusion ($\delta < 0$) that could not explain the observed characteristics. Then we consider that, at least in our case, the pitch-angle scattering by these waves is not strong and the weak diffusion regime is maintained. Kosugi et al. (1988) reported flares that show a non-thermal microwave emission lasting tenths of minutes after the peak without any HXR signal. These microwaves originate from $\gtrsim 1$ MeV electrons, which might be strongly trapped in a loop via wave-particle interactions. During the trap, they could be accelerated by strong turbulent waves.

Our interpretation of the difference of the spectral indices between the HXRs and microwaves based on the TPP model is subject to the observation that microwaves are emitted mainly at the loop top whereas HXRs are emitted at the footpoints. Therefore this interpretation is inadequate for a flare that shows, for example, microwaves as well as HXRs at the footpoints. In such a flare, the microwave-emitting electrons are identical to the HXR-emitting ones. This means $F(E) \propto \beta N(E)$, i.e., $\delta = 0.5$ in equation (3.4.5), yielding $\alpha \simeq \gamma$ in equation (3.4.12). The footpoint microwave emissions would thus be expected to have almost the same value of the spectral index as the footpoint HXRs.

Takasaki et al. (2007) performed an imaging spectroscopy of a flare occurred on 2000 November 25 by using *Yohkoh* and NoRH. This flare shows one HXR footpoint source at the east end of the loop, a loop-top microwave source, and another microwave footpoint source at the west which is the conjugate of the HXR footpoint source. They found that the footpoint microwave emission has a softer spectral index than the loop-top one by ~ 2, and the time profile of its spectrum is similar to that of the HXR spectrum rather than that of the loop-top microwave spectrum. This is well explained by TPP, as they suggested. However, the spectral indices of the footpoint HXR and microwave sources do not follow our expectation of $\alpha \simeq \gamma$, indicating

that the energy distributions of the precipitating electrons at the conjugate footpoints are different from each other. The possible reason to explain this discrepancy is the asymmetry of the loop condition that the magnetic field strengths are -70 Gauss at the HXR footpoint and $+800$ Gauss at the microwave footpoint. The asymmetric footpoint condition yields an asymmetric distribution of the precipitating electrons in energy and pitch-angle space, which results in asymmetric emissions (Sakao, 1994; Alexander & Metcalf, 2002; Goff et al., 2004). Therefore, detailed investigation on the asymmetry in the footpoint emissions may help the further study of the injection electrons (e.g., McClements & Alexander, 2005).

Chapter 4

Energy-Dependent Distribution of Non-Thermal Emissions in the Early Impulsive Phase

In this chapter we analyze the non-thermal emissions during the early impulsive phase (01:00:00 -01:02:00 UT) of the 2003 May 29 flare. In particular, we focus on the spatial variation of HXRs. We found that the footpoint HXR source, appeared at the northwest site with stronger magnetic field, is brighter (weaker) for the lower (higher) energy than its conjugate footpoint source with weaker magnetic field. We explain this energy-dependent asymmetry of the double-footpoint HXR sources in terms of the energy-dependent difference of the pitch-angle distribution of the parent electrons. The observed characteristics of the HXR images can be interpreted as a consequence of the electron acceleration parallel to the magnetic field line.

4.1 Motivation

In the previous chapter, we studied the electron transport model of trap-plus-precipitation, to explain the observation of the 2003 May 29 flare. To do this, we assumed that the flare is approximated by the two-dimensional CSHKP model and the loop is symmetric. The actual flares often show much complex three-dimensional structure and the asymmetric loop(s). Figure 4.1 shows the enhancement of the white

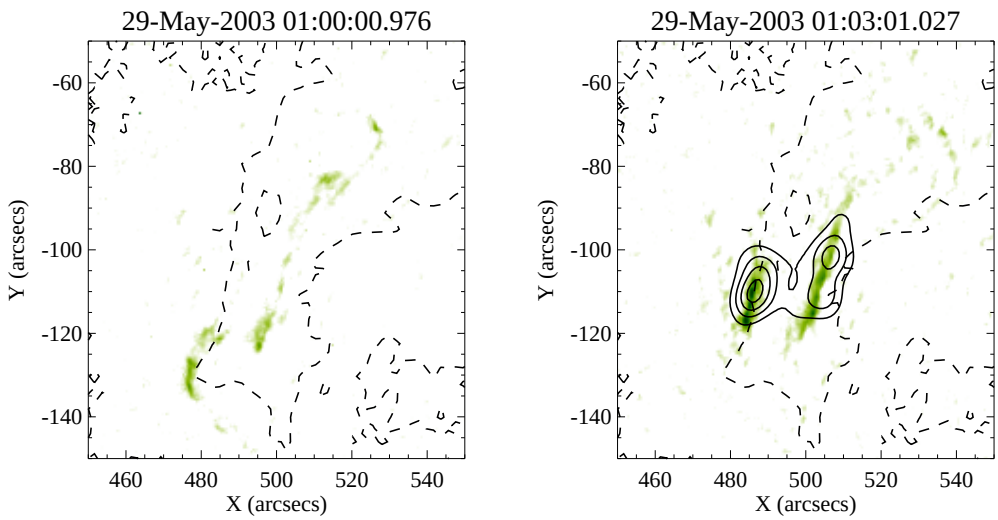

Figure 4.1: White light images taken with the *TRACE* WL channel at 01:00:01 (left) and 01:03:01 (right) UT. These images are drawn after removing the static features of the photosphere such as sunspots, to emphasize the flare-associated emissions. The solid contours in the right map are the *RHESSI* 40-100 keV image at 01:03:00 UT. The accumulation time for making this image is 12.48 s. The dashed contours denote the photospheric magnetic neutral lines. Solar north is up and west is to the right.

light emission associated with the 2003 May 29 flare at 01:00:01 (left) and 01:03:01 (right) UT, taken with the *TRACE* WL channel. The former corresponds to the time before the first peak of the non-thermal emissions, and the latter corresponds to the time between the second and third peaks (see, Fig. 2.3 for the non-thermal light curves). In the right map, the white light emissions are quasi-symmetrically distributed with respect to the photospheric magnetic neutral line and co-spatial with the HXR footpoint sources (solid contours).

On the other hand, the white light emissions at 01:00:01 UT show complicated spatial distribution. There are discrete emission sites of southeast around [480,-130], southwest around [495,-120], west around [510,-80] and northwest [525,-70]. Probably the southeast site is magnetically connected with the west sites. At this period the HXR emission is very weak (Fig. 2.3). We do not overlay the corresponding HXR image in the left map because we can not make the image at this period with sufficient quality (we later show HXR images taken after this period).

Recent observations with *Yohkoh*, *TRACE*, *RHESSI*, and *Hinode* have shown that

the flare white light emissions well correlate with the HXR emissions both in space and time (Matthews et al., 2003; Hudson et al., 2006; Xu et al., 2006; Isobe et al., 2007). Metcalf et al. (2003) and Fletcher et al. (2007) carried out a quantitative estimation of the power of the white light emissions and they suggested that the low energy ($\sim$ 20 keV) non-thermal electrons are the most powerful candidate for the primal energy source of the white light emissions. The left map of Figure 4.1 implies that, in the early impulsive phase of this flare, the energy release and particle acceleration occurred in a complex magnetic field configuration that might be beyond the scope of the CSHKP model. We analyzed in detail the HXR images during the early impulsive phase (01:00:00 - 01:02:00 UT) in order to obtain different insights on the flare non-thermal emissions and electrons from those obtained in chapter 3.

HXR Asymmetry

It is known that HXR sources, located at both ends of a flare loop (double footpoints), frequently show an asymmetry both in their intensity and spectrum. Sakao (1994) analyzed flares with double-footpoint HXR sources observed with *Yohkoh*. He found that in four out of five events the brighter HXR source has a harder spectrum and is located at the site with weaker magnetic field. He interpreted this relativeness in terms of the magnetic mirroring effect of parent electrons. Since the magnetic mirror force is weaker and the loss cone is larger at the footpoint with weaker magnetic field, a larger number of electrons can reach this footpoint and penetrate deeper in the chromosphere. Since the ambient plasma density increases with decreasing height relative to the solar surface, electrons can more efficiently emit HXRs via bremsstrahlung at the deeper chromosphere. As a result, the HXR emission at the footpoint with weaker magnetic field is brighter and harder.

However, there have been reported flares that do not follow the Sakao's scenario but show an opposite trend. Goff et al. (2004) statistically analyzed the sample of 32 flares observed with *Yohkoh* and found that about 30% of them show the brighter HXR source located at the footpoint with stronger magnetic field. Falewicz & Siarkowski (2007) suggested that the HXR source at the footpoint with stronger magnetic field could be brighter if electrons are not injected at an apex of the loop but at the site close to this footpoint.

Alexander & Metcalf (2002) advanced this kind of study by using *RHESSI*. *RHESSI* allows us to make HXR images with arbitrary energy bands, while *Yohkoh* provided images with four fixed energy bands (14-23, 23-33, 33-53, and 53-93 keV). They investigated the time- and energy-dependence of the asymmetry of the intensity of the double-footpoint HXR sources and showed that the asymmetry varies with time and energy. In particular, they found that the asymmetry is inverted with energy: the brighter HXR source for the lower energy and that for the higher energy is opposite. This result does not match the Sakao's scenario. The intensity of the footpoint HXR source is proportional to the number of precipitating electrons that is determined from the loss cone. Since the loss cone is independent of the electron energy, it is expected in his scenario that the HXR source at the footpoint with weaker magnetic field is brighter at any energy. One of the possible explanations on the observation by Alexander & Metcalf (2002) is that the pitch-angle distribution of parent electrons is different with energy when they are injected into the loop. The asymmetry of footpoint HXR sources and its variation would be a clue for the determination of the pitch-angle distribution of injected electrons.

In this chapter we analyze the spatial distribution of the non-thermal emissions during the early impulsive phase (01:00:00 - 01:02:00 UT) of the 2003 May 29 flare. We find that three HXR sources appear in this period, similar to the *TRACE* WL image at 01:00:01 UT (left image of Fig. 4.1). These HXR sources show systematic time- and energy-dependent distribution. We interpret the observations as an evidence that the parent electrons are accelerated parallel to the magnetic field line. To verify this hypothesis, we study an acceleration model by using the electron continuity equation in energy and pitch-angle space.

4.2 Observations

The overall observation summary of the 2003 May 29 flare is presented in chapter 2. In this chapter we study the temporal and spectral variations of the HXR and microwave images in 01:00:00 - 01:02:00 UT. The non-thermal light curves in this period is shown in Figure 4.2.

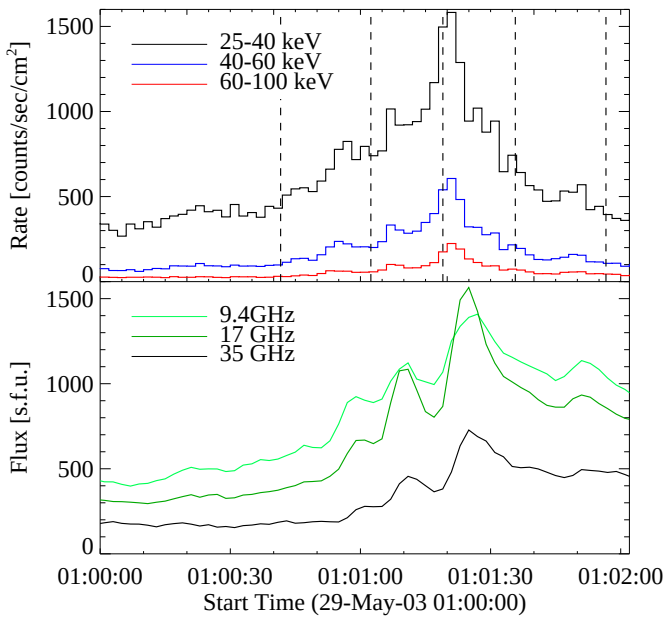

Figure 4.2: Light curves during the early impulsive phase of the 2003 May 29 flare. *Upper*: The *RHESSI* HXR light curves (in units of counts/sec/cm^2) in 25-40, 40-60, and 60-100 keV from top to bottom. The dashed lines denote time intervals for imaging and spectral analysis in § 4.2.1. *Lower*: The microwave light curves (S.F.U.) observed in the NoRP 9.4, 17 and 35 GHz bands from top to bottom.

4.2.1 HXR Images

Figure 4.3 shows the spatial distribution of the HXR emissions taken with *RHESSI* in four energy bands (20-30, 30-40, 40-50, and 50-100 keV from left to right) at four time intervals (01:00:42 - 01:01:02 - 01:01:19 - 01:01:36 - 01:01:56 UT from top to bottom). These time intervals are denoted by the dashed lines in Figure 4.2. These *RHESSI* images are reconstructed with the CLEAN algorithm (Hurford et al., 2002) with collimators 3-6, giving an angular resolution of $\sim 7''$. The background color images are the 1700 Å negative image taken with *TRACE* at 00:59:57 UT (slightly earlier than the times of *RHESSI* images).

The HXR images show time- and energy-dependent distribution. At 01:00:42 - 01:01:19 UT (we will refer to this period as the "rise phase"), three HXR sources can be found in the top two rows of Figure 4.3. For example, the 30-40 keV HXR image at

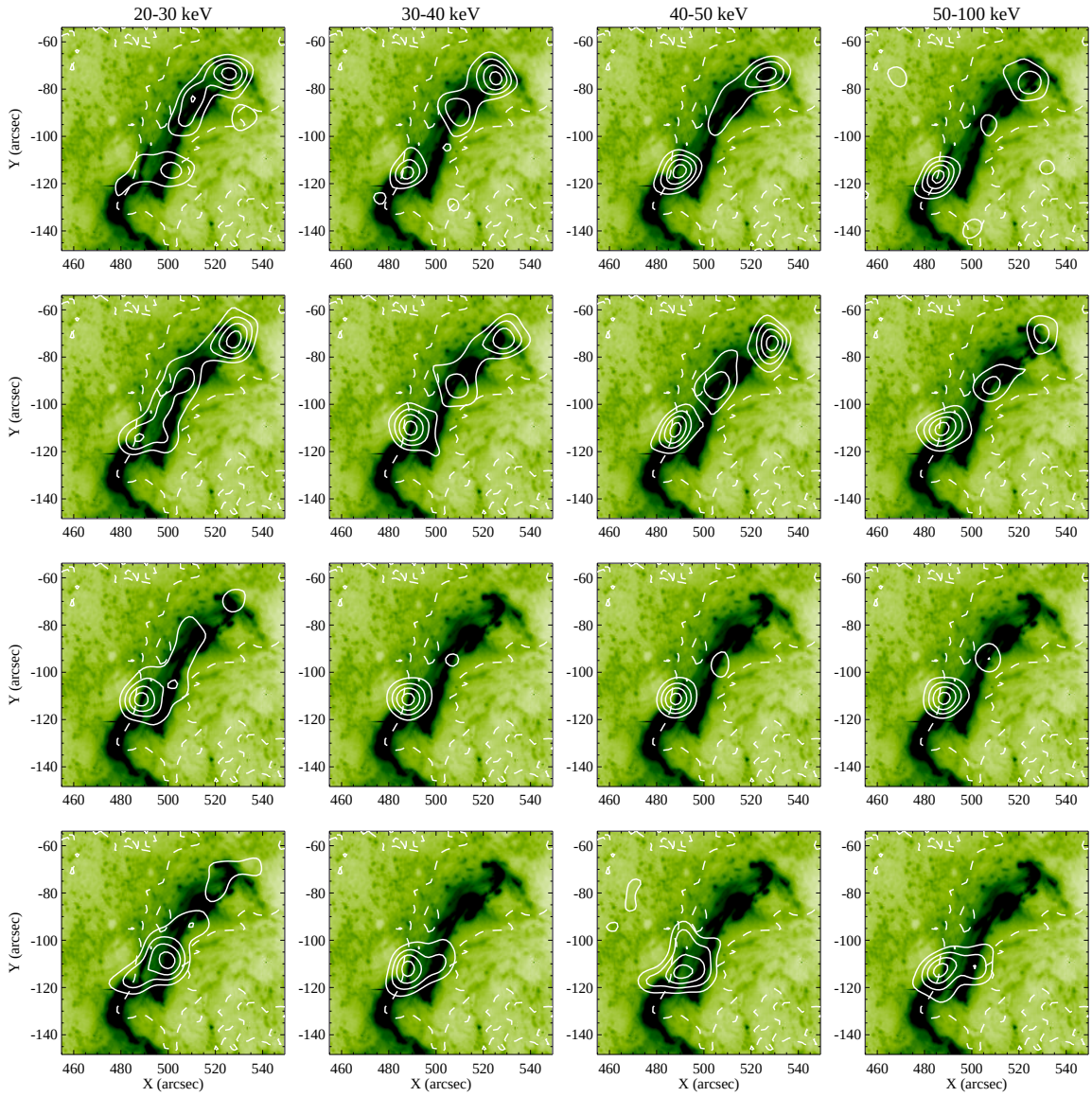

Figure 4.3: *RHESSI* images (solid contours) in 20-30, 30-40, 40-50, and 50-100 keV (from left to right) at 01:00:42 - 01:01:02, 01:01:02 - 01:01:19, 01:01:19 - 01:01:36, and 01:01:36 - 01:01:56 UT (from top to bottom). Contour levels are 30%, 50%, 70%, and 90% of the peak intensity in each image. The *RHESSI* images are reconstructed with the CLEAN algorithm. The background color images are the 1700 Å negative image taken with *TRACE* at 00:59:57 UT. The dashed contours denote the photospheric magnetic neutral lines. Solar north is up and west is to the right.

01:00:42 - 01:01:02 UT (first row, second column) shows the discrete sources around [490,-110], [510,-90], and [525,-75]. We refer to these sources as "SE", "W", and "NW", respectively. Such spatial distribution could not be seen during the impulsive phase of 01:02:00 - 01:05:30 UT, showing double-footpoint sources (see, Fig. 3.2 in chapter 3). Though the SE source seems to be located on the photospheric magnetic neutral line, we consider that the SE source has an opposite (positive) magnetic polarity to the west side (negative), and then the SE source is magnetically connected with the W and NW sources. This speculation is supported by the following reasons: (1) the flare site $x = 500$ is not close to the disk center. Then the projection effect of the photospheric magnetic field is not negligible; (2) the post flare loop seen in EUV (top right map of Fig. 2.2) is tilted with respect to the line of sight; and (3) the UV image (bottom right map of Fig. 2.2) shows the structure connecting the southeast site and the northwest site.

These HXR sources are within the ribbons seen in 1700 Å UV. From Figure 4.1, we confirm that the sites of them are almost co-spatial with the emission sites of the white light. Therefore they are emitted near the footpoints of the loops by the non-thermal electrons precipitating into the chromosphere. We further confirm this assertion from the spectral analysis. Figure 4.4 shows the HXR energy spectra at four time intervals, correspond to those for images. The black lines are the observational data. We fit the *RHESSI* 6-100 keV spectrum with a combination of a single Maxwellian (represents the thermal bremsstrahlung, see, e.g., Tandberg-Hanssen & Emslie (1988)) with involving two gaussians for the iron-line complex peaking at ~ 6.7 keV and the iron-nickel complex peaking at ~ 8.0 keV, and a single power-law (represents the non-thermal bremsstrahlung) functions. The green and red lines are the fitted Maxwellian and power-law functions, respectively. In the rise phase (top), the mean temperature obtained from the fitting by the Maxwellian function is ~ 1.4 keV. By the thermal bremsstrahlung radiation mechanism, this value is related to be the plasma average temperature. The emissions above 20 keV are well described by the power-law with the spectral indices of 4.4 - 4.9, supporting that these are certainly non-thermal emissions. Therefore all of the > 20 keV HXR sources in the rise phase are the emissions from the non-thermal electrons precipitating into the footpoints of the loops.

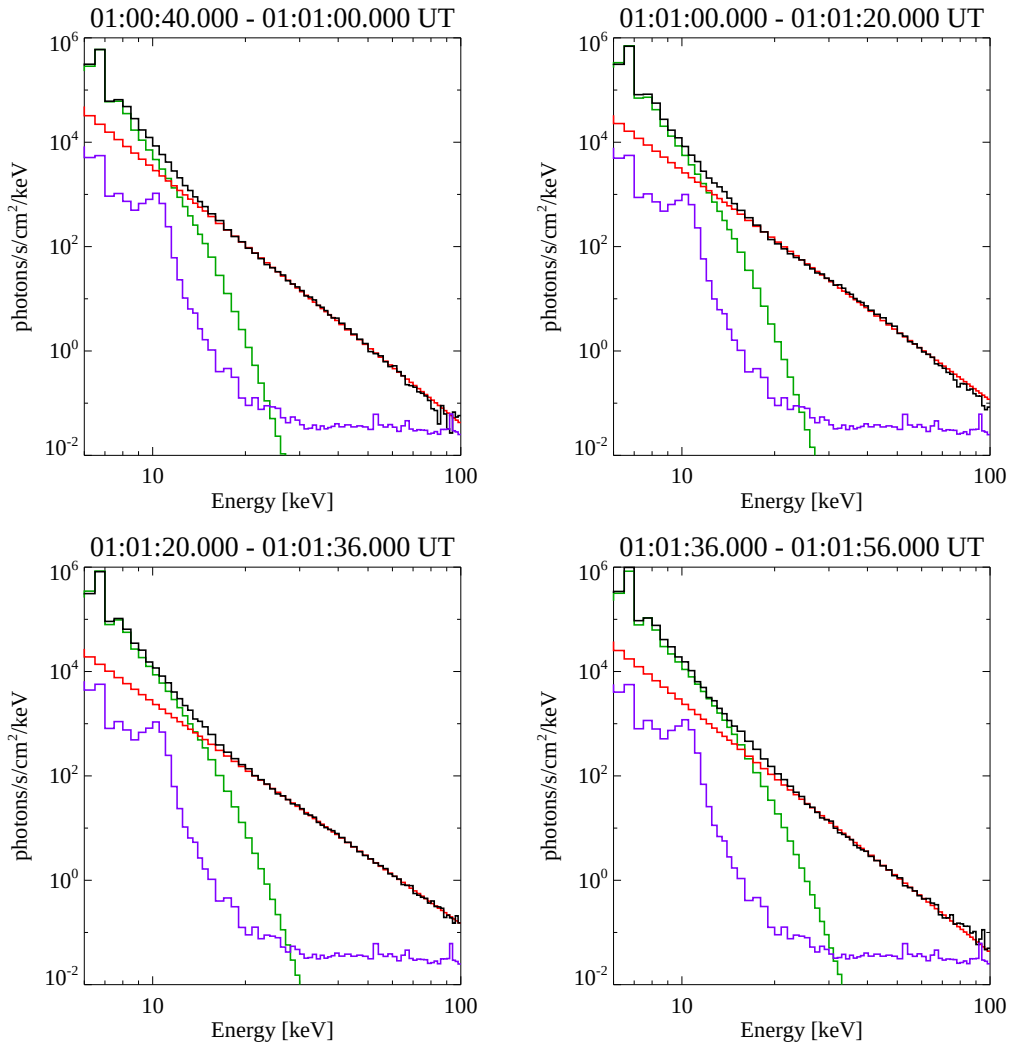

Figure 4.4: Energy spectra of the spatially integrated HXR photon flux taken with *RHESSI* at 01:00:40 - 01:01:00 (top left), 01:01:00 - 01:01:20 (top right), 01:01:20 - 01:01:36 (bottom left), and 01:01:36 - 01:01:56 (bottom right) UT. The black, green, red, and purple lines are the observational data, the fitted single Maxwellian distribution (represents the thermal bremsstrahlung) with involving two gaussians for the iron- and iron-nickel lines, the fitted single power-law distribution (represents the non-thermal bremsstrahlung), and the background level, respectively. From the fitting, the mean temperature (in units of keV) and the spectral index in the power-law part at each interval are obtained to be $\{1.37 \pm 0.043, 4.9 \pm 0.02\}$, $\{1.38 \pm 0.039, 4.4 \pm 0.02\}$, $\{1.60 \pm 0.0002, 4.2 \pm 0.0004\}$, and $\{1.84 \pm 0.0001, 4.8 \pm 0.0005\}$.

At 01:01:19 - 01:01:56 UT (we will refer to this period as the "decay phase"), the SE source becomes prominent. The NW source disappears at 01:01:19 - 01:01:36 UT (third row of Fig. 4.3), and the W source disappears at 01:01:36 - 01:01:56 UT (fourth row). Finally, the HXR sources are located at the region of $[480 < x < 500]$ and $[-120 < y < -100]$, except those in 20-30 keV (bottom left). The HXR energy spectra in the decay phase are shown in the bottom plots of Figure 4.4. With the flare progress, the mean temperature gradually increases and achieves 1.8 keV at 01:01:36 - 01:01:56 UT (bottom right). In this period, the emissions around 20 keV are expressed by both the thermal and non-thermal, while the emissions above ~ 30 keV are described by the power-law with the spectral indices of 4.2 - 4.8. Therefore the > 30 keV HXR sources in this phase (fourth row of Fig. 4.3) are also the non-thermal emissions. We consider these as the double-footpoint HXR sources, which are too close to be well resolved. They are connected (by the magnetic loop) almost perpendicular to the magnetic neutral line. Such spatial distribution of the HXR sources is similar to that observed during 01:02:00 - 01:05:30 UT (Fig. 3.2). These HXR images in the rise and decay phases reveal that the flare morphology changed with time during the early impulsive phase.

We discuss the energy-dependent difference of the HXR images in the rise phase. Three HXR sources are commonly seen in all energy bands (20-100 keV). However, the ratio of the HXR intensity at the east side to that at the west side shows a systematic asymmetry with energy. In the lower energy (20-40 keV), the HXR emissions primarily come from the west side (e.g., image at the second row, first column of Fig. 4.3). In the higher energy (50-100 keV), on the other hand, the HXR emissions are concentrated at the SE site.

Imaging Spectroscopy

For a quantitative analysis, we newly reconstruct the HXR images with the Forward-Fitting algorithm (Aschwanden et al., 2002). This algorithm describes the spatial distribution of emissions by a finite number of elementary analytic functions (e.g., gaussian function). We reconstruct the HXR images in the rise phase (01:00:42 - 01:01:19 UT) by using this algorithm with five number of gaussian functions, which is overlaid on the *SOHO*/MDI magnetogram in Figure 4.5. We can more clearly

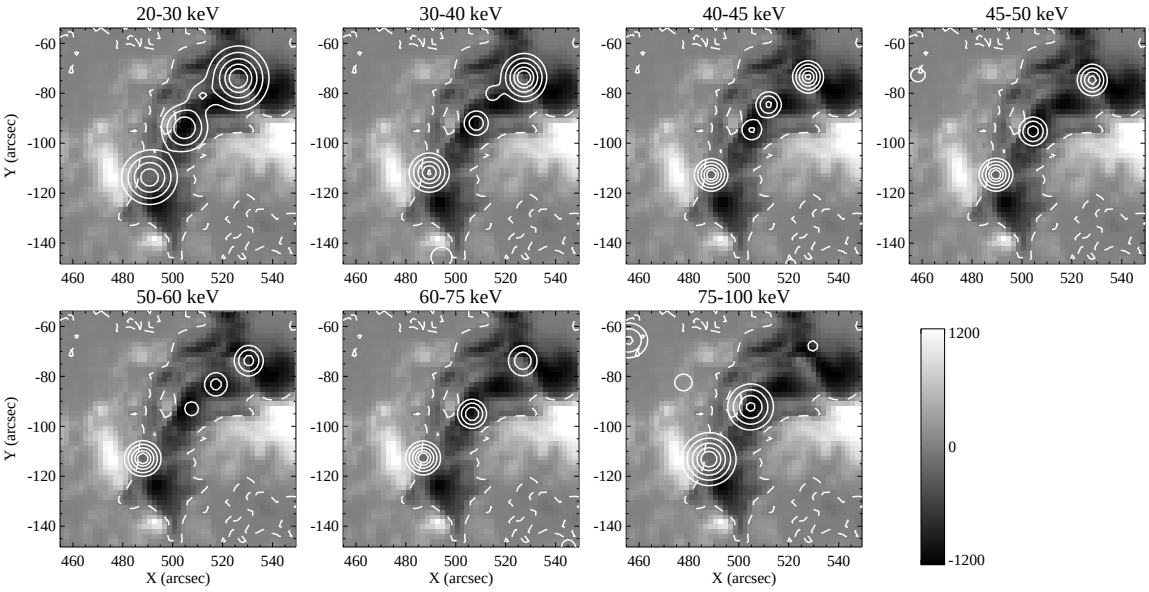

Figure 4.5: *RHESSI* images (solid contours) at 01:00:42 - 01:01:19 UT, in energy bands of 20-30, 30-40, 40-45, 45-50, 50-60, 60-75, and 75-100 keV from top left to bottom right. These images are reconstructed with the Forward-Fitting algorithm. Contour levels are 15%, 30%, 50%, 70%, and 85% of the peak intensity in each image. The background images are the *SOHO*/MDI magnetogram. The dashed contours denote the photospheric magnetic neutral lines. Solar north is up and west is to the right.

discriminate the three sources of SE, W, and NW in these images than the CLEAN images. The W and NW sources are located at the region with strong negative magnetic polarity (~ -1000 Gauss). The SE source is, as found earlier, located on the photospheric magnetic neutral line. We consider that the SE source is located at the region with weak positive magnetic polarity and is a conjugate of the NW as well as W sources.

The center positions of the sources are slightly different from each image with different energy band. In two images in 40-45 and 50-60 keV, the W source is split into two sources. We consider that these uncertainties are within an error of the image reconstruction because no systematic variation is found when we reconstruct images with different parameter set (time intervals and energy bands).

The HXR intensity of the NW source is larger than that of the SE and W sources for the lower energy but smaller for the higher energy. In the 75-100 keV, the NW source is quite faint and the emissions primarily come from the SE and W sources.

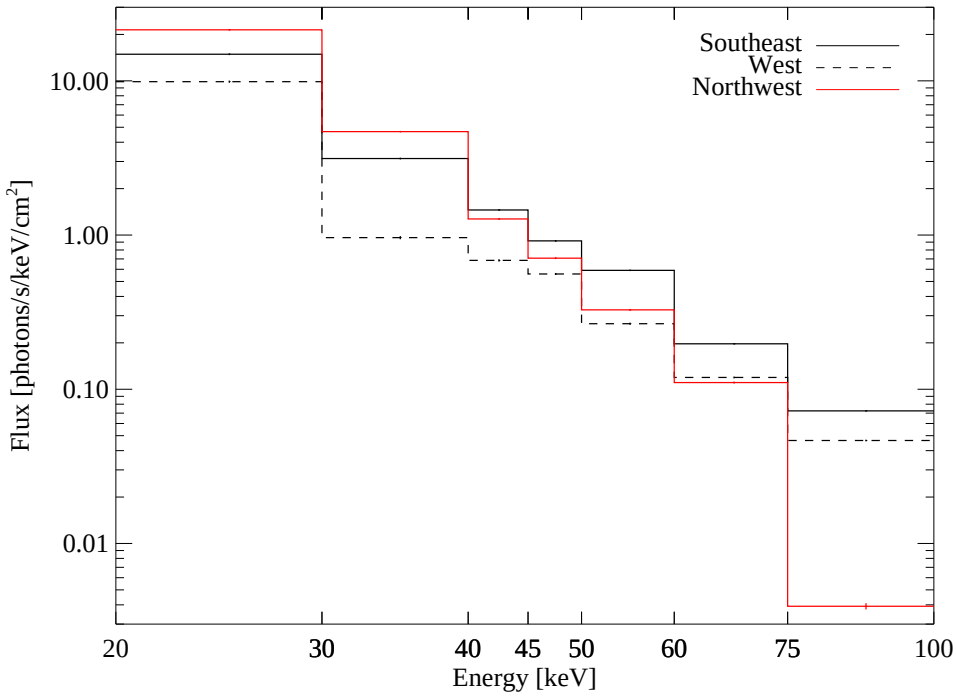

Figure 4.6: Energy spectra of the HXR photon fluxes from the southeast footpoint (SE; black solid line), west footpoint (W; dashed line) and the northwest footpoint (NW; red line) in the rise phase, obtained from Fig. 4.5.

Using these images, we compare the energy spectra of the HXR photon fluxes from the SE, W, and NW sources. Figure 4.6 shows the energy spectra of the HXRs from three sources. The emission from the W source (dashed line) is smaller than that from the SE source (black solid line) in all energy bands. This relationship can be explained by the Sakao's scenario because the magnetic field at the W source is stronger than that at the SE source. From the single power-law fitting, we obtain the spectral indices of the emissions from the W and SE sources, 4.4 ± 0.42 and 4.1 ± 0.36, respectively. Since the spectral indices of the spatially integrated HXR photon flux in this phase are 4.4 - 4.9 (top plots of Fig. 4.4), these spectral indices of the W and SE sources are in the reasonable range. The emission from the NW source is larger than that from the SE source for the lower energy (< 40 keV), but much smaller for the higher energy (> 50 keV). This clearly shows the systematic asymmetry of the HXR intensity from the double footpoints with energy, same as that reported by Alexander & Metcalf

(2002). This relationship can not be explained by the Sakao's scenario. The spectral index of the emission from the NW source is 5.0 ± 0.80, also in the reasonable range. This result indicates that the lower energy electrons preferably precipitate into the NW footpoint with stronger magnetic field while the higher energy electrons are into the SE footpoint with weaker magnetic field.

4.2.2 Microwave Images

The time resolution for the *RHESSI* image reconstruction depends on the photon count. The photon count in the rise phase was not large enough to allow us to reconstruct images with high time and energy resolutions. For further study, we use the NoRH microwave images. Since NoRH provides the high time resolution data (up to 100 ms), these are complement to the spectrally-resolved *RHESSI* images (Fig. 4.5).

The top maps of Figure 4.7 show the spatial distribution of the microwave brightness temperature (drawn in a logarithmic scale) at 01:01:11 UT, taken with NoRH in two frequency bands of 17 GHz (left) and 34 GHz (right). We made the NoRH images with a integration time of 2 s. The *RHESSI* 30-40 keV HXR image (same as that in Fig. 4.5) is overlaid as the black solid contours. The bottom left map shows the spatial distribution of the microwave spectrum, which is defined by

$$\alpha = \frac{\log\left(F_\nu^{34\mathrm{GHz}}/F_\nu^{17\mathrm{GHz}}\right)}{\log(34\ \mathrm{GHz}/17\ \mathrm{GHz})}, \tag{4.2.1}$$

where F_ν is the flux density. Note that by this definition the sign of α is opposite to that defined in § 3.2.3. To obtain this image we convolve the 17 GHz image with the 34 GHz beam pattern and vice versa, because two images with different observation frequencies have different beam patterns (see § 2.3.2). When α is negative, the emission is optically-thin and thus α can be related to the energy distribution of the parent electrons.

The microwave emissions primarily come from the site between the HXR SE and W sources. Therefore we consider the flare main energy release site (main site) is located near the loop which connects the SE and W sources. Since the maximum brightness temperature at 17 GHz, 9×10^7 K, is too intense to be explained by the thermal free-free emission (e.g., Dulk, 1985), these emissions are non-thermal

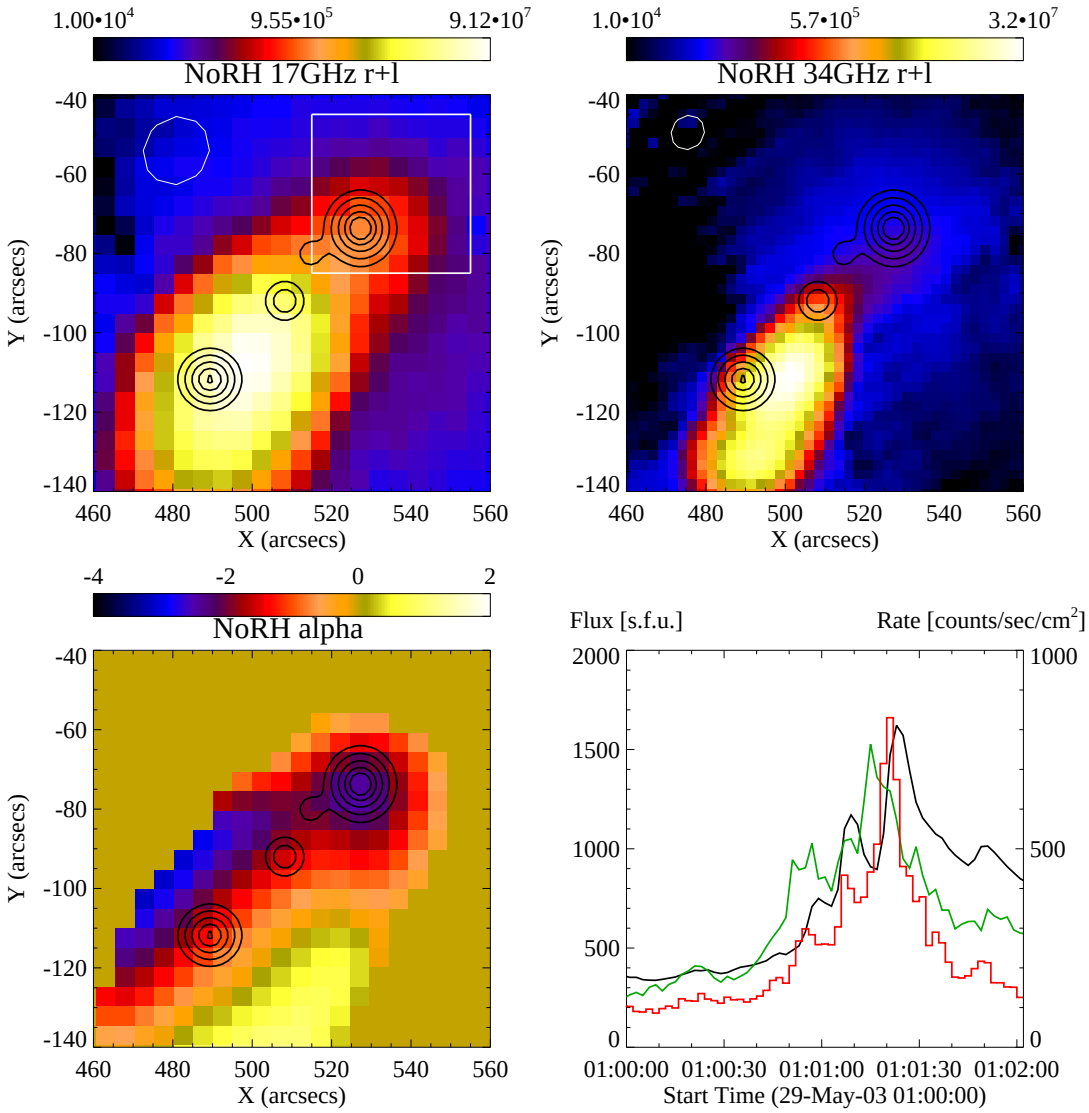

Figure 4.7: Microwave observation during the early impulsive phase. *Top*: NoRH 17 GHz (left) and 34 GHz (right) brightness temperature (in units of kelvin, logarithmic scale) maps at 01:01:11 UT. Solar north is up and west is to the right. The black solid contours show the *RHESSI* 30-40 keV image at 01:00:42 - 01:01:19 UT. White circles in the upper left corner denote the beam size at half-level of the peak intensity. The 17 GHz microwave footpoint source region is defined by a white box in the left map. *Bottom left*: Map of microwave spectral index α derived from eq. (4.2.1). *Bottom right*: Light curves of the 17 GHz microwave footpoint emission (green, S.F.U.), the 17 GHz total microwave (black), and the 40-100 keV HXR (red, in units of counts/sec/cm^2). The value of the 17 GHz microwave footpoint flux density is multiplied by a factor of 60 for illustration.

gyrosynchrotron radiation from the high energy electrons trapped in this loop (Kundu et al., 1994; Melnikov et al., 2002).

In addition, we observe the microwave counterpart of the HXR NW source. We consider it as the microwave footpoint source. This is only seen in the 17 GHz image (top left map); no significant signal is detected in the 34 GHz image (top right) during the course of the early impulsive phase. From the spectrum map (bottom left), the microwave footpoint emission has a softer spectral index ($\alpha \sim -4$) than that at the main site (~ -2), indicating that the energy distribution of the parent electrons at the microwave footpoint source is softer than that at the main site. Note that the magnetic field strength at this site is ~ -1000 Gauss (Fig. 4.5). When the magnetic field strength at the emission site is larger, the effective energy of electrons emitting gyrosynchrotron radiation at a fixed frequency is lower (e.g., Lu & Petrosian, 1989; Bastian, 1999). We estimate the effective energy of the electrons contributing to the microwave footpoint emission according to an approximation by Lu & Petrosian (1989),

$$E_{\rm eff} = 9.0 \left(\frac{\nu}{17\ {\rm GHz}}\right)^{1/2} \left[\left(\frac{B}{100\ {\rm Gauss}}\right) \delta \sin\theta\right]^{-1/2} - 1, \tag{4.2.2}$$

where δ is the index of the energy distribution (single power-law assumption) of parent electrons, θ is a viewing angle with respect to the magnetic field line, and $E_{\rm eff}$ is the kinetic energy in units of the electron rest mass energy, respectively. The spectral index of the parent electrons at the microwave footpoint source can be evaluated from the observed microwave spectral index (~ -4) with an empirical relationship given by Dulk (1985) (see also § 3.4.2), yielding $\delta = -1.1(\alpha - 1.2) \sim 5.8$. Using this, we estimate $E_{\rm eff} = 200$ keV if we assume $B = 1000$ Gauss and $\theta = 45°$. Consequently, we consider that the microwave footpoint emission is generated by the lower energy ($\lesssim 200$ keV) electrons with a softer energy distribution, compared to those at the main site. This picture is qualitatively consistent with the relationship between the HXR NW and SE sources.

The white box in the top left map of Figure 4.7 denotes the microwave footpoint region defined by eye. Using a time series of 17 GHz NoRH images, we obtain the light curve of the microwave footpoint emission by integrating the flux density in this region. The bottom right plot of Figure 4.7 shows the light curve of the microwave

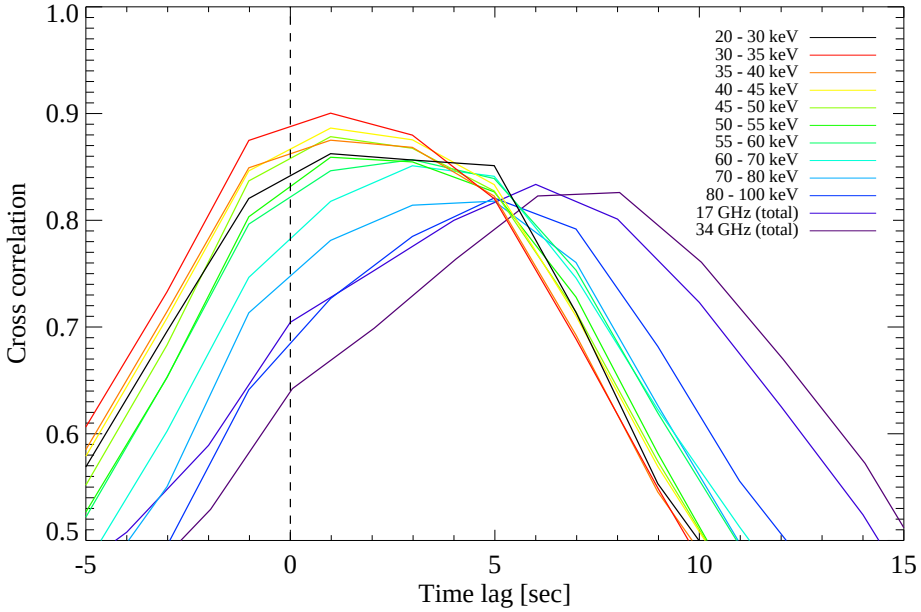

Figure 4.8: Cross-correlation functions of the light curves in 01:00:30 - 01:01:30 UT, between the 17 GHz microwave footpoint emission and the emissions in many other frequency bands. The lower energy HXRs coincide with the 17 GHz microwave footpoint emission (red and yellow lines), while the higher energy HXRs and microwaves are delayed (green and blue lines).

footpoint source (green line). The light curves of the 17 GHz total microwave (black line) and the 40-100 keV HXR (red line) are also shown for comparison. These three light curves show similar profile of two sub peaks and the main peak, indicating that these are emitted by the electrons from the same population. However, they show time lags. Two sub peaks are simultaneous between the microwave footpoint and the HXR light curves. The main peak of the microwave footpoint leads that of the HXR. The total microwave light curve is delayed from both the microwave footpoint and the HXR at all peaks. We calculate the cross-correlation functions of the light curves in 01:00:30 - 01:01:30 UT between the microwave footpoint emission and emissions in many other frequency bands. This is presented in Figure 4.8. The 17 GHz and 34 GHz total microwave emissions are delayed from the footpoint emission by 8-10 s (e.g., blue lines). The lower energy HXRs coincide with the microwave footpoint emission within a time resolution of 2 s (e.g., red line), but are systematically delayed

with increasing energy. Though these HXR light curves are spatially unresolved ones, we guess from Figures 4.3 and 4.5 that the lower energy HXR light curve corresponds to the emissions from both the NW and SE sources while the higher energy one corresponds to the emission from the SE source. Therefore this result shows that the northwest footpoint source brightens earlier than other sources around the main site, though this source is far from the main site. This implies that the parent electrons preferably travel toward the northwest from the main site.

4.2.3 Observation Summary and Discussion

In the rise phase of the early impulsive phase, three footpoint HXR sources, SE, W, and NW, were observed with *RHESSI*. The SE and W sources are conjugate footpoints of the loop at the flare main site where the primal energy release and particle acceleration took place, supported by the NoRH images. We consider that the electrons are injected into the loops around there. The additional NW source is also a conjugate with the SE source. Though the magnetic field at the NW site is stronger than that at the SE site, the HXR emission from the NW source is brighter for the lower energy than that from the SE source. This asymmetry of the HXR intensity is inverted for the higher energy. We found that the lower energy emissions from the NW source lead the higher energy emissions at the main site (including the SE source).

As is shown by *RHESSI* and *TRACE* (Fig. 4.1), the flare morphology and its magnetic field configuration in the early impulsive phase are quite different from those in the main impulsive phase. We discuss a possible scenario for the evolution of this flare. Before the flare, *TRACE* 195 Å image shows a dark structure lying southeast ([480, −120]) to northwest ([520, −80]) sites (top left panel of Fig. 2.2). This is a filament, sustained by sheared and twisted fields. At the beginning of the flare reconnection occurred in these fields, suggested by the *RHESSI* images shown in this chapter. The filament lost equilibrium, and then was ejected upward. Pre-existing closed dipole fields, which envelop the filament and the sheared fields, were elongated by the ejected filament. The elongated dipole fields create current sheet. Consequently the two-dimensional CSHKP type magnetic reconnection (Fig. 1.2) took place, as observed in the main impulsive phase. Such scenario is proposed by

Hirayama (1974) and Moore et al. (2001). Though we do not detect the filament motion from the *TRACE* 195 Å movie due to a lack of the observation during 00:56 - 01:01 UT (corresponds to the flare onset), there are indirect evidences of the filament ejection: (1) the filament disappeared in the *TRACE* image taken several hours after the flare; and (2) the CME and the type II radio burst were observed by *SOHO*/LASCO and the WIND satellite, respectively.

The energy-dependent asymmetry of the HXR intensity between the SE and NW sources can not be explained by the Sakao's scenario, while the asymmetry between the SE and W sources is well understood. In his scenario, the HXR source at the footpoint with weaker magnetic field must be brighter at any energy than that with stronger magnetic field, as long as the parent electrons are "symmetrically" injected into the loop: electron injection at an apex of the loop with a symmetric pitch-angle distribution with respect to the direction parallel to the magnetic field line.

Falewicz & Siarkowski (2007) considered an asymmetry of the injection site to explain the brighter HXR source at the footpoint with stronger magnetic field. When the injection site is close to the footpoint with stronger magnetic field, electrons which can not precipitate into this footpoint take a long distance to reach another footpoint with weaker magnetic field. During this journey, they suffer considerable Coulomb collisions and then lose their energy. Therefore, this scenario predicts a lack of lower energy emissions at the footpoint with weaker magnetic field because lower energy electrons might stop before reaching this footpoint. As a result, the energy-dependent asymmetry of the footpoint HXR sources that is brighter at the site with stronger (weaker) magnetic field for the lower (higher) energy might be realized. Their scenario is, however, not adequate for our observation. The injection site must be situated close to the NW source to be explained in viewpoint of their scenario. In our situation, the flare main energy release site is located between the HXR SE and W sources (Fig. 4.7), indicating that the injection site is also located around there, rather far from the NW source.

Hanaoka (1999) presented microwave observations of flares that show the microwave footpoint source located at a remote distance from a flare main site. The light curve of the microwave footpoint source is slightly delayed from that of the HXR at the main site. This is opposite to our observation, but their observation is

rather straightforward to be understood. If electrons are injected symmetrically with respect to the magnetic field line, the emission at the site far from the main site must be delayed from that at the main site because parent electrons require longer time to reach there.

Previous scenarios, which could not explain our observation, implicitly assumed that the injected electrons have a symmetric pitch-angle distribution with respect to the direction parallel to the magnetic field line. We conclude that the characteristics of the northwest footpoint emission are hard to be explained as long as assuming the symmetric pitch-angle distribution of the injected electrons. The trap-plus-precipitation model studied in chapter 3 is also not adequate for describing the northwest footpoint emission. One possible explanation for the relationship between the NW and SE sources is the parallel asymmetry of the pitch-angle distribution of the injected electrons.

4.3 A Model for Electron Acceleration

We make a hypothesis that the electrons which emit HXRs and microwaves at the NW and SE sources suffered a parallel acceleration toward the northwest direction. To verify this, we model an acceleration parallel to the magnetic field line by using the electron continuity equation. The continuity equation is useful for analytically describing the evolution of the electron energy distribution (e.g., Tsuneta, 1995).

To study this, we make simplifications as follows:

1. Electrons are already pre-accelerated/heated before entering the "acceleration site".

2. They are further accelerated by an unspecified external force at the site without escape.

3. After the acceleration ceases, they are injected into the loop, start to propagate, and then precipitate into the footpoints with different magnetic field strengths.

By treating the pre-accelerated electrons as an initial condition, we study the evolution of the electron distribution in phase space during the periods 2 - 3.

4.3.1 Continuity Equation

We model the evolution of electrons at the acceleration site by using the electron continuity equation in energy and pitch-angle space,

$$\frac{\partial N}{\partial t} + \frac{\partial}{\partial E}\left(\dot{E}N\right) + \frac{\partial}{\partial \mu}\left(\dot{\mu}N\right) = 0. \tag{4.3.1}$$

Here $N(\mu, E, t)$ is the electron distribution in phase space (number of electrons per unit pitch-angle cosine per unit energy), $\dot{E}$ and $\dot{\mu}$ are the electron energy and pitch-angle change by an external force, μ is the pitch-angle cosine, $E = \Gamma - 1$ is the kinetic energy in units of the electron rest mass energy $m_{\rm e}c^2$, Γ is the Lorentz factor, $m_{\rm e}$ is the electron mass, and c is the speed of light, respectively. Here we do not consider the energy loss by Coulomb collisions for simplicity.

Electrons change their energy and pitch angle by an external force,

$$\frac{dE'}{dt'} = \dot{E}(\mu', E') = \mu'\beta(E')\frac{F_\parallel}{m_{\rm e}c}, \tag{4.3.2}$$

$$\frac{d\mu'}{dt'} = \dot{\mu}(\mu', E') = \frac{1-\mu'^2}{\Gamma'\beta(E')}\frac{F_\parallel}{m_{\rm e}c}, \tag{4.3.3}$$

where $\beta = \sqrt{1-(E+1)^{-2}}$ and $F_\parallel$ is the external force parallel to the magnetic field line. The primed variables are the Lagrangian coordinates of an electron. We assume $F_\parallel = \text{constant} > 0$. We later discuss a possible candidate of this force. The analytic solution of equation (4.3.1) can be obtained by the method of characteristics (Craig et al., 1985),

$$N(\mu, E, t) = N(\mu_0, E_0, 0)\frac{\Gamma^2\beta}{\Gamma_0^2\beta_0}, \tag{4.3.4}$$

where $\Gamma_0 = E_0 + 1$, $\beta_0 = \beta(E_0)$, and (μ_0, E_0) is the solution of equations (4.3.2) and (4.3.3) at $t' = 0$ with a boundary condition of $(\mu', E', t') = (\mu, E, t)$.

We give the initial condition for N (pre-accelerated electrons) as the isotropic kappa distribution,

$$N(\mu, E, 0) = \left(\frac{1}{2\pi\kappa E_{\rm p}}\right)^{3/2}\frac{\mathcal{G}(\kappa+1)}{\mathcal{G}(\kappa-1/2)}\frac{\beta}{\Gamma^3}\left(1+\frac{E}{\kappa E_{\rm p}}\right)^{-(\kappa+1)}. \tag{4.3.5}$$

Here,

$$E_{\rm p} = \frac{k_{\rm B}T}{m_{\rm e}c^2}\left(1-\frac{3}{2\kappa}\right), \tag{4.3.6}$$

is related to the average thermal energy, $k_{\rm B}$ is the Boltzmann constant, T is the temperature, and $\mathcal{G}(x)$ is the gamma function, respectively. For $\kappa \gg 1$ this distribution is identical to a simple Maxwellian with the temperature T. For smaller $\kappa > 1$ this distribution possesses a power-law tail at high energy. We take $k_{\rm B}T = 1.5$ keV and $\kappa = 4$.

4.3.2 Electron Distributions

Figure 4.9 shows the electron distribution in phase space (μ, E) at the acceleration site (eq. (4.3.4)). The external force is taken to satisfy $F_{\parallel}ct = 80$ keV, i.e.,

$$F_{\parallel} = 2.7 \times 10^{-3} \left(\frac{t}{0.1 \text{ s}} \right)^{-1} \text{[eV/m]}. \tag{4.3.7}$$

Since the equation (4.3.1) is the advection equation, its solution is determined when $F_{\parallel}t$ is determined. Electrons with initially isotropic pitch-angle distribution move toward the positive direction in μ space and then the resulting distribution peaks at μ close to unity, because the external force is given as positive. The lower energy electrons are more concentrated in the parallel direction than the higher energy ones, as seen from contours.

We assumed that after the acceleration ceases electrons start to propagate toward both footpoints of the loop. These electrons propagate in the loop (with a length of $\sim 6 \times 10^4$ km) within a second, while the observation timescale is longer. Therefore we do not consider the time evolution of the electron distribution along the loop but simply evaluate the electron distribution at both footpoints as follows. The footpoint (FP1) is located at the end of the positive direction ($\mu > 0$) with stronger magnetic field, representing the NW source. We assume that this footpoint has a mirror ratio $M_1 = 5$ and thus a loss cone angle cosine $\mu_{c1} = \sqrt{1 - M_1^{-1}} = 0.9$. Therefore the electron flux precipitating into FP1 can be evaluated as

$$f_1(E, t) \propto \beta \int_{\mu_{c1}}^{1} \mu N(\mu, E, t) d\mu. \tag{4.3.8}$$

The range for integration corresponds to the region surrounded by the vertical axis (at $\mu = 1$) and the solid line in Figure 4.9.

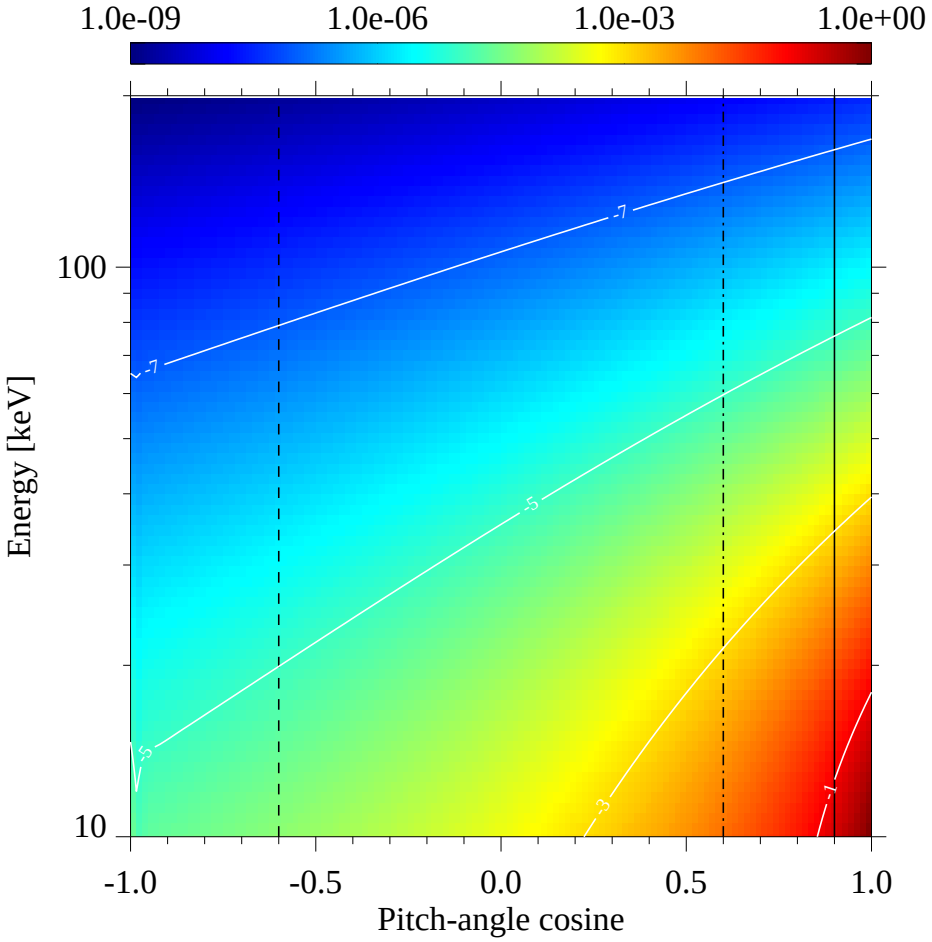

Figure 4.9: Electron distribution in phase space at the acceleration site (eq. (4.3.4)). The horizontal and vertical axes correspond to the electron pitch-angle cosine and energy, respectively. The white lines are contours with levels of 10^{-7}, 10^{-5}, 10^{-3}, and 10^{-1} of the maximum value. The solid, dashed, and dash-dotted lines denote the loss cones, $0.9(= \mu_{c1})$, $-0.6(= -\mu_{c2})$, and $0.6(= \mu_{c2})$, respectively.

Another footpoint (FP2) is located at the end of the negative direction ($\mu < 0$) with weaker magnetic field, representing the SE source. We assume that this footpoint has a mirror ratio $M_2 = 1.56$ and thus a loss cone angle cosine $\mu_{c2} = 0.6$. The electron flux precipitating into FP2 can be evaluated as

$$f_2(E,t) \propto \beta \left[\int_{-1}^{-\mu_{c2}} \mu N(\mu, E, t) d\mu + \int_{\mu_{c2}}^{\mu_{c1}} \mu N(\mu, E, t) d\mu \right]. \tag{4.3.9}$$

The electrons with the pitch-angle cosine of $\mu_{c2} < \mu < \mu_{c1}$ initially travel toward the positive direction. They can not precipitate into FP1 because they are outside the loss cone. Then they bounce at there, change the sign of μ, and travel toward the negative direction. Consequently they precipitate into FP2 (Aschwanden et al., 1999). This corresponds to the second term of equation (4.3.9). The range for integration is shown in Figure 4.9: the region surrounded by the vertical axis (at $\mu = -1$) and the dashed line (for the first term), and that surrounded by the solid and dash-dotted lines (for the second term).

These two quantities are related to the footpoint HXR emissions by adopting the thick-target bremsstrahlung (Brown, 1971) as the emission mechanism. Figure 4.10 shows the energy distribution of the precipitating electron fluxes $f_1(E)$ (solid line) and $f_2(E)$ (dashed line). In the lower energy, the number of $f_1(E)$ is larger than $f_2(E)$. On the other hand, the number of $f_2(E)$ is larger than $f_1(E)$ in the higher energy. From the single power-law fitting of their energy distributions above 30 keV, we obtain the spectral indices of 5.8 for $f_1(E)$ and 5.3 for $f_2(E)$. Such electron fluxes can produce the energy-dependent asymmetric footpoint HXR emission that is brighter at the site with stronger (weaker) magnetic field for the lower (higher) energy. This is consistent with the observed relationship between the NW and SE sources.

This difference in the energy distribution of the precipitating electron fluxes is attributed to that the rate of the electron energy and pitch-angle change depends on the initial condition (μ_0, E_0). This is understood by the analytic solution of equations (4.3.2) and (4.3.3), which describes the time evolution of the energy and pitch-angle

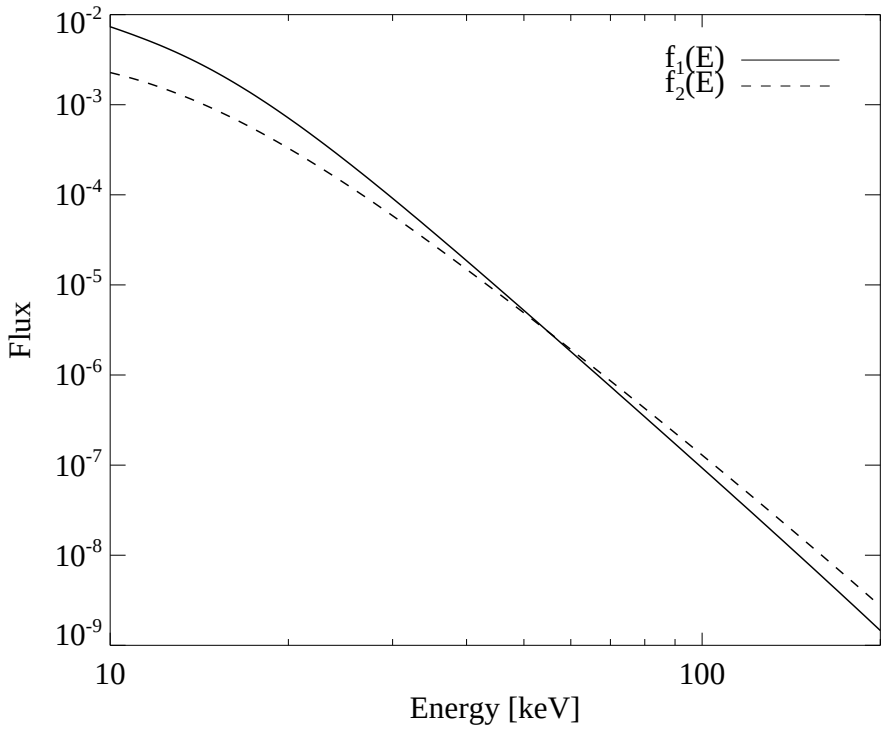

Figure 4.10: Energy distribution of the precipitating electron fluxes, $f_1(E)$ (solid line) and $f_2(E)$ (dashed line). From the single power-law fitting, the spectral indices are obtained to be 5.8 and 5.3, respectively.

of an individual electron. Using the non-relativistic approximation, the solution is

$$E' = E_0 + \mu_0 \sqrt{2E_0} \frac{F_\parallel t}{m_\mathrm{e} c} + \frac{1}{2} \left(\frac{F_\parallel t}{m_\mathrm{e} c} \right)^2 , \tag{4.3.10}$$

$$\mu' = \cos \left[\tan^{-1} \left\{ \sqrt{1-\mu_0^2} \left(\mu_0 + \frac{F_\parallel t}{\sqrt{2E_0} m_\mathrm{e} c} \right)^{-1} \right\} \right] . \tag{4.3.11}$$

From equation (4.3.10), the energy gain relative to the initial value,

$$\frac{E' - E_0}{E_0} = \mu_0 \sqrt{\frac{2}{E_0}} \frac{F_\parallel t}{m_\mathrm{e} c} + \frac{1}{2E_0} \left(\frac{F_\parallel t}{m_\mathrm{e} c} \right)^2 , \tag{4.3.12}$$

is larger when the initial energy is lower. This means that the acceleration with constant $F_\parallel$ softens the electron energy distribution if seed electrons have a negative slope in their energy distribution (e.g., power-law). From equation (4.3.11), one can

find that electrons with lower initial energy are more concentrated in the parallel direction. This means that this acceleration makes an energy-dependent pitch-angle distribution: anisotropy in parallel direction is stronger for lower energy electrons. The lower energy electrons are more likely to precipitate into FP1. Because of these two reasons, a large number of lower energy electrons with a softer energy distribution can precipitate into the footpoint with stronger magnetic field.

After the precipitation into FP1, the remaining electrons with pitch angle larger than the loss cone angle of FP1 but smaller than that of FP2 travel toward negative direction and precipitate into another footpoint FP2 with weaker magnetic field. Since a large number of lower energy electrons are already lost at FP1, the number of precipitating electrons at FP2 is smaller than that at FP1 for the lower energy though the loss cone (integration range in μ) of FP2 is larger than that of FP1. On the other hand, a significant amount of higher energy electrons remain without precipitating into FP1, because the pitch-angle anisotropy of the higher energy electrons is not so strong compared to that of the lower energy ones (Fig. 4.9). Therefore the number of higher energy precipitating electrons at FP2 is larger than that at FP1.

4.4 Conclusion and Discussion

From the model study, we presented that the energy-dependent asymmetry of the double-footpoint HXR sources can be explained in terms of the energy-dependent difference of the pitch-angle distribution of the parent electrons. We interpret the observed characteristics of the NW source as a consequence that the electrons are accelerated parallel to the magnetic field toward the northwest direction when they are injected into the loop.

We studied the parallel acceleration of electrons by a constant force. A candidate of this force is a field-aligned electric field. Electron acceleration in solar flares by a field-aligned electric field has been considered by e.g., Tsuneta (1985, 1995), Holman (1985), and Benka & Holman (1994). Tsuneta (1995) proposed a scenario for the generation of a field-aligned electric field. He considered that a downflow from the reconnection site drives the small-scale time-varying shear flow (vortices) at the loop top where the downflow collides. Vortices would yield non-steady charge separation.

This yields a polarization current perpendicular to the magnetic field line, which is carried by ions. A field-aligned current is generated to close the current circuit. Then a voltage drop is generated along the magnetic field line and accelerates electrons toward the parallel direction. An amplitude of an electric field in his scenario is estimated to be 2.4×10^{-3} V m^{-1}, which is close to equation (4.3.7).

Generation of a field-aligned electric field is studied for auroral particle acceleration. A scenario for a field-aligned electric field generation by kinetic Alfvén waves has been proposed by e.g., Hasegawa (1976). The scenario is as follows. Alfvén waves originate from a polarization current carried by ions. When this current yields charge separation, Alfvén waves propagate perpendicular as well as parallel to magnetic field lines. This is the shear Alfvén mode. Shear Alfvén waves have a finite amplitude of a field-aligned electric field. In the MHD regime this field is negligibly small. However, a non-negligible field-aligned electric field is generated when a perpendicular wavelength is comparable to the ion gyro-radius or the electron inertia length. This is the kinetic Alfvén wave. When the electron thermal speed is much faster than the Alfvén speed, the field-aligned electric field of the kinetic Alfvén wave is evaluated as

$$\mathcal{E}_{\parallel} \sim k_{\parallel} k_{\perp} \rho_{\rm i}^2 \mathcal{E}_{\perp} \sim k_{\parallel} \rho_{\rm i} \frac{\delta v}{c} B_0, \tag{4.4.1}$$

where $\mathcal{E}_{\parallel}$ and $\mathcal{E}_{\perp}$ are the parallel and perpendicular components of the electric field, $k_{\parallel}$ and $k_{\perp}$ are the parallel and perpendicular wavenumbers, $\rho_{\rm i}$ is the ion gyro-radius, δv is the velocity perturbation, and B_0 is the ambient magnetic field strength, respectively. Spectroscopic observations of solar flares have reported the excess line broadening, which could not be explained by the thermal velocity only, at the loop-top region (non-thermal line broadening, e.g., Khan et al., 1995; Alexander et al., 1998). The corresponding velocity, ~ 100 km s^{-1}, might be related to wave perturbations. Using this value, we estimate equation (4.4.1) as

$$\mathcal{E}_{\parallel} \sim 2.8 \times 10^{-3} \left(\frac{\delta v}{100 \text{ km/s}} \right) \left(\frac{\lambda_{\parallel}}{100 \text{ km}} \right)^{-1} \left(\frac{T_{\rm i}}{2 \text{ keV}} \right)^{1/2} \quad [\text{V/m}], \tag{4.4.2}$$

where $\lambda_{\parallel}$ is the parallel wavelength and $T_{\rm i}$ is the ion temperature. The parallel wavelength is not necessarily the spatial scale of ions or electrons, to achieve the value we used in equation (4.3.7).

Essence of these two models for the generation of a field-aligned electric field is same: an ion polarization current causes the electron motion along the field line to

close the current circuit. The resulting field-aligned electric fields are bi-directional and time-varying. Therefore the energy gain would be zero in net, provided that the spatial and time scales of the fields are smaller than those of phenomena (for a solar flare, $\sim 10^4$ km and ~ 10 s). Inhomogeneity of a background plasma is one of keys to diminish this problem. Nakamura (2000) considered a field-aligned electric field of kinetic Alfvén waves in a plasma with an inhomogeneous ambient magnetic field (mirror kinetic Alfvén waves). When the magnetic field is not uniform, electrons are restricted to move toward the direction of stronger magnetic field by the magnetic mirroring force. To close the current circuit, they have to overcome the mirroring force. Therefore a unidirectional electric field is generated to reduce the effect of the mirroring force, and thus can accelerate electrons toward the direction of stronger magnetic field. This is in agreement with our situation. Nakamura (2000) also showed that this field is static, and thus can accelerate electrons continuously.

In the model, we treated that the emission from the NW source is generated by the directly-precipitating electrons propagating from the main site, while that from the SE source is by the electrons which once travel toward the northwest direction, bounce at the NW footpoint, return to the main site, and then precipitate into the SE footpoint. Therefore it is naturally expected in our model that the emission at the SE footpoint is delayed from that at the NW footpoint. This qualitatively supports the observation, but quantitatively not. The expected time lag in the model is a loop-transit time of electrons, $\lesssim 1$ s, while the observation shows longer time lags between the microwave footpoint emission and the emissions at the main site (Fig. 4.8). One of the probable reasons of this discrepancy is that the emission at the main site is generated by the electrons in the loop connecting the SE and W sites as well as those in the loop connecting the SE and NW sites. The electrons in both loops contribute to the HXR emission at the SE footpoint, while we modeled the electrons in the loop connecting the SE and NW sites only. Another reason is a contribution of trap-precipitating electrons in the loop connecting the SE and NW sites. Electrons which are initially outside the loss cones are once trapped in the loop and then subsequently precipitate into the footpoints via pitch-angle scattering. This is studied in chapter 3, but not in this chapter. These electrons are more likely to precipitate into the footpoint with weaker magnetic field, that is, SE, because the

scattering istropizes the electrons. In these regards, our model treatment of the SE source might be incomplete. However, this does not deny the fact that the HXR emission from the NW source (stronger magnetic field) is brighter than that from its conjugate of the SE source (weaker magnetic field) for the lower energy, and thus not contradict our interpretation that the lower energy electrons preferably travel toward the northwest and precipitate into the NW footpoint.

The asymmetry of the footpoint emissions and its variation reflect signatures of the variation of injected electrons in energy, pitch angle, and time. Since HXR-emitting electrons have a timescale of less than a second (propagation timescale), it is important to observe the emission with a time resolution better than 0.1 s to completely resolve their dynamics. Aschwanden et al. (1996a,c,b) performed a time-of-flight analysis to determine the site where electrons are accelerated and start to propagate, by using the HXR light curves taken with *CGRO*/BATSE with a high time resolution of $\lesssim 64$ ms that is enough to resolve the temporal evolution of electrons. The HXR imaging observation with such a high time resolution is also required to further determine the evolution of the electron energy and pitch-angle distribution at the acceleration site. If the HXR images are taken with $\lesssim 0.1$ s, they would reflect the instantaneous properties of precipitating electrons. Using them as a boundary condition of the model, we would describe the time evolution of the electron distribution at the acceleration site.

Chapter 5

Numerical Study of the Non-Thermal Microwave Propagating Feature in the 1999 August 28 Flare

In this chapter we analytically and numerically study the motion of electrons propagating along the magnetic loop, to consider the observation of the propagating feature of the non-thermal microwave source in the 1999 August 28 flare (Yokoyama et al., 2002) and determine the injection pitch-angle distribution. We found that the microwave propagating feature does not correspond to the motion of a specific electron but the motion of an ensemble of electrons with different initial pitch angles. Based on the study, we conclude that the non-thermal electrons in the 1999 August 28 flare are isotropically accelerated and then are injected into the loop.

5.1 Introduction

Since flare non-thermal emissions are signatures of the propagation of accelerated particles in the solar corona, they have key information on the particle transport process. For HXRs, Sakao (1994) analyzed flares with double-footpoint HXR sources observed with *Yohkoh*, and showed that the time variation of the emissions from

double sources coincides with each other within 0.1 s. This indicates that electrons, not ions, propagate along the magnetic loop, reach the footpoints, and then emit HXRs at there. For meter-wavelength radio emissions, the so-called type III radio burst (e.g., Bastian et al., 1998) is thought to be a daughter Langmuir wave, which is excited by electrons propagating from a flare site toward the interplanetary space along the open magnetic field line. For centimeter-wavelength radio emissions, the microwave source located at a remote distance from a flare main site (microwave remote source; Hanaoka, 1996, 1997; Nishio et al., 1997) is interpreted as the precipitation of electrons propagating from the main site where the energy release and particle acceleration take place. Hanaoka (1999) showed that the light curve at the microwave remote source has a similar profile to the HXR light curve at the main site, but is slightly delayed by roughly the loop transit time of electrons. This confirms the above interpretation.

There are a few microwave observations of the direct detection of propagating electrons from a time series of images. Bastian et al. (1994) reported the motion of the 8.4 GHz and 15 GHz microwave sources with a speed of 3,000 km s^{-1}. White et al. (2000) reported the rapid motion of the 0.33 GHz microwave source with a speed of 2.6×10^4 km s^{-1}. The most striking observation was reported by Yokoyama et al. (2002) (hereafter Y2002). They observed the flare occurred on 1999 August 28 by NoRH with 0.1 s cadence (Fig. 5.1). From a time series of NoRH 17 GHz images, they found two different classes of propagating features of non-thermal microwave sources along the loop. One is a slower propagation at a speed of 6×10^3 km s^{-1} (slope A), and the other is a faster propagation at a speed of 9×10^4 km s^{-1} (slope B).

The origin of the slower propagating feature (slope A) is discussed by Stepanov et al. (2007). They interpreted this feature as the propagation of low-frequency whistler waves that can trap the parent electrons by wave-particle interactions at their turbulent front. The phase velocity of low-frequency whistler waves is roughly in agreement with the observation. The origin of the faster propagating feature (slope B) is discussed by Y2002. They interpreted this propagating feature as free-stream of relativistic electrons along the loop. Assuming that the 17 GHz microwave-emitting electrons are almost relativistic ($v \sim c > 9 \times 10^4$ km s^{-1}), they concluded that the

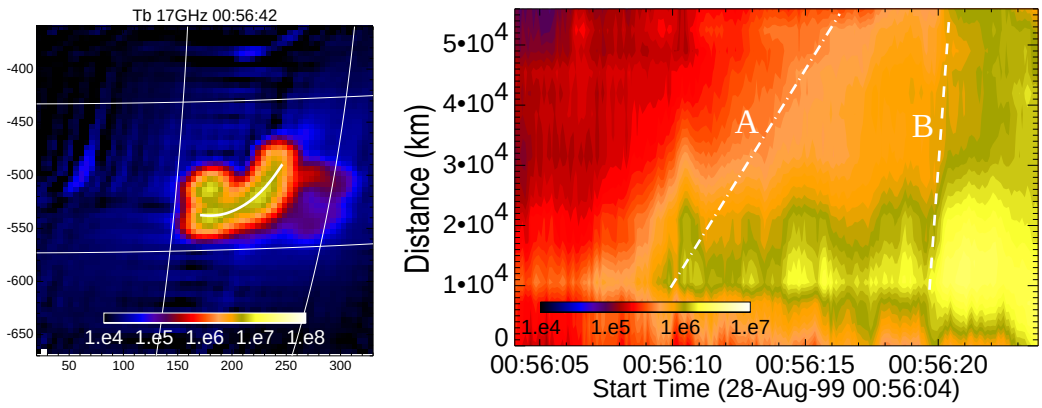

Figure 5.1: Time variation of the 17 GHz intensity distribution along the microwave loop indicated by the solid white line in the left panel. The dash-dotted line A and dashed line B show the propagating feature of the microwave source with speeds of $\sim 6 \times 10^3$ km s^{-1} and $\sim 9 \times 10^4$ km s^{-1}, respectively (from Yokoyama et al., 2002).

parent electrons are injected with large pitch angle, $\sim 70°$.

The interpretation of Y2002 on the microwave propagating feature is subject to the following simplifications. One is on the electron motion. They assumed that electrons freely stream along the loop. However, since the flare loop must be a converging magnetic loop, electrons suffer the magnetic mirroring force. The other is on the microwave emission mechanism. They assumed that the trajectory of electrons corresponds to the apparent motion of the gyrosynchrotron source. However, since the gyrosynchrotron radiation mechanism (Ramaty, 1969; Petrosian, 1981; Dulk, 1985; Bastian, 1999) intricately depends on many physical parameters, it is not necessarily evident that the apparent motion of the radiation source is identical to the trajectory of electrons with a specific pitch angle.

In this chapter we reconsider the rapid propagating feature of the microwave source in the 1999 August 28 flare and address the pitch-angle distribution of the injected electrons, by refining the treatments of the emission mechanism as well as the electron motion in the loop. In § 5.2 we present an analytic treatment of the electron motion in a converging magnetic loop. In § 5.3 we present our numerical model of the electron propagation along the loop. We use the gyro-averaged Fokker-Planck equation (same as in chapter 3) to determine the electron phase space distribution along the loop. We calculate the gyrosynchrotron intensity distribution along the

loop from the calculated electron distribution for comparison with the observation. In § 5.4 we present our calculation results. Our calculation results do not support the interpretation of Y2002 but suggest that the electrons in the 1999 August 28 flare are isotropically accelerated and then are injected into the loop. In § 5.5 we summarize this chapter.

5.2 Analytic Treatment

We show an analytic solution of the motion of a single electron in a converging magnetic loop. This is described by the following equations: the equations of motion along the magnetic field line and the conservation of the magnetic moment,

$$\frac{dr}{dt} = \mu v, \tag{5.2.1}$$

$$\frac{1-\mu^2}{B(r)} = \frac{1-\mu_0^2}{B(0)}, \tag{5.2.2}$$

where r is the position measured from the loop top ($r = 0$; initial position) along the field line, v is the velocity, μ is the pitch-angle cosine, μ_0 is the initial pitch-angle cosine, and $B(r)$ is the magnetic field strength at the position, respectively.

For mathematical convenience, we give the magnetic field strength as a quadratic function with respect to r of the form (e.g., Aschwanden et al., 1996a; Hanaoka, 1999),

$$\begin{aligned} B(r) &= B_0 + (B_\mathrm{f} - B_0)\left(\frac{r}{r_\mathrm{f}}\right)^2 \\ &= B_0\left\{1 + (M-1)\left(\frac{r}{r_\mathrm{f}}\right)^2\right\}, \end{aligned} \tag{5.2.3}$$

where B_0 and B_f are the magnetic field strengths at the loop top and at the footpoint, r_f is the footpoint distance from the loop top along the field line (a half length of the loop), and $M = B_\mathrm{f}/B_0$ is the magnetic mirror ratio, respectively. When its initial pitch angle, $\alpha_0 = \cos^{-1}\mu_0$, is larger than the loss cone angle $\alpha_c = \cos^{-1}(\sqrt{1-M^{-1}})$, an electron is trapped and has the bounce motion in the loop due to the magnetic mirror. With a help of equation (5.2.3), equations (5.2.1) and (5.2.2) describe the

bounce motion as the simple harmonic oscillation,

$$r = R\sin(\omega t), \tag{5.2.4}$$

$$\mu = \mu_0 \cos(\omega t), \tag{5.2.5}$$

where,

$$R = \frac{\mu_0}{\sqrt{(1-\mu_0^2)(M-1)}} r_{\rm f}, \tag{5.2.6}$$

$$\omega = \sqrt{(1-\mu_0^2)(M-1)}\frac{v}{r_{\rm f}}. \tag{5.2.7}$$

Equation (5.2.7) tells that an electron with a larger initial pitch angle has a higher frequency of the bounce motion.

Y2002 interpreted their observation of the rapid propagating feature of the non-thermal microwave source along the flare loop as free-streaming electrons, and estimated their initial pitch angle to be $\sim 70°$. However, the actual flare loop must be a converging magnetic loop that inhibits the electron free-stream. We advance their interpretation by using the solution described above. We assume, same as Y2002, that the apparent propagating motion of the microwave source corresponds to the trajectory of electrons with a specific initial pitch angle. The observation gives constraints on several variables appeared in equations (5.2.6) and (5.2.7). Electrons were injected at the loop-top region around [200,-520] in the left panel of Fig. 5.1 and propagated toward the west loop end around [240,-480]. Then we use a footpoint distance of $r_{\rm f} \sim 4.5 \times 10^4$ km. Electrons took 0.5 sec to reach the footpoint. This time would be smaller than a quarter of the bounce period. Then we evaluated ω as inequality, $\omega \gtrsim (2\pi)/(0.5 \times 4) = \pi$ radian s^{-1}. In the same way, R is evaluated as inequality, $R \gtrsim r_{\rm f}$. Assuming that the magnetic field strength at the emission site is on the order of 100 Gauss (this value is justified by Y2002), the velocity of non-thermal gyrosynchrotron-emitting electrons is almost the speed of light (Bastian, 1999), $v \sim c = 3 \times 10^5$ km s^{-1}. Using these, we can evaluate the magnetic mirror ratio as well as the initial pitch-angle cosine from equations (5.2.6) and (5.2.7),

$$\mu_0 = \frac{\omega R}{c} \gtrsim 0.47, \tag{5.2.8}$$

$$M = 1 + \frac{\omega r_{\rm f}/c}{1-\mu_0^2} \gtrsim 1.3. \tag{5.2.9}$$

On the other hand, Y2002 implemented the potential magnetic field extrapolation to the *SOHO*/MDI photospheric magnetic field data, and obtained a magnetic field strength at the loop top, $B_0 \sim 200$ Gauss. The photospheric magnetic field strength at the west loop end is ~ 400 Gauss. Therefore we evaluate $1.3 \lesssim M \lesssim 2$. Substituting $M = 2$ in equation (5.2.7), we obtain $\mu_0 = 0.88$. Consequently we evaluate $0.47 \lesssim \mu_0 \lesssim 0.88$, and thus $28^\circ \lesssim \alpha_0 \lesssim 62^\circ$ which is smaller than that derived by Y2002. This is because we consider the magnetic field convergence while they did not.

5.3 Numerical Model

In the previous section, we only treat the motion of a single electron. Our goal is to numerically model the gyrosynchrotron intensity distribution along the loop for comparison with the observation. For this purpose, we first numerically model the electron propagation in the loop by the Fokker-Planck treatment of the electron distribution in phase space. This modeling is essentially same as that in chapter 3. The same formulae appeared in § 3.3 are used.

The gyro-averaged Fokker-Planck equation is

$$\frac{\partial N}{\partial t} + \mu c \beta \frac{\partial N}{\partial r} + \frac{\partial}{\partial \mu}\left(\dot{\mu} N\right) + \frac{\partial}{\partial E}\left(\dot{E} N\right) = \frac{\partial}{\partial \mu}\left(D_{\mu\mu}\frac{\partial N}{\partial \mu}\right). \tag{5.3.1}$$

Here $N(r, \mu, E, t)$ is the electron distribution in phase space (number of electrons per unit length per unit pitch-angle cosine per unit energy), $\dot{E}$ and $D_{\mu\mu}$ are the Coulomb energy loss rate and pitch-angle diffusion coefficient, $\dot{\mu}$ is the magnetic mirroring force, $E = \Gamma - 1$ is the kinetic energy in units of the electron rest mass energy $m_{\rm e}c^2$, Γ is the Lorentz factor, $\beta = \sqrt{1 - \Gamma^{-2}}$, and $m_{\rm e}$ is the electron mass, respectively.

We adopt the Coulomb energy loss rate and pitch-angle diffusion coefficient from equations (3.3.2) and (3.3.3). The ambient plasma number density and the Coulomb logarithm are treated as constant, $n = 10^{10}$ cm^{-3} and $\ln \Lambda = 25$. Since we address shorter timescale (order of 1 sec) phenomena than the Coulomb collision time (order of 100 sec for 1 MeV electrons), the results and conclusion are almost independent of these variables.

The magnetic mirroring force, which is given in equation (3.3.4), depends on the

gradient of the magnetic field strength along the field line. In addition, detailed information on the magnetic field configuration is necessary to simulate the spatial distribution of the gyrosynchrotron radiation because it depends on a viewing angle with respect to the magnetic field line, while the actual magnetic field configuration in solar flares is unknown. In this model, we employ the potential magnetic field configuration for simplicity. We give the two-dimensional, static, and symmetric potential magnetic field in Cartesians coordinate as follows:

$$\begin{cases} B_x = B_{\rm f}\cos(kx)e^{-kz}, \\ B_z = -B_{\rm f}\sin(kx)e^{-kz}, \end{cases} \tag{5.3.2}$$

where x and z directions correspond to the tangential and normal directions relative to the solar surface, respectively. The parameter of k specifies the magnetic field line, determined from $r_{\rm f}$ and M (see below). This magnetic field configuration is shown in the left panel of Figure 5.2.

The strength of this potential magnetic field measured along the field line is written as

$$B(r) = \frac{B_0}{\cos\left[\sin^{-1}\left\{\tanh(kr)\right\}\right]}, \tag{5.3.3}$$

where

$$k = \frac{1}{2r_{\rm f}}\ln\left[\frac{1+\sin\left\{\cos^{-1}\left(M^{-1}\right)\right\}}{1-\sin\left\{\cos^{-1}\left(M^{-1}\right)\right\}}\right]. \tag{5.3.4}$$

The top right panel of Figure 5.2 shows the magnetic field strength measured along the field line. We use parameters of $r_{\rm f} = 4.5\times10^4$ km and $M = 1.6$ based on the estimation in § 5.2. The form of the potential magnetic field strength (eq. (5.3.3), solid line) is very close to the quadratic function (eq. (5.2.3), dashed line), allowing us to use the analytic solution derived in § 5.2 as an approximation for the calculation result.

We give the initial condition for N as

$$N(r,\mu,E,0) = \exp\left[-\left(\frac{r}{0.2r_{\rm f}}\right)^2\right]\phi(\mu)E^{-4}, \tag{5.3.5}$$

where $\phi(\mu)$ is the initial pitch-angle distribution given later. By this equation, electrons are initially injected at the loop top. The initial condition is given to be

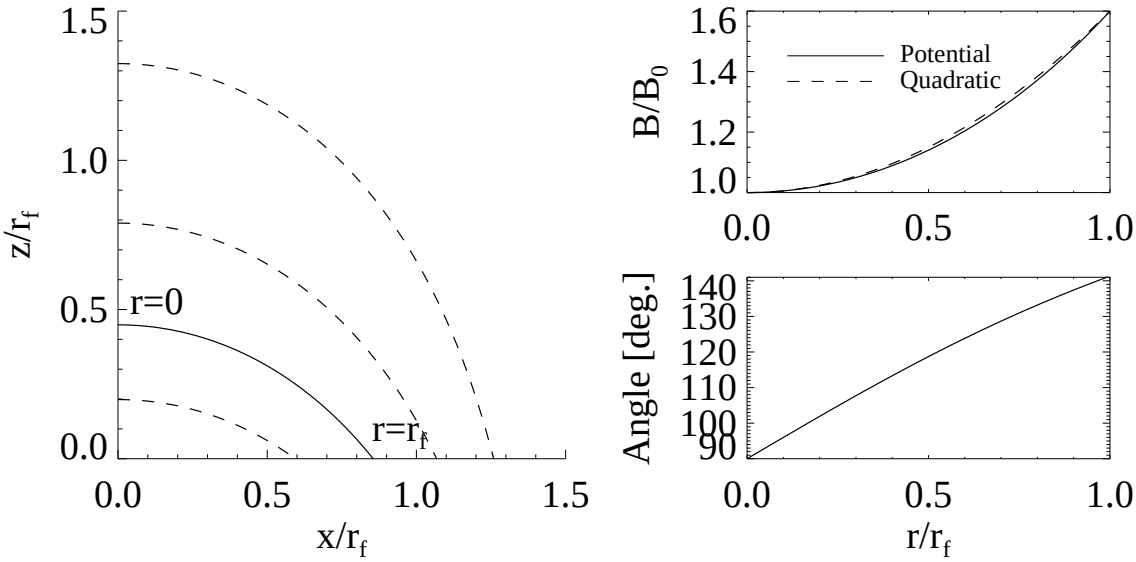

Figure 5.2: *Left*: The potential magnetic field configuration described by equation (5.3.2). The x- and z-axes correspond to the tangential and normal directions relative to the solar surface, respectively. We solve the Fokker-Planck equation (eq. (5.3.1)) along the thick line which has the half loop length $r_{\rm f} = 4.5 \times 10^4$ km and the magnetic mirror ratio $M = 1.6$. *Top right*: The magnetic field strength measured along the field line (thick line in the left panel). The solid and dashed lines correspond to equations (5.3.3) and (5.2.3), respectively. *Bottom right*: A viewing angle θ with respect to the magnetic field line (thick line in the left panel) described by equation (5.3.6). The loop is assumed to be located at the disk center. When the loop is on the limb with orientation in north-south, $\theta = 90°$ is independent of r.

symmetric in (r, μ) space that yields the symmetric solution of equation (5.3.1): $N(r, \mu, E, t) = N(-r, -\mu, E, t)$.

We numerically solve equation (5.3.1) by using the scheme described in § 3.3.2. We set 64×128 cells in (r, μ) space, and 128 logarithmically-spaced grids from 50 to 5000 keV in E space, respectively.

Using the electron distribution $N(r, \mu, E, t)$, we further numerically calculate the distribution of the gyrosynchrotron radiation for comparison with the observation of Y2002. Since the 17 GHz microwave emission observed with NoRH in the 1999 August 28 flare is the optically thin, non-thermal gyrosynchrotron radiation as presented in Y2002, it is sufficient for our purpose to consider only the optically thin gyrosynchrotron radiation at high harmonics ($10 \lesssim \nu/\nu_{\rm B} \lesssim 100$) from mildly rela-

tivistic electrons ($\Gamma \lesssim 10$). Therefore, we use the approximation given by Petrosian (1981) to calculate the gyrosynchrotron emissivity (Appendix D).

The gyrosynchrotron emissivity $j_\nu(r, \theta, t)$ depends on a magnetic field strength and a viewing angle θ with respect to the magnetic field line at the emission site as well as the parent electron distribution. We set a magnetic field strength at the loop top of $B_0 = 200$ Gauss. A viewing angle is determined from the location and orientation of the loop on the Sun, and its tilt relative to the solar surface. We do not consider the tilt for the determination of θ for simplicity, and employ two ideal cases of the loop location and orientation: (1) the loop is located at the disk center ("disk" case); and (2) it is on the limb oriented north-south ("limb" case). In the disk case, θ is written as a function of r from the model magnetic field configuration (eq. (5.3.2)),

$$\theta(r) = \cos^{-1}\left[-\tanh(kr)\right], \tag{5.3.6}$$

and in the limb case $\theta = 90°$ is independent of r. The bottom right panel of Figure 5.2 shows $\theta(r)$ in the disk case.

We use the gyrosynchrotron intensity $I_\nu(r, \theta, t)$, which is the observed variable, instead of the emissivity. This can be calculated by considering the projection effect of the loop by an observer, $I_\nu(r, \theta, t) \propto j_\nu(r, \theta, t)/\sqrt{B(r)}\sin\theta(r)$ (given in eq. (3.4.9)).

5.4 Calculation Results and Interpretation

In this section, we present our model calculation results and address whether the apparent propagating motion of the microwave source reported by Y2002 actually corresponds to the motion of electrons injected with a specific initial pitch angle. To discuss this, we perform calculations for two cases of the pitch-angle distribution of the initial condition ($\phi(\mu)$ in eq. (5.3.5)): "narrow-band" case (§ 5.4.1) and "broad-band" case (§ 5.4.2).

5.4.1 Narrow-Band Case

We first consider that initially injected electrons have an almost unique pitch angle, following the interpretation made by Y2002. To simulate this case, we give an

initial pitch-angle distribution as follows:

$$\phi(\mu) = \exp\left[-\left(\frac{|\mu| - \mu_{\rm p}}{0.1}\right)^2\right], \tag{5.4.1}$$

where we set $\mu_{\rm p} = \sqrt{1 - M^{-1}} = 0.612$, which is the loss cone angle cosine.

The top left panel of Figure 5.4 shows the time variation of the 1 MeV electron number distribution along the loop. The vertical axis corresponds to the spatial coordinates from the loop top to the footpoint. To illustrate this (and the top right panel), we use the pitch-angle integrated variable:

$$N_\mu(r, E, t) = \int_{-1}^{1} d\mu N(r, \mu, E, t). \tag{5.4.2}$$

The solid and dashed lines show the trajectories of electrons with initial pitch-angle cosine of respective ± 0.61 and ± 0.4, obtained by solving equation (5.2.1) with equations (5.2.2) and (5.3.3) (not eq. (5.2.3)) by using the 4th order Runge-Kutta method.

Initially injected electrons move toward the footpoint and about a half of them reach there at 0.2 - 0.4 sec. They are lost from the calculation box because they are initially in the loss cone. Remaining electrons are bounced back by the magnetic mirror and move toward the opposite direction. Subsequent diffusion in (r, μ) space by Coulomb collisions is ignorable since the collision time ($\sim$ 200 s) is much longer than the calculation time (2 s).

The middle and bottom left panels of Figure 5.4 show the time variation of the 17 GHz gyrosynchrotron intensity distribution along the loop located at the disk center and on the limb, respectively. Note that the vertical scale of the middle left (and middle right) panel is slightly different from other panels because of the projection effect of the loop.

The maximum intensity of the gyrosynchrotron radiation is larger in the limb case than in the disk case (see color bars of the middle and bottom left panels). The magnetic field strength at the brightest site is larger in the limb case than in the disk case. The effective energy of electrons contributing to the gyrosynchrotron radiation at a fixed frequency decreases when the magnetic field strength increases (Lu & Petrosian, 1989; Bastian, 1999). Therefore, lower energy electrons contribute to the 17 GHz gyrosynchrotron radiation in the limb case than in the disk case.

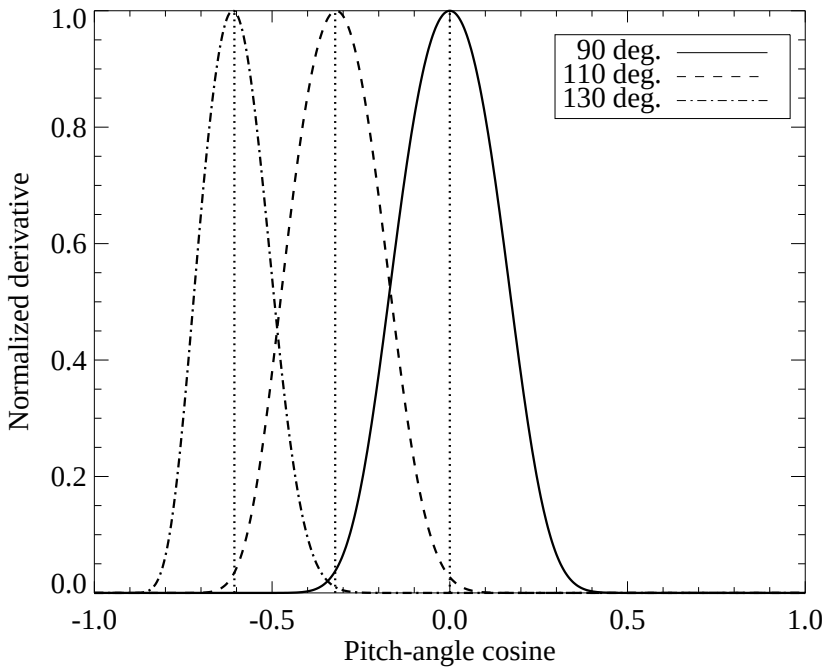

Figure 5.3: Normalized contribution functions to 17 GHz gyrosynchrotron radiation from 1 MeV electrons with an isotropic pitch-angle distribution as a function of the viewing angle (solid, dashed, and dash-dotted lines for $\theta = 90$, 110, and 130 degree). The source is assumed to be homogeneous with a magnetic field strength of 200 Gauss. The dotted lines show $\mu = \beta \cos\theta$.

Consequently, the number of primary gyrosynchrotron-emitting electrons and the intensity of the resultant emission are larger in the limb case than in the disk case.

The strong gyrosynchrotron source is localized in space along the loop. In the limb case (bottom left), radiation primarily comes from the footpoint. In the disk case (middle left), strong radiation comes from the intermediate position between the loop top and footpoint. These results are attributed to the dependence of the gyrosynchrotron emissivity on a viewing angle as well as the parent electron distribution along the loop. We interpret these results by using the analytic solution in § 5.2.

Figure 5.3 shows the contribution function to 17 GHz gyrosynchrotron radiation from 1 MeV electrons with an isotropic pitch-angle distribution. The radiation is primarily emitted by the electrons with the pitch-angle cosine (Petrosian, 1981; Lu

& Petrosian, 1990),

$$\mu \sim \beta \cos\theta \equiv \mu_{\rm g}, \tag{5.4.3}$$

that is dependent on θ. Therefore it is different between the disk and limb cases.

Disk case

When the loop is at the disk center, θ is described by equation (5.3.6) and thus $\mu_{\rm g} = -\beta \tanh(kr)$. Using equations (5.2.2) and (5.2.3), the position $r_{\rm g}$ where electrons satisfy $\mu = \mu_{\rm g}$ is the solution of the following equation,

$$\beta \tanh(kr_{\rm g}) = \sqrt{\mu_0^2 - (1-\mu_0^2)(M-1)\left(\frac{r_{\rm g}}{r_{\rm f}}\right)^2}. \tag{5.4.4}$$

In the narrow-band case, we consider that injected electrons have an almost unique initial pitch angle (eq. (5.4.1)), $\mu_0 \sim \mu_{\rm p} = \sqrt{1-M^{-1}}$. Using this, equation (5.4.4) is rewritten as

$$\beta \tanh(kr_{\rm g}) \sim \sqrt{(1-M^{-1})\left\{1-\left(\frac{r_{\rm g}}{r_{\rm f}}\right)^2\right\}}, \tag{5.4.5}$$

that gives $r_{\rm g}$ of an intermediate value between 0 and $r_{\rm f}$. Therefore the strong radiation comes from the intermediate position between the loop top and footpoint. This explains the gyrosynchrotron intensity distribution in the middle left panel of Figure 5.4.

Limb case

When the loop is on the limb with orientation in north-south, $\theta = 90°$ and thus $\mu_{\rm g} = 0$. Using equations (5.2.2) and (5.2.3), the position where electrons satisfy $\mu = \mu_{\rm g} = 0$ and thus emit the strong radiation is

$$r_{\rm g} = \frac{\mu_0}{\sqrt{(1-\mu_0^2)(M-1)}} r_{\rm f}. \tag{5.4.6}$$

Using $\mu_0 \sim \mu_{\rm p} = \sqrt{1-M^{-1}}$, this results in $r_{\rm g} \sim r_{\rm f}$. Therefore the strong radiation comes from the footpoint. This explains the gyrosynchrotron intensity distribution in the bottom left panel of Figure 5.4.

Based on these discussions, we conclude that electrons injected into the loop with an almost unique pitch angle do not yield the propagating feature of the radiation source along the loop. This does not support the interpretation of Y2002 that the observed propagating feature of the microwave source corresponds to the motion of electrons with a specific initial pitch angle.

5.4.2 Broad-Band Case

Next, we consider that initially injected electrons have an isotropic pitch-angle distribution: $\phi(\mu) = \text{constant}$. Electrons with small initial pitch angle can reach the footpoint while those with large initial pitch angle are confined to a narrow region around the loop top.

The top right panel of Figure 5.4 shows the time variation of the 1 MeV electron number distribution along the loop. The solid, dashed, and dash-dotted lines show the trajectories of electrons with initial pitch-angle cosine of respective ± 0.61, ± 0.4, and ± 0.2. As expected, electrons are broadly distributed in the loop compared with the narrow-band case (top left panel).

The middle and bottom right panels of Figure 5.4 show the time variation of the 17 GHz gyrosynchrotron intensity distribution along the loop located at the disk center and on the limb, respectively. The intensity distribution is quite different from that in the narrow-band case (middle and bottom left panels). The strong radiation source is broadly distributed along the loop. We can see the propagating feature of the strong radiation source from the loop top to the footpoint in both the middle and bottom right panels, similar to the observation of Y2002. For example, rapid propagating motion is found during 0.3 - 0.5 sec and 0.9 - 1.2 sec in the bottom right panel. These features do not result from the motion of electrons with a specific initial pitch angle but from the motion of an ensemble of electrons with different initial pitch angles.

Apparent Propagating Motion of the Microwave Source

We discuss the apparent motion of the radiation source. For mathematical simplicity, we consider the limb case. As mentioned in § 5.4.1, the gyrosynchrotron radiation is primarily emitted by the electrons with $\mu \sim 0$ when the loop is on the

limb with orientation in north-south. Using equations (5.2.5) and (5.2.7), we derive the time when the pitch-angle cosine becomes zero for an electron with the initial pitch-angle cosine μ_0,

$$t_{\rm g} = \frac{1}{\omega}\left(\frac{\pi}{2} + i\pi\right) = \frac{(\pi/2 + i\pi)}{\sqrt{(1-\mu_0^2)(M-1)}}\frac{r_{\rm f}}{v}, \tag{5.4.7}$$

where i is an integer. This means that when μ_0 is smaller (i.e., an initial pitch angle is larger) $t_{\rm g}$ is smaller. At $t = t_{\rm g}$, the electron position is given by equation (5.2.4) with $\sin(\omega t_{\rm g}) = 1$. Using this, μ_0 in equation (5.4.7) can be removed and equation (5.4.7) is rewritten as

$$t_{\rm g} = \left(\frac{\pi}{2} + i\pi\right)\sqrt{1 + \frac{1}{M-1}\left(\frac{r_{\rm f}}{r_{\rm g}}\right)^2}\frac{r_{\rm g}}{v}. \tag{5.4.8}$$

This means that when $r_{\rm g}$ is smaller $t_{\rm g}$ is smaller. Therefore, $r_{\rm g}$ is smaller when μ_0 is smaller. The timing and position of an electron emitting strong radiation is dependent on its initial pitch angle. By this equation, one can trace the position of the strong gyrosynchrotron-emitting electron in (r, t) space. Figure 5.5 is the zoomed image of the bottom right panel of Figure 5.4, to compare the analytic solution (eq. (5.4.8)) with the calculation result. The thick line shows the analytic solution with $i = 0$ and $v = c$. As can be seen, the analytic solution well explains the propagating feature of the radiation source.

Based on these discussions, we interpret the microwave propagating feature in Figure 5.5 as follows. Electrons with larger (smaller) initial pitch angle emit microwaves earlier (later) at the position closer to (farther from) the loop top, as seen in the peak of the dash-dotted (solid) line in Figure 5.5. This difference, due to the difference of the initial pitch angle of the parent electrons, appears as the propagating motion of the strong microwave source along the loop from the loop top to the footpoint.

The propagation speed of the radiation source can be evaluated from the slope of the line in Figure 5.5,

$$v_{\rm prop} = \frac{dr_{\rm g}}{dt_{\rm g}} = \frac{1}{(\pi/2 + i\pi)}\sqrt{1 + \frac{1}{M-1}\left(\frac{r_{\rm f}}{r_{\rm g}}\right)^2}\,v. \tag{5.4.9}$$

The propagation of the radiation source is periodic ($i = 0, 1, 2, \ldots$), as seen in Figure 5.4. This is because initially injected electrons remain to oscillate in the loop. In the

actual flare, however, electrons should be continuously injected into the loop, different from our model treatment. Then the periodic propagation seen in our calculation would be occulted by the emissions from subsequently injected electrons, except the first one. The observable propagating motion is the first line ($i = 0$). This yields $v_{\rm prop} \gtrsim (2/\pi)c$ from equation (5.4.9), which is much faster than the observed speed of $\sim 0.3c$ in Y2002. This value is derived in the ideal case that the loop is located on the limb with orientation in north-south. In the disk case (middle right panel of Fig. 5.4), the propagation speed is slower than that in the limb case (bottom right panel). The apparent velocity of the radiation source varies with the viewing angle. For a quantitative discussion on the velocity of the radiation source, we need to determine the accurate viewing angle.

The viewing angle is determined from the magnetic field configuration, and the location, orientation and tilt of the loop with respect to the Sun. Though the loop location can be determined from the observation (Fig. 5.1), determination of the viewing angle is still difficult because the actual magnetic field configuration is unknown. Therefore we simplified our study in two ideal cases (disk and limb cases) for a qualitative understanding of the microwave propagating feature. Though a quantitative agreement is not achieved, we believe that our interpretation is valid in any probable magnetic field configuration and loop location because of the following reason.

It is supposed that a specific electron accounts for the propagating feature of the microwave source. To emit the strong radiation throughout the propagation along the loop, it should move with $\mu \sim \beta \cos\theta$ at any time and position. To satisfy this condition, the viewing angle at the footpoint must be more perpendicular to the field line than that at the loop top, because the pitch angle of electrons becomes larger with approaching the footpoint. This is hard to be realized, except for the loop located on the limb with orientation in east-west.

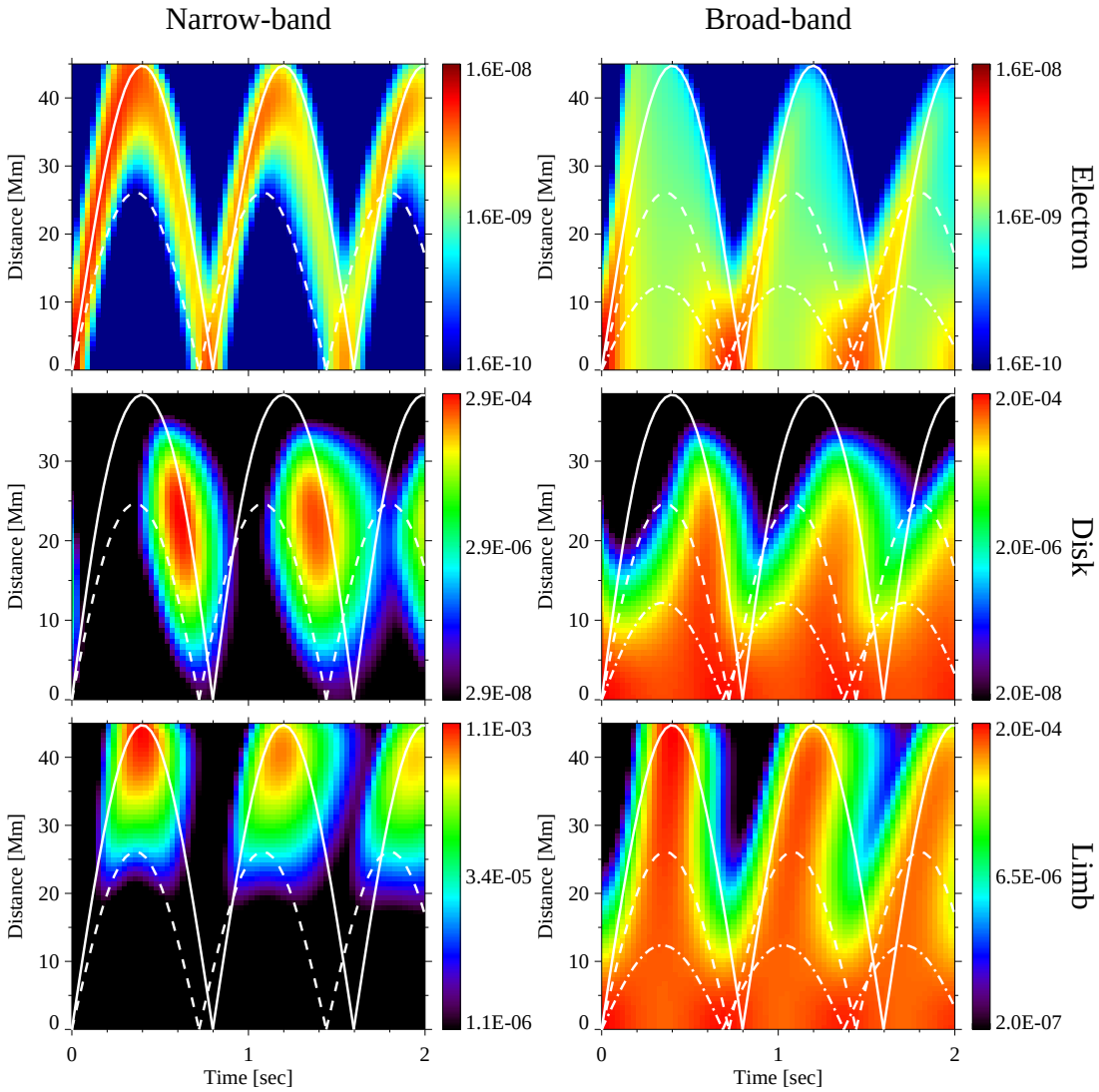

Figure 5.4: Time variations of the electron number (top) and the gyrosynchrotron intensity (middle and bottom) distributions along the loop. The vertical axis corresponds to the spatial coordinates from the loop top to the footpoint. The left and right panels correspond to the results calculated for the narrow- and broad-band cases, respectively. *Top*: The 1 MeV electron number distribution along the loop. *Middle*: The 17 GHz intensity distribution along the loop located at the disk center. Note that the vertical scale of these panels is slightly different from other panels because of the projection effect of the loop. *Bottom*: The 17 GHz intensity distribution along the loop on the limb. The solid, dashed, and dash-dotted lines show the trajectories of electrons with initial pitch-angle cosine of ± 0.61, ± 0.4, and ± 0.2, respectively.

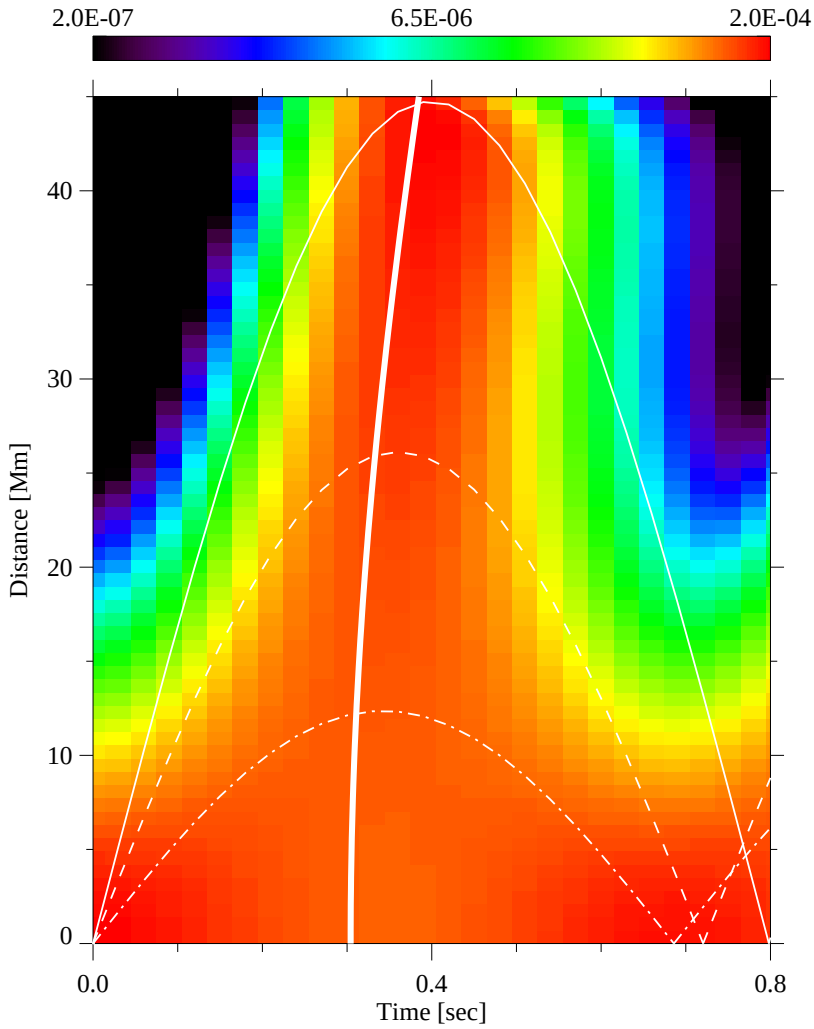

Figure 5.5: Time variation of the 17 GHz gyrosynchrotron intensity distribution along the loop on the limb during 0-0.8 sec, calculated for the broad-band case. The solid, dashed, and dash-dotted lines show the trajectories of electrons with initial pitch-angle cosine of ± 0.61, ± 0.4, and ± 0.2, respectively. The thick line shows the analytic solution (eq. (5.4.8)).

5.5 Summary and Discussion

We presented the analytic and numerical treatments of the rapid propagating feature of the non-thermal microwave source reported by Y2002, to address the pitch-angle distribution of the injected electrons. We studied this issue by modeling the electron propagation with the Fokker-Planck equation and by calculating the gyrosynchrotron radiation.

We first assumed that electrons injected into the loop have an almost unique initial pitch angle, following the interpretation made by Y2002. These electrons do not yield the propagating feature in the gyrosynchrotron intensity distribution along the loop. This does not support the interpretation of Y2002.

We next assumed that electrons injected into the loop have an isotropic pitch-angle distribution. In this case, the gyrosynchrotron intensity distribution shows the apparent motion of the strong radiation source from the loop top to the footpoint, similar to the observation. This feature is interpreted as the motion of an ensemble of electrons (not a specific electron), which have different timing and position to emit strong radiation due to the difference of their initial pitch angle. The injected electrons have to be widely distributed in pitch-angle space to yield the propagating feature.

We discuss a probable physical process of electrons in the 1999 August 28 flare. It is thought that this flare was triggered by the interaction between the loop and the compact source at [180, -520], which is possibly an unresolved compact loop (Fig. 5.1). Such configuration is suggested by Hanaoka (1999), called "double-loop flare". Hanaoka (1999) concluded that in the double-loop flare non-thermal electrons are accelerated at the region where two loops interact. Based on this model, Y2002 interpreted that the acceleration site in the 1999 August 28 flare is where the propagation of the non-thermal microwave source starts, that is, the injection region. We conclude that the non-thermal electrons in the 1999 August 28 flare start to propagate along the loop just after being isotropically accelerated at the site.

The propagating feature of the microwave source gives us opportunities to study the gyrosynchrotron radiation mechanism and the electron transport, and to constrain the pitch-angle distribution of the injected electrons. As is evident from many hard

X-ray observations showing footpoint sources (Sakao, 1994, 1999), propagation of electrons and the microwave source along the loop commonly occurs in solar flares. However, direct detection of such phenomena is quite difficult. The 1999 August 28 flare is the unique event in that NoRH detected the microwave propagating feature during its observational period until end of 2004 since its operation start in 1992 June (Shimojo, 2007). This event was an extremely well resolved one in both space and time by NoRH.

For further study, improvement of radio observatories is necessary. Observations with high temporal ($\lesssim 0.1$ s) and spatial ($\sim 1''$) resolutions will more clearly resolve the microwave source because it propagates with a velocity close to the speed of light along the loop with typical length $\lesssim 100'' \sim 7 \times 10^4$ km. Such observations should be implemented at frequencies greater than ~ 10 GHz which correspond to the optically thin regime of the microwave emissions in typical solar flares, to obtain the spectral property of non-thermal electrons. Since the gyrosynchrotron radiation depends on the viewing angle with respect to the loop, the center-to-limb variation of the microwave distribution is studied to address the electron distribution in the loop. Such study has been statistically carried out by e.g., Kosugi (1985) and Silva & Valente (2002) with spatially unresolved data. Statistical study of the center-to-limb variation of the spatial distribution of microwave emissions further gives constraints on the pitch-angle distribution of the injected electrons. Our numerical study will be of help to the future observational study for understanding of the electron dynamics in solar flares.

Chapter 6

Summaries and Concluding Discussion

Electron acceleration in solar flares is a longstanding problem. The determination of the energy and pitch-angle distribution of accelerated electrons from the observations is essential to solve it. We determined the distribution of accelerated electrons from both the observational and theoretical studies. In this chapter we present the brief summary of each previous chapter. Then we present concluding discussion, which this thesis brings, about the electron acceleration in solar flares.

6.1 Brief Summaries of Chapters

In chapter 3, we performed a comparative analysis of non-thermal emissions of HXRs and microwaves in the main impulsive phase of the 2003 May 29 flare, to reveal characteristics of non-thermal electrons in a wide energy range. We focused on the higher energy HXRs above 100 keV that have been less studied and thus less understood so far. We found that the higher energy HXRs show intermediate characteristics between the lower energy HXRs below 100 keV and microwaves. The spatial distribution of the higher energy HXRs coincides with that of the lower energy HXRs while the time profile of the spectrum of the higher energy HXRs is similar to that of the microwaves. This analysis revealed the variability of higher energy HXR-emitting electrons (in intermediate energy range) as well as lower energy HXR-

emitting electrons (in lower energy range) and microwave-emitting ones (in higher energy range).

To explain the observed variability and determine the injection pitch-angle distribution, we developed a general treatment of the electron transport model called trap-plus-precipitation, by solving the Fokker-Planck equation in space, energy, and pitch angle. Comparing the calculations and observations, we showed that the trap-plus-precipitation model in the weak diffusion regime can explain the variability of the observed non-thermal emissions. By the observed characteristics of the higher energy HXRs, we concluded that the electrons are accelerated more perpendicular to than parallel to the magnetic field line. We suggest a possible mechanism of the betatron acceleration.

In chapter 4, we performed a detailed analysis of the spatial distribution of non-thermal emissions in the early impulsive phase. We found the energy-dependent asymmetric distribution of the footpoint sources appeared at the southeast and northwest sites. The northwest footpoint HXR source is brighter (weaker) for lower (higher) energy than the southeast source, and its time profile leads the southeast. This variability could not be explained by previously proposed scenarios. We showed that this could be explained if the injected electrons have an asymmetric pitch-angle distribution in direction parallel to the magnetic field. A field-aligned electric field is a candidate to yield this pitch-angle distribution.

In chapter 5, we numerically studied the electron propagation along the loop based on the observation of the 1999 August 28 flare (Yokoyama et al., 2002). From the refined modeling of the electron propagation with the Fokker-Planck equation and the gyrosynchrotron radiation, we concluded that the injected electrons have to be widely distributed in pitch-angle space to yield the observed propagating feature of the microwave source. We suggest that the electrons are almost isotropically accelerated in this flare.

6.2 Concluding Discussion

By the observational and theoretical studies, we addressed the pitch-angle distributions of injection electrons in three cases. These are different from each other,

implying that a different acceleration mechanism efficiently works in a different physical condition. We propose three acceleration mechanisms and discuss how these mechanisms affect the pitch-angle distribution. They are the adiabatic betatron and Fermi acceleration processes, and the acceleration by a field-aligned electric field.

When the flare (magnetic reconnection) occurs, the reconnected magnetic field line moves toward the solar surface. During this convection, the field line increases its magnetic field strength and shortens its spatial length along the line. Electrons which are frozen into the magnetic field can be adiabatically accelerated via both the betatron and Fermi acceleration processes. The betatron acceleration process increases the electron perpendicular energy $E_\perp$ with conserving the magnetic moment, $E_\perp/B =$ constant, where B is the magnetic field strength. The Fermi acceleration process increases the electron parallel energy $E_\parallel$ with conserving the longitudinal invariant, $E_\parallel {r_\mathrm{c}}^2 =$ constant, where r_c is the characteristic travel length of electrons along the field line. Through these processes, accelerated electrons change their distribution in pitch-angle as well as energy space. If the betatron acceleration overcomes the Fermi acceleration, the electrons are accelerated more perpendicular to the magnetic field line, and vice versa. To discuss which acceleration process efficiently works, we assume the relationship between B and r_c as $B \propto r_\mathrm{c}^{-\xi}$.

When the magnetic field is compressed with a compression ratio of $R_\mathrm{c}(> 1)$ by the convection, the characteristic travel length shortens by a factor of $R_\mathrm{c}^{1/\xi}$ from the above assumption (with $\xi > 0$). By this compression, the electrons increase their perpendicular and parallel energies by

$$\begin{cases} E_\perp/E_{\perp,0} = R_\mathrm{c}, & \text{(betatron)}, \\ E_\parallel/E_{\parallel,0} = R_\mathrm{c}^{2/\xi}, & \text{(Fermi)}, \end{cases} \tag{6.2.1}$$

where values with subscript 0 mean their initial values. The electrons can be accelerated more efficiently in the perpendicular direction than in the parallel when $\xi > 2$. The actual value of ξ is not clear. We consider that a macroscopic magnetic field configuration is one of the keys to determine it.

We express the magnetic field strength in polar coordinates, $B = B(l)$, where l is the radius from the center (Fig. 6.1). For example, the dipole magnetic field is $B \propto l^{-3}$. If we assume that r_c is proportional to l, we obtain $B \propto l^{-\xi}$. When the magnetic field configuration in the flare is close to the dipole, ξ is close to 3 and thus

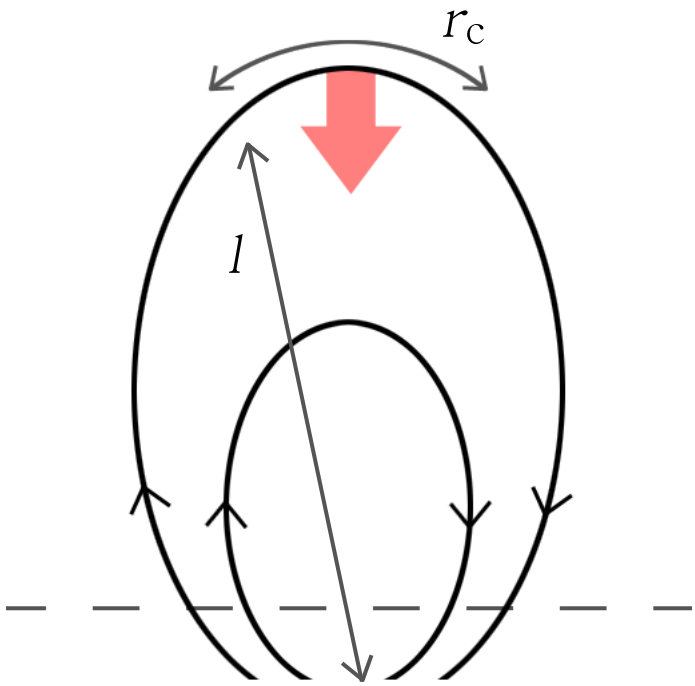

Figure 6.1: Schematic picture of the reconnected magnetic fields. The black solid lines denote the magnetic field lines. The dashed line denotes the solar surface. The red arrow denotes the direction of the convection. By the convection, the magnetic field strength of the loop is increased, yielding the adiabatic betatron acceleration in the perpendicular direction. If the characteristic travel length r_c is decreased by the convection, electrons are accelerated also in the parallel direction via the adiabatic Fermi acceleration.

the pancake pitch-angle distribution of the electrons is realized.

When the Petschek-type magnetic reconnection occurs, a pair of slow-mode shocks is formed. In this configuration, the characteristic travel length would be evaluated by a distance between shocks because most of electrons except those with enough small pitch angle are reflected at the shock by the magnetic mirroring force. In the configuration of the Petschek-type magnetic reconnection, this length becomes longer with the convection toward the downstream region. This means $\xi < 0$. Therefore the electron parallel energy is decreased while the perpendicular energy is increased by the compression. The Petschek-type magnetic reconnection yields the pancake pitch-angle distribution of the electrons via the adiabatic acceleration processes.

We consider that the magnetic field configuration in the main impulsive phase of

2003 May 29 flare (studied in chapter 3) is expected to satisfy these criteria because the flare geometry shows a simple two-dimensional structure which is approximated by the CSHKP model. However, this might not be expected in other cases (studied in chapters 4 and 5) because the geometries in these cases show a complex three-dimensional configuration that might be beyond the scope of the CSHKP model. The 1999 August 28 flare is triggered by the interaction of two loops. The appearance of multiple footpoints in the early impulsive phase of the 2003 May 29 flare implies the existence of multiple loops, which are strongly sheared with respect to the photospheric magnetic neutral line and might interact with each other. In such complex geometries, the betatron acceleration might not play a dominant role and thus the electrons do not have the pancake pitch-angle distribution.

If the characteristic travel length is independent of the electron energy, the right-hand sides of equation (6.2.1) are independent of the initial energy of electrons. This means that the pitch-angle distribution of the electrons is equally changed by these acceleration processes regardless of their energy. If an acceleration by a field-aligned electric field additionally works, the pitch-angle distribution is concentrated parallel to the magnetic field line. As shown in chapter 4, this acceleration process yields the energy-dependent difference of the pitch-angle distribution. Lower energy electrons are more concentrated in the parallel direction. This process less works on higher energy electrons. The pitch-angle distribution of higher energy electrons is almost determined by the adiabatic processes, while that of lower energy ones is significantly changed through this acceleration process.

We summarize the new insights into the electron acceleration in solar flares, which are obtained by the study in this thesis. Electrons, which would be isotropically accelerated around magnetic reconnection regions and then are ejected from there, are further adiabatically accelerated until reaching the injection site. The efficiency of the adiabatic acceleration depends on the magnetic field configuration. When the configuration is close to the dipole ($\xi > 2$) or the Petschek-type reconnection occurs ($\xi < 0$), the betatron acceleration works more efficiently than the Fermi acceleration and then the electron pitch-angle distribution is more concentrated in the perpendicular direction with respect to the magnetic field. When a field-aligned electric field is generated, lower energy electrons are efficiently accelerated and their pitch-

angle distribution is concentrated in the parallel direction, while that of higher energy electrons is less affected.

We finally give future directions. For current solar-dedicated HXR observatories, the emission sources are discriminated in space because HXR sources typically show discrete double-footpoint structure. However time resolution is not sufficient yet. In the injection and trap-plus-precipitation model, the HXR observation reflects the profile of injected electrons. If the HXR imaging observation with time resolution better than 0.1 s (a timescale of flare non-thermal electrons) is realized, it will provide an instantaneous profile of electrons. For solar-dedicated radio observatories, the high time resolution is achieved by NoRH, but the spatial resolution is insufficient. Since the microwave observation can reveal the spatial distribution of electrons along the loop, propagating electrons can be tracked (as studied in chapter 5) if the microwave loop is well resolved. When these observations are realized, we will see the instantaneous electron profiles of acceleration and transport. Combining such observations with theoretical works describing the electron acceleration as well as transport, we will further approach the origin of non-thermal electrons in solar flares.

Appendix A

Instrumentation

Here we summarize the three space-based and ground-based instruments, which could reveal variability of non-thermal emissions and electrons in solar flares, *RHESSI*, NoRP, and NoRH.

A.1 RHESSI

The *Reuven Ramaty High Energy Solar Spectroscopic Imager* (*RHESSI*; Lin et al. 2002; Fig. A.1) is the sixth in the NASA line of Small Explorer (SMEX) missions, launched on 5 February 2002. *RHESSI* is designed to explore particle acceleration and energy release in solar flares, through imaging and spectroscopy of HXR and γ-ray continua emitted by high energy electrons, and γ-ray lines emitted by ions. This is a single instrument consisting of an imager (Hurford et al., 2002) and a spectrometer (Smith et al., 2002).

The Spectrometer is made up of nine cryogenically-cooled germanium detectors (GeDs) with a spectral resolution of 1-10 keV FWHM over the energy range from 3 keV to 17 MeV, providing the highest resolution HXR (imaging) spectroscopy and the first γ-ray line spectroscopy. Nine aluminum disks (attenuators) are automatically set in front of the detectors when the photon counting rate is too high, to suppress the number of low energy incoming photons and keep the detectors from being saturated. This automated shutter system achieves a very wide dynamic range ($> 10^7$) of flare intensities to be handled.

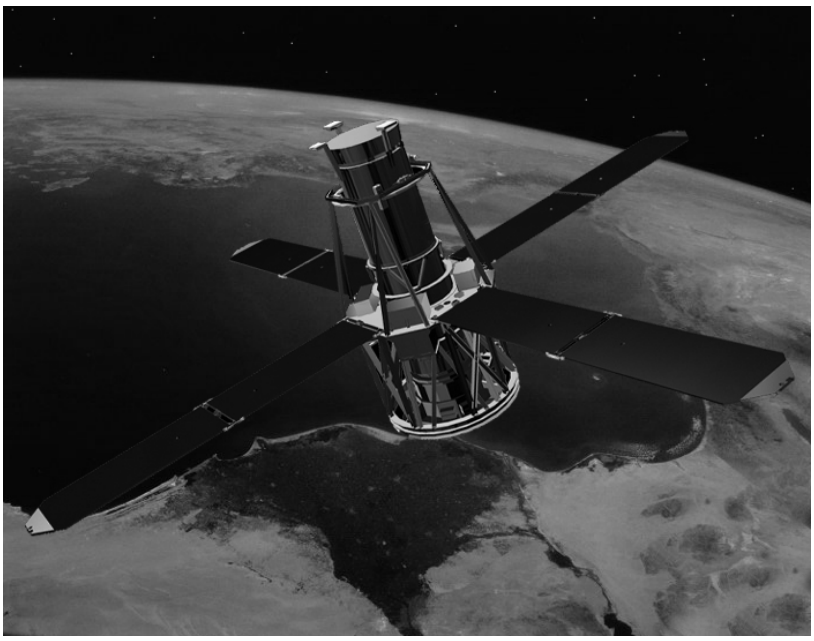

Figure A.1: *Reuven Ramaty High Energy Solar Spectroscopic Imager* (*RHESSI*).

The Imaging System is made up of nine bi-grid rotating modulation collimators (RMCs), one in front of each GeDs. As the spacecraft rotates, the RMCs convert the spatial information from the emission source into temporal modulation of the photon counting rates. The spatial information can be retrieved from the counted temporal modulation profile with a Fourier transform. The nine RMCs are so designed as to give different spatial resolutions. The spatial resolution is as fine as $\sim 2.3''$ with a full-Sun field of view, depending on which collimators are used for imaging reconstruction. Since it obtains the temporal modulation profile by the spacecraft rotation, the time resolution of images must be a rotation period, ~ 4 s.

A.2 NoRP

The Nobeyama Radio Polarimeters (NoRP; Nakajima et al. 1985 and references their in; Fig. A.2) observes the total flux and the degree of circular-polarization from the Sun with multiple frequencies of 1, 2, 3.75, 9.4, 17, 35, and 80 GHz. The time resolution is 0.1 s. The system of 17 GHz has been operated since 1978, that of 35 GHz since 1983, and that of 80 GHz since 1984. The systems of 1, 2, 3.75, and 9.4

Figure A.2: Nobeyama Radio Polarimeters (NoRP).

GHz were moved from Toyokawa Observatory of the Research Institute in 1994 and have been operated since then.

A.3 NoRH

The Nobeyama Radioheliograph (NoRH; Nakajima et al. 1994; Fig. A.3) is a solar-dedicated radio interferometer, which obtains the full Sun images with dual frequencies of 17 and 34 GHz. Both the intensity and the degree of circular-polarization are observed for 17 GHz while only the intensity are observed for 34 GHz. The time resolution is as high as 0.1 s. The spatial resolution depends on the observation condition, as high as $10''$ for 17 GHz and $5''$ for 34 GHz, respectively. Is has been operated since 1992.

NoRH is designed to investigate the location of high energy electrons in solar flares with high time and spatial resolutions. The observation frequencies are chosen to be 17 and 34 GHz, allowing us to deduce the energy distribution of high energy electrons because microwaves in this frequency range are optically thin regime in typical solar flare circumstances.

Figure A.3: Nobeyama Radioheliograph (NoRH).

Appendix B

Gaussian Fitting of the Microwave Source

We present a method to fit the microwave image with a two-dimentional elliptical gaussian function, performed in § 2.3.2. The two-dimensional elliptical gaussian function in image coordinates (x, y) is written as follows:

$$f(x,y) = T_{\mathrm{b}} \exp\left[-\frac{1}{2}(x - x_0, y - y_0) \cdot W^{-1} \cdot \begin{pmatrix} x - x_0 \\ y - y_0 \end{pmatrix}\right], \tag{B.1}$$

where T_{b} is the peak brightness temperature, (x_0, y_0) is the position of the gaussian center, and W is a second rank tensor,

$$W = \frac{1}{2\ln 2}\begin{pmatrix} (w_{xx}/2)^2 & (w_{xy}/2)^2 \\ (w_{yx}/2)^2 & (w_{yy}/2)^2 \end{pmatrix}. \tag{B.2}$$

Its components w_{xx} and w_{yy} are the gaussian full-width at half-maximum (FWHM) in x- and y-directions, respectively. The parameters for fitting are T_{b}, x_0, y_0, w_{xx}, w_{yy}, and $w_{xy}(= w_{yx})$. Figure B.1 shows an example of the fitting result for NoRH 17 GHz.

The geometry of the elliptical gaussian distribution can be expressed by three quantities: the width in directions of major (M) and minor (m) axes, and the tilt angle. These are obtained from eigenvalues and eigenvectors of the following tensor,

$$\begin{pmatrix} w_{xx} & w_{xy} \\ w_{yx} & w_{yy} \end{pmatrix}. \tag{B.3}$$

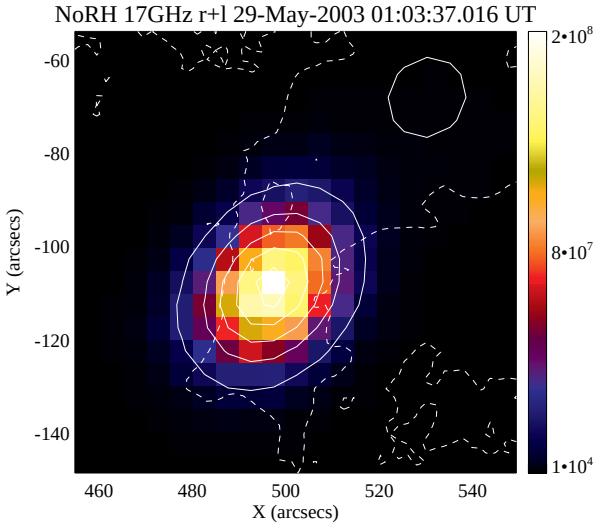

Figure B.1: Spatial distribution of 17 GHz microwave (color image in units of kelvin) overlaid by the fitting result of the elliptical gaussian function (thick solid contours) at 01:03:37 UT on 2003 May 29. Contour levels are 10%, 30%, 50%, 70%, and 90% of the peak intensity. The major axis of the elliptical gaussian is oriented to upper right. A white circle in the upper right corner denotes the beam size at half-level of the peak intensity. The dashed contours denote the photospheric magnetic neutral lines. Solar north is up and west is to the right.

Eigenvalues correspond to the gaussian FWHM in M- and m-directions (w_{MM} and w_{mm}), and eigenvectors give directions of major and minor axes. We can convert the tensor components into following variables: w_{MM}, w_{mm}, and θ which is an angle between m- and x-axes.

Appendix C

Beam Deconvolution Method

Here we present a method to approximate the shape of an actual microwave source from the observed shape, performed in § 2.3.2. Suppose that the one-dimensional shape of an emission source is described by the gaussian function with the peak intensity I^{a} and the width σ^{a},

$$f(x) = I^{\mathrm{a}} \exp\left[-\frac{1}{2}\left(\frac{x}{\sigma^{\mathrm{a}}}\right)^2\right]. \tag{C.1}$$

We express the beam size as the gaussian function,

$$b(x) = \frac{1}{\sqrt{2\pi}\sigma^{\mathrm{b}}} \exp\left[-\frac{1}{2}\left(\frac{x}{\sigma^{\mathrm{b}}}\right)^2\right]. \tag{C.2}$$

The observed shape of the emission source is the convolution of equation (C.1) by the beam,

$$\begin{aligned} g(x) &= \int_{-\infty}^{\infty} dx' f(x') b(x'-x) \\ &= \frac{I^{\mathrm{a}}}{\sqrt{2\pi}\sigma^{\mathrm{b}}} \int_{-\infty}^{\infty} dx' \exp\left[-\frac{1}{2}\left\{\left(\frac{x'}{\sigma^{\mathrm{a}}}\right)^2 + \left(\frac{x'-x}{\sigma^{\mathrm{b}}}\right)^2\right\}\right] \\ &= \left(I^{\mathrm{a}}\frac{\sigma^{\mathrm{a}}}{\sigma}\right) \exp\left[-\frac{1}{2}\left(\frac{x}{\sigma}\right)^2\right]. \end{aligned} \tag{C.3}$$

The observed shape is also described by the gaussian with the peak intensity and the width of

$$\begin{cases} I = I^{\mathrm{a}}\sigma^{\mathrm{a}}/\sigma, \\ \sigma = \sqrt{(\sigma^{\mathrm{a}})^2 + (\sigma^{\mathrm{b}})^2}. \end{cases} \tag{C.4}$$

Since we obtain I, σ, and σ_{b}, we approximate the shape of an actual emission source by using this relation.

Appendix D

Formula for the Gyrosynchrotron Emissivity

In chapters 3 and 5, we calculated the gyrosynchrotron emissivity from the calculated electron distribution. A general calculation of the gyrosynchrotron radiation in a magnetized plasma (Ramaty, 1969) includes effects such as self-absorption, absorption by ambient plasma, and Razin suppression. These contribute at low harmonics ($\nu/\nu_{\rm B} \lesssim 10$, where $\nu_{\rm B}$ is the electron gyrofrequency) of the gyrosynchrotron radiation. In our current study, however, only the optically thin gyrosynchrotron radiation at high harmonics ($10 \lesssim \nu/\nu_{\rm B} \lesssim 100$) from mildly relativistic electrons ($\Gamma \lesssim 10$, where Γ is the Lorentz factor) is of interest. Under such limited conditions, there is a useful expression given by Petrosian (1981). We adopt his formula to predict the microwave emission from the calculated electron distribution. The approximate expression of the gyrosynchrotron emissivity at a frequency ν and a viewing angle $\theta(r)$ with respect to the magnetic field (r is the spatial coordinates along the magnetic field line), from mildly relativistic electrons with arbitrary energy and pitch-angle distributions, is as follows;

$$\begin{aligned} j_\nu(r,\theta,t) &= \frac{e^2\nu_{\rm B}}{c}\left(\frac{\nu}{\nu_{\rm B}\sin^2\theta}\right)\int_1^\infty d\Gamma \times \\ &\quad \int_{-1}^{1} d\mu N(r,\mu,\Gamma,t)Y(\theta,\Gamma,\mu)\mathcal{Z}^{2m}(\theta,\Gamma,\mu), \end{aligned} \tag{D.1}$$

where $N(r, \mu, \Gamma, t)$ is the electron number distribution in phase space along the line, μ is the pitch-angle cosine, c is the speed of light, $\beta = \sqrt{1 - \Gamma^{-2}}$, e is the elementary charge, and,

$$Y = \frac{(\cos\theta - \mu\beta)^2 + (1 - z^2)(1 - \beta\mu\cos\theta)^2}{(1 - z^2)^{1/2}(1 - \beta\mu\cos\theta)}, \quad m = \frac{\nu\Gamma}{\nu_{\mathrm{B}}}(1 - \beta\mu\cos\theta)$$
$$\mathcal{Z} = \frac{z\exp\left[(1 - z^2)^{1/2}\right]}{1 + (1 - z^2)^{1/2}}, \quad z = \frac{\beta\sin\theta(1 - \mu^2)^{1/2}}{1 - \beta\mu\cos\theta}. \tag{D.2}$$

When the magnetic field strength is given as a function of r, ν_{B} is a function of r.

Bibliography

Alexander, D., & Coyner, A. J. 2006, Astrophys. J., 640, 505

Alexander, D., Harra-Murnion, L. K., Khan, J. I., & Matthews, S. A. 1998, Astrophys. J., 494, L235

Alexander, D., & Metcalf, T. R. 2002, Sol. Phys., 210, 323

Antonucci, E., Gabriel, A. H., Acton, L. W., Leibacher, J. W., Culhane, J. L., Rapley, C. G., Doyle, J. G., Machado, M. E., & Orwig, L. E. 1982, Sol. Phys., 78, 107

Antonucci, E., Gabriel, A. H., & Dennis, B. R. 1984, Astrophys. J., 287, 917

Asai, A., Ishii, T. T., Kurokawa, H., Yokoyama, T., & Shimojo, M. 2003, Astrophys. J., 586, 624

Asai, A., Masuda, S., Yokoyama, T., Shimojo, M., Isobe, H., Kurokawa, H., & Shibata, K. 2002, Astrophys. J., 578, L91

Asai, A., Yokoyama, T., Shimojo, M., Masuda, S., Kurokawa, H., & Shibata, K. 2004, Astrophys. J., 611, 557

Aschwanden, M. J. 1998, Astrophys. J., 502, 455

—. 2002, Particle Acceleration and Kinematics in Solar Flares (Particle Acceleration and Kinematics in Solar Flares, A Synthesis of Recent Observations and Theoretical Concepts, by Markus J. Aschwanden, Lockheed Martin, Advanced technology Center, palo Alto, California, U.S.A. Reprinted from SPACE SCIENCE REVIEWS, Volume 101, Nos. 1-2 Kluwer Academic Publishers, Dordrecht)

Aschwanden, M. J., Bynum, R. M., Kosugi, T., Hudson, H. S., & Schwartz, R. A. 1997, Astrophys. J., 487, 936

Aschwanden, M. J., Fletcher, L., Sakao, T., Kosugi, T., & Hudson, H. 1999, Astrophys. J., 517, 977

Aschwanden, M. J., Hudson, H., Kosugi, T., & Schwartz, R. A. 1996a, Astrophys. J., 464, 985

Aschwanden, M. J., Kosugi, T., Hudson, H. S., Wills, M. J., & Schwartz, R. A. 1996b, Astrophys. J., 470, 1198

Aschwanden, M. J., Schmahl, E., & The Rhessi Team. 2002, Sol. Phys., 210, 193

Aschwanden, M. J., & Schwartz, R. A. 1996, Astrophys. J., 464, 974

Aschwanden, M. J., Schwartz, R. A., & Dennis, B. R. 1998, Astrophys. J., 502, 468

Aschwanden, M. J., Wills, M. J., Hudson, H. S., Kosugi, T., & Schwartz, R. A. 1996c, Astrophys. J., 468, 398

Bai, T., & Dennis, B. 1985, Astrophys. J., 292, 699

Bai, T., & Ramaty, R. 1976, Sol. Phys., 49, 343

Bastian, T. S. 1999, in Proceedings of the Nobeyama Symposium, held in Kiyosato, Japan, Oct. 27-30, 1998, Eds.: T. S. Bastian, N. Gopalswamy and K. Shibasaki, NRO Report No. 479., p.211-222

Bastian, T. S., Benz, A. O., & Gary, D. E. 1998, Annu. Rev. Astron. Astrophys., 36, 131

Bastian, T. S., Nitta, N., Kiplinger, A. L., & Dulk, G. A. 1994, in Proceedings of Kofu Symposium, 199–202

Benka, S. G., & Holman, G. D. 1994, Astrophys. J., 435, 469

Brown, J. C. 1971, Sol. Phys., 18, 489

Carmichael, H. 1964, in The Physics of Solar Flares, 451

Carrington, R. C. 1859, Mon. Not. R. Astron. Soc., 20, 13

Cornell, M. E., Hurford, G. J., Kiplinger, A. L., & Dennis, B. R. 1984, Astrophys. J., 279, 875

Craig, I. J. D., MacKinnon, A. L., & Vilmer, N. 1985, Astrophys. & Space Sci., 116, 377

Crannell, C. J., Frost, K. J., Saba, J. L., Maetzler, C., & Ohki, K. 1978, Astrophys. J., 223, 620

Domingo, V., Fleck, B., & Poland, A. I. 1995, Sol. Phys., 162, 1

Duijveman, A., Hoyng, P., & Machado, M. E. 1982, Sol. Phys., 81, 137

Dulk, G. A. 1985, Annu. Rev. Astron. Astrophys., 23, 169

Falewicz, R., & Siarkowski, M. 2007, Astron. & Astrophys., 461, 285

Fleishman, G. D., & Melnikov, V. F. 2003, Astrophys. J., 587, 823

Fletcher, L., Hannah, I. G., Hudson, H. S., & Metcalf, T. R. 2007, Astrophys. J., 656, 1187

Fletcher, L., & Martens, P. C. H. 1998, Astrophys. J., 505, 418

Goff, C. P., Matthews, S. A., van Driel-Gesztelyi, L., & Harra, L. K. 2004, Astron. & Astrophys., 423, 363

Golub, L., Deluca, E., Austin, G., Bookbinder, J., Caldwell, D., Cheimets, P., Cirtain, J., Cosmo, M., Reid, P., Sette, A., Weber, M., Sakao, T., Kano, R., Shibasaki, K., Hara, H., Tsuneta, S., Kumagai, K., Tamura, T., Shimojo, M., McCracken, J., Carpenter, J., Haight, H., Siler, R., Wright, E., Tucker, J., Rutledge, H., Barbera, M., Peres, G., & Varisco, S. 2007, Sol. Phys., 243, 63

Grigis, P. C., & Benz, A. O. 2006, Astron. & Astrophys., 458, 641

Hamilton, R. J., Lu, E. T., & Petrosian, V. 1990, Astrophys. J., 354, 726

Hanaoka, Y. 1996, Sol. Phys., 165, 275

—. 1997, Sol. Phys., 173, 319

—. 1999, Publ. Astron. Soc. Japan, 51, 483

Handy, B. N., Acton, L. W., Kankelborg, C. C., Wolfson, C. J., Akin, D. J., Bruner, M. E., Caravalho, R., Catura, R. C., Chevalier, R., Duncan, D. W., Edwards, C. G., Feinstein, C. N., Freeland, S. L., Friedlaender, F. M., Hoffmann, C. H., Hurlburt, N. E., Jurcevich, B. K., Katz, N. L., Kelly, G. A., Lemen, J. R., Levay, M., Lindgren, R. W., Mathur, D. P., Meyer, S. B., Morrison, S. J., Morrison, M. D., Nightingale, R. W., Pope, T. P., Rehse, R. A., Schrijver, C. J., Shine, R. A., Shing, L., Strong, K. T., Tarbell, T. D., Title, A. M., Torgerson, D. D., Golub, L., Bookbinder, J. A., Caldwell, D., Cheimets, P. N., Davis, W. N., Deluca, E. E., McMullen, R. A., Warren, H. P., Amato, D., Fisher, R., Maldonado, H., & Parkinson, C. 1999, Sol. Phys., 187, 229

Hasegawa, A. 1976, J. Geophys. Res., 81, 5083

Haug, E. 1997, Astron. & Astrophys., 326, 417

Hirayama, T. 1974, Sol. Phys., 34, 323

Holman, G. D. 1985, Astrophys. J., 293, 584

Hudson, H. S. 1972, Sol. Phys., 24, 414

Hudson, H. S., Wolfson, C. J., & Metcalf, T. R. 2006, Sol. Phys., 234, 79

Hurford, G. J., Schmahl, E. J., Schwartz, R. A., Conway, A. J., Aschwanden, M. J., Csillaghy, A., Dennis, B. R., Johns-Krull, C., Krucker, S., Lin, R. P., McTiernan, J., Metcalf, T. R., Sato, J., & Smith, D. M. 2002, Sol. Phys., 210, 61

Imada, S., Hoshino, M., & Mukai, T. 2005, Geophys. Res. Lett., 32, 9101

Isobe, H., Kubo, M., Minoshima, T., Ichimoto, K., Katsukawa, Y., Tarbell, T. D., Tsuneta, S., Berger, T. E., Lites, B. W., Nagata, S., Shimizu, T., Shine, R. A., Suematsu, Y., & Title, A. 2007, Publ. Astron. Soc. Japan, 59, S807

Jing, J., Lee, J., Liu, C., Gary, D. E., & Wang, H. 2007, Astrophys. J., 664, L127

Kane, S. R. 1974, in IAU Symp. 57: Coronal Disturbances, 105–141

Karlický, M., & Kosugi, T. 2004, Astron. & Astrophys., 419, 1159

Kennel, C. F., & Petscheck, H. E. 1966, J. Geophys. Res., 71, 1

Khan, J. I., Harra-Murnion, L. K., Hudson, H. S., Lemen, J. R., & Sterling, A. C. 1995, Astrophys. J., 452, L153

Kiplinger, A. L., Dennis, B. R., Frost, K. J., & Orwig, L. E. 1984, Astrophys. J., 287, L105

Kiplinger, A. L., Dennis, B. R., Frost, K. J., Orwig, L. E., & Emslie, A. G. 1983, Astrophys. J., 265, L99

Kopp, R. A., & Pneuman, G. W. 1976, Sol. Phys., 50, 85

Kosugi, T. 1985, Publ. Astron. Soc. Japan, 37, 575

Kosugi, T., Dennis, B. R., & Kai, K. 1988, Astrophys. J., 324, 1118

Kosugi, T., Masuda, S., Makishima, K., Inda, M., Murakami, T., Dotani, T., Ogawara, Y., Sakao, T., Kai, K., & Nakajima, H. 1991, Sol. Phys., 136, 17

Kosugi, T., Matsuzaki, K., Sakao, T., Shimizu, T., Sone, Y., Tachikawa, S., Hashimoto, T., Minesugi, K., Ohnishi, A., Yamada, T., Tsuneta, S., Hara, H., Ichimoto, K., Suematsu, Y., Shimojo, M., Watanabe, T., Shimada, S., Davis, J. M., Hill, L. D., Owens, J. K., Title, A. M., Culhane, J. L., Harra, L. K., Doschek, G. A., & Golub, L. 2007, Sol. Phys., 243, 3

Krucker, S., Hurford, G. J., Shih, A. Y., & Lin, R. P. 2007, in American Astronomical Society Meeting Abstracts, Vol. 210, American Astronomical Society Meeting Abstracts, 93.14

Kundu, M. R., Nindos, A., White, S. M., & Grechnev, V. V. 2001, Astrophys. J., 557, 880

Kundu, M. R., White, S. M., Gopalswamy, N., & Lim, J. 1994, Astrophys. J. Suppl., 90, 599

Leach, J., & Petrosian, V. 1981, Astrophys. J., 251, 781

Lee, J., & Gary, D. E. 2000, Astrophys. J., 543, 457

Lee, J., Gary, D. E., & Shibasaki, K. 2000, Astrophys. J., 531, 1109

Lin, R. P., Dennis, B. R., Hurford, G. J., Smith, D. M., Zehnder, A., Harvey, P. R., Curtis, D. W., Pankow, D., Turin, P., Bester, M., Csillaghy, A., Lewis, M., Madden, N., van Beek, H. F., Appleby, M., Raudorf, T., McTiernan, J., Ramaty, R., Schmahl, E., Schwartz, R., Krucker, S., Abiad, R., Quinn, T., Berg, P., Hashii, M., Sterling, R., Jackson, R., Pratt, R., Campbell, R. D., Malone, D., Landis, D., Barrington-Leigh, C. P., Slassi-Sennou, S., Cork, C., Clark, D., Amato, D., Orwig, L., Boyle, R., Banks, I. S., Shirey, K., Tolbert, A. K., Zarro, D., Snow, F., Thomsen, K., Henneck, R., Mchedlishvili, A., Ming, P., Fivian, M., Jordan, J., Wanner, R., Crubb, J., Preble, J., Matranga, M., Benz, A., Hudson, H., Canfield, R. C., Holman, G. D., Crannell, C., Kosugi, T., Emslie, A. G., Vilmer, N., Brown, J. C., Johns-Krull, C., Aschwanden, M., Metcalf, T., & Conway, A. 2002, Sol. Phys., 210, 3

Lin, R. P., Schwartz, R. A., Pelling, R. M., & Hurley, K. C. 1981, Astrophys. J., 251, L109

Litvinenko, Y. E. 1996, Astrophys. J., 462, 997

Liu, C., Lee, J., Gary, D. E., & Wang, H. 2007, Astrophys. J., 658, L127

Lu, E. T., & Petrosian, V. 1988, Astrophys. J., 327, 405

—. 1989, Astrophys. J., 338, 1122

—. 1990, Astrophys. J., 354, 735

Machado, M. E., Ong, K. K., Emslie, A. G., Fishman, G. J., Meegan, C., Wilson, R., & Paciesas, W. S. 1993, Advances in Space Research, 13, 175

MacKinnon, A. L. 1986, Astron. & Astrophys., 163, 239

—. 1988, Astron. & Astrophys., 194, 279

—. 1991, Astron. & Astrophys., 242, 256

MacKinnon, A. L., Brown, J. C., Trottet, G., & Vilmer, N. 1983, Astron. & Astrophys., 119, 297

MacKinnon, A. L., & Craig, I. J. D. 1991, Astron. & Astrophys., 251, 693

Masuda, S., Kosugi, T., Hara, H., Sakao, T., Shibata, K., & Tsuneta, S. 1995, Publ. Astron. Soc. Japan, 47, 677

Masuda, S., Kosugi, T., Hara, H., Tsuneta, S., & Ogawara, Y. 1994, Nature, 371, 495

Masuda, S., Kosugi, T., & Hudson, H. S. 2001, Sol. Phys., 204, 55

Matthews, S. A., van Driel-Gesztelyi, L., Hudson, H. S., & Nitta, N. V. 2003, Astron. & Astrophys., 409, 1107

McClements, K. G. 1990a, Astron. & Astrophys., 234, 487

—. 1990b, Astron. & Astrophys., 230, 213

McClements, K. G., & Alexander, D. 2005, Astrophys. J., 619, 1153

Melnikov, V. F., Shibasaki, K., & Reznikova, V. E. 2002, Astrophys. J., 580, L185

Melrose, D. B., & Brown, J. C. 1976, Mon. Not. R. Astron. Soc., 176, 15

Metcalf, T. R., Alexander, D., Hudson, H. S., & Longcope, D. W. 2003, Astrophys. J., 595, 483

Miller, J. A., Larosa, T. N., & Moore, R. L. 1996, Astrophys. J., 461, 445

Moore, R. L., Sterling, A. C., Hudson, H. S., & Lemen, J. R. 2001, Astrophys. J., 552, 833

Nakajima, H., Kosugi, T., Kai, K., & Enome, S. 1983, Nature, 305, 292

Nakajima, H., Nishino, M., Enome, S., Shibasaki, K., Takano, T., Hanaoka, Y., Torii, C., Sekiguchi, H., Bushimata, T., Kawashima, S., Shinohara, N., Irimajiri, Y., Koshiishi, H., Kosugi, T., Shiomi, Y., Sawa, M., & Kai, K. 1994, Proc. IEEE, 82, 705

Nakajima, H., Sekiguchi, H., Sawa, M., Kai, K., & Kawashima, S. 1985, Publ. Astron. Soc. Japan, 37, 163

Nakamura, T. K. 2000, J. Geophys. Res., 105, 10729

Neupert, W. M. 1968, Astrophys. J., 153, L59

Nishio, M., Yaji, K., Kosugi, T., Nakajima, H., & Sakurai, T. 1997, Astrophys. J., 489, 976

Ogawara, Y., Takano, T., Kato, T., Kosugi, T., Tsuneta, S., Watanabe, T., Kondo, I., & Uchida, Y. 1991, Sol. Phys., 136, 1

Ohyama, M., & Shibata, K. 1998, Astrophys. J., 499, 934

Petrosian, V. 1981, Astrophys. J., 251, 727

Petschek, H. E. 1964, in The Physics of Solar Flares, ed. W. N. Hess, 425

Priest, E. R. 1987, Solar magneto-hydrodynamics. (Solar magneto-hydrodynamics by E.R. Priest. Dordrecht: D. Reidel, 1987.)

Ramaty, R. 1969, Astrophys. J., 158, 753

Sakao, T. 1994, PhD thesis, The Univ. of Tokyo

Sakao, T. 1999, in Proceedings of the Nobeyama Symposium, held in Kiyosato, Japan, Oct. 27-30, 1998, Eds.: T. S. Bastian, N. Gopalswamy and K. Shibasaki, NRO Report No. 479., p.321-333

Shimada, N., Terasawa, T., & Jokipii, J. R. 1997, J. Geophys. Res., 102, 22301

Shimojo, M. 2007, private communication

Silva, A. V. R., Gary, D. E., White, S. M., Lin, R. P., & de Pater, I. 1997, Sol. Phys., 175, 157

Silva, A. V. R., & Valente, M. M. 2002, Sol. Phys., 206, 177

Silva, A. V. R., Wang, H., & Gary, D. E. 2000, Astrophys. J., 545, 1116

Smith, D. M., Lin, R. P., Turin, P., Curtis, D. W., Primbsch, J. H., Campbell, R. D., Abiad, R., Schroeder, P., Cork, C. P., Hull, E. L., Landis, D. A., Madden, N. W., Malone, D., Pehl, R. H., Raudorf, T., Sangsingkeow, P., Boyle, R., Banks, I. S., Shirey, K., & Schwartz, R. 2002, Sol. Phys., 210, 33

Somov, B. V., & Kosugi, T. 1997, Astrophys. J., 485, 859

Stepanov, A. V., Yokoyama, T., Shibasaki, K., & Melnikov, V. F. 2007, Astron. & Astrophys., 465, 613

Sturrock, P. A. 1966, Nature, 211, 695

Takakura, T. 1972, Sol. Phys., 26, 151

Takasaki, H., Kiyohara, J., Asai, A., Nakajima, H., Yokoyama, T., Masuda, S., Sato, J., & Kosugi, T. 2007, Astrophys. J., 661, 1234

Tandberg-Hanssen, E., & Emslie, A. G. 1988, The physics of solar flares (Cambridge and New York, Cambridge University Press, 1988, 286 p.)

Terasawa, T., Shibata, K., & Scholer, M. 2000, Adv. Space Res., 26, 573

Tsuneta, S. 1985, Astrophys. J., 290, 353

—. 1995, Publ. Astron. Soc. Japan, 47, 691

Tsuneta, S., Acton, L., Bruner, M., Lemen, J., Brown, W., Caravalho, R., Catura, R., Freeland, S., Jurcevich, B., & Owens, J. 1991, Sol. Phys., 136, 37

Tsuneta, S., & Naito, T. 1998, Astrophys. J., 495, L67

Tsuneta, S., Suematsu, Y., Ichimoto, K., Shimizu, T., Otsubo, M., Nagata, S., Katsukawa, Y., Title, A., Tarbell, T., Shine, R., Rosenberg, B., Hoffmann, C., Jurcevich, B., Levay, M., Lites, B., Elmore, D., Matsushita, T., Kawaguchi, N., Mikami, I., Shimada, S., Hill, L., & Owens, J. 2007, Sol. Phys., submitted

Tsuneta, S., Takahashi, T., Acton, L. W., Bruner, M. E., Harvey, K. L., & Ogawara, Y. 1992, Publ. Astron. Soc. Japan, 44, L211

White, S. M., Janardhan, P., & Kundu, M. R. 2000, Astrophys. J., 533, L167

Xu, Y., Cao, W., Liu, C., Yang, G., Jing, J., Denker, C., Emslie, A. G., & Wang, H. 2006, Astrophys. J., 641, 1210

Yabe, T., Tanaka, R., Nakamura, T., & Xiao, F. 2001, Mon. Wea. Rev., 129, 332

Yokoyama, T., Akita, K., Morimoto, T., Inoue, K., & Newmark, J. 2001, Astrophys. J., 546, L69

Yokoyama, T., Nakajima, H., Shibasaki, K., Melnikov, V. F., & Stepanov, A. V. 2002, Astrophys. J., 576, L87, (Y2002)